

**INVESTIGATION OF FIBRE REINFORCEMENT TOWARD POLYMER  
PRODUCTION EMPHASIZING FUSED DEPOSITION MODELLING**

**PENYIASATAN PENGUATAN FIBER KE ATAS PRODUK POLYMER  
MENGUNAKAN KAEDAH PEMODELAN PEMENDAPAN BERCAMPUR**



**IDRIS BIN MAT SAHAT  
AHMED NURYE OUMER  
ZULKIFLI BIN AHMAD@MANAP  
MOHD RUZAIMI BIN MAT REJAB**

**RESEARCH VOTE NO.:  
RDU150387**

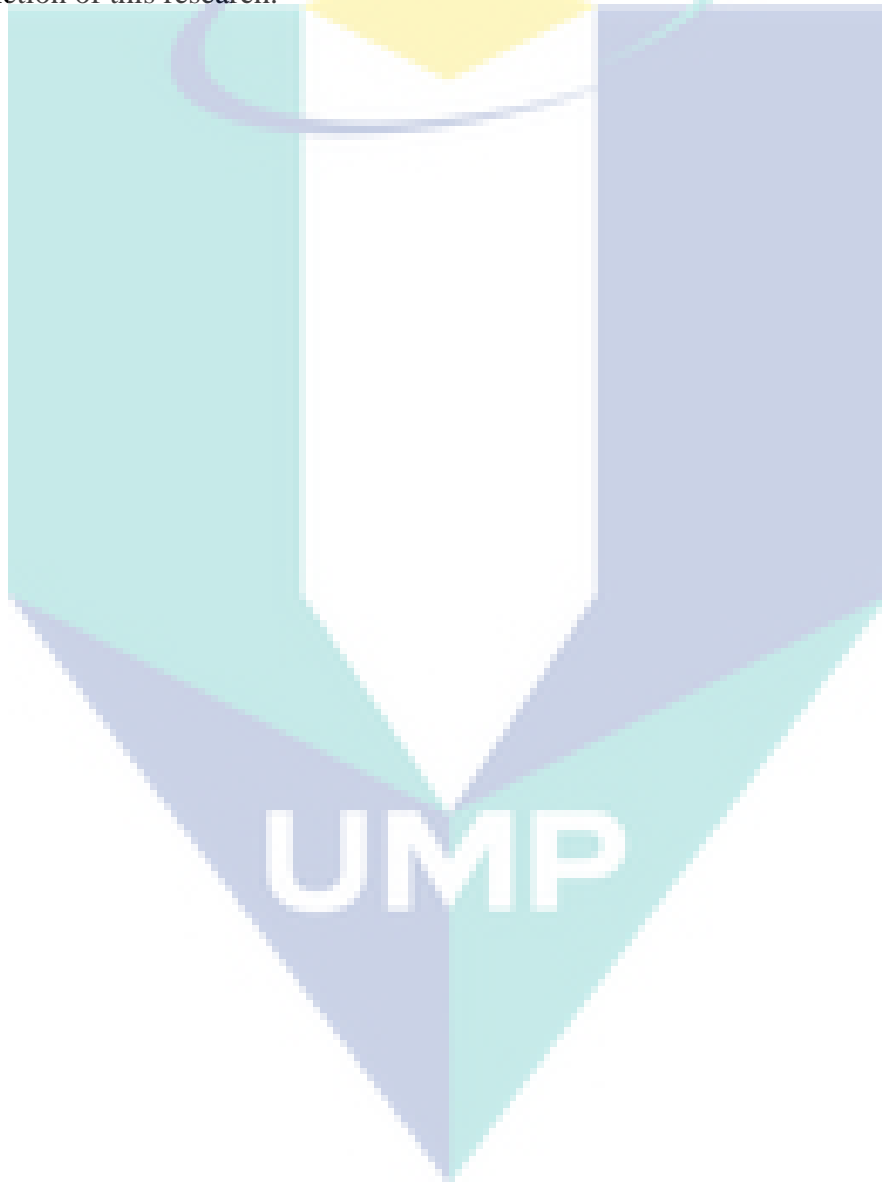
**UMP**

**Fakulti Teknologi Kejuruteraan Mekanikal dan Automotif  
Universiti Malaysia Pahang**

## ACKNOWLEDGEMENTS

I am grateful and would like to express my sincere gratitude Universiti Malaysia Pahang for this opportunity to conduct research

My sincere thanks go to Mr. Ahmad Zukarnain Bin Mohamed, assistant vocational training in Material Laboratory, for his support in handling the machine. Special thanks should be given to fellow researchers and friends. I would like to acknowledge their comments and suggestions, which was crucial for the successful completion of this research.



## ABSTRAK

Percetakan 3D adalah salah satu teknologi prototaip pantas untuk mengarang struktur 3D. Pemodelan Pemodelan Berfungsi (FDM) adalah kaedah percetakan 3D yang popular yang melibatkan lapisan lapisan bahan seperti Polylactic Acid (PLA). Walaupun FDM mempunyai beberapa kelebihan tetapi ada beberapa masalah yang perlu dihadapi. Apabila menetapkan pilihan percetakan, beberapa parameter perlu diambil kira, seperti ketinggian lapisan, suhu percetakan, temperatur buildplate, diameter, kelajuan cetak, kelajuan perjalanan, ketumpatan infill dan corak infill. Memilih parameter ini sering menjadi cabaran besar bagi pengguna, dan secara amnya diselesaikan oleh pengalaman tanpa mengambil kira pengaruh variasi dalam parameter pada sifat mekanik bahagian yang dicetak. Kajian ini menganalisis kesan peratusan infill pada sifat mekanik Polylactic Acid (PLA) dan spesimen tegangan lenturan. Untuk mengenal pasti kesan ini, lakukan ujian tegangan dan ujian lenturan. Spesimen prototaip pesat dicetak pada peratusan infill yang berbeza (30%, 50% dan 70%) dan corak infill yang berbeza (Grid, segitiga dan garis) tetapi selebihnya parameter percetakan disimpan malar. Dua keputusan yang berbeza telah dianalisis untuk ujian ini, sifat tegangan (Kekuatan Tegangan Tepat, Tegangan Tegangan pada pecah, Kemuluran di UTS) dan sifat lentur (Tekanan Flexural, Modulus Flexural). Keputusan menunjukkan bahawa UTS tertinggi adalah pada persamaan inframerah sebanyak 70% 34.66MPa (corak garis), Tekanan tegangan tertinggi pada rehat adalah pada peratusan 70% infill adalah 12.07MPa (Corak Grid), Kemuluran tertinggi pada UTS adalah pada peratus% infill adalah 5.29% (Corak garis), Tekanan Flexural tertinggi adalah pada peratus 70% infill adalah 56.59 MPa (Corak Grid) dan Modulus Flexural tertinggi adalah pada peratus% infill ialah 2278.48 MPa (Corak Grid). Selepas membandingkan tiga graf polynomial untuk sifat tegangan, ia menyimpulkan bahawa corak garis tidak terjejas oleh parameter percetakan yang berterusan kerana nilai sifat tegangan meningkat dengan peningkatan peratusan infill tetapi corak segi tiga dipengaruhi oleh parameter percetakan yang berterusan apabila mencetak pada pola 70% dan grid apabila mencetak pada 50% disebabkan oleh penurunan nilai sifat tegangan. Selepas membandingkan dua graf polynomial untuk sifat lentur, ia menyimpulkan bahawa corak grid tidak terjejas oleh parameter percetakan yang berterusan kerana nilai sifat lentur meningkat dengan peningkatan peratusan infill tetapi corak segi tiga dan corak garis dipengaruhi oleh parameter percetakan yang berterusan apabila mencetak pada 70% disebabkan oleh penurunan sifat lenturan nilai.

## ABSTRACT

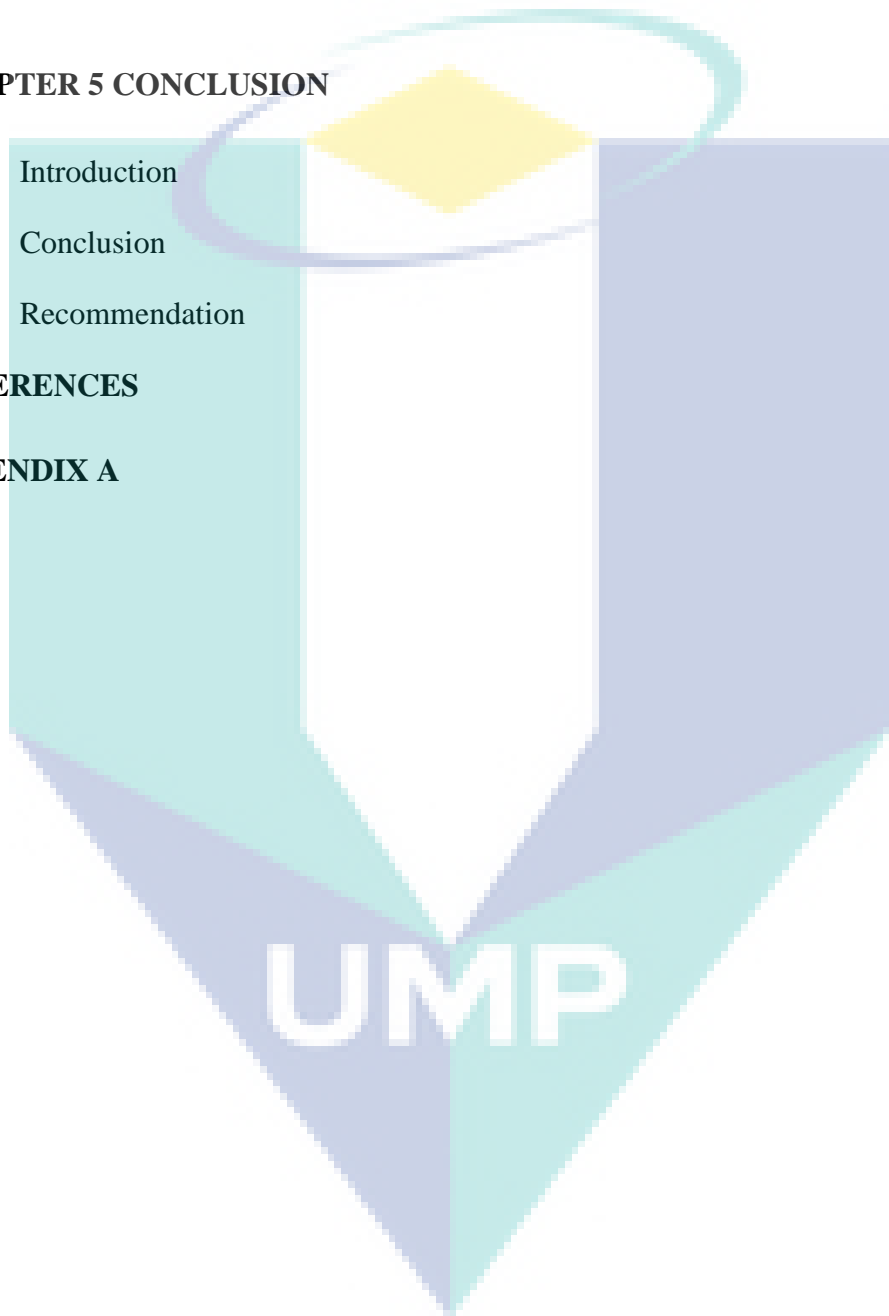
3D printing is one of rapid prototyping technology to fabricate 3D structure. Fused Deposition Modeling (FDM) is a popular 3D printing methods that involve extruding layers of material like Polylactic Acid (PLA). Even though FDM has some advantages but there are several difficulties that have to be faced. When setting the printing options, several parameters have to be taken into account, such as layer height, printing temperature, buildplate temperature, diameter, print speed, travel speed, infill density and infill pattern. Selecting these parameters is often a great challenge for the user, and is generally solved by experience without considering the influence of variations in the parameters on the mechanical properties of the printed parts. This research analyzes the effect of the infill percentage on the mechanical properties of Polylactic Acid (PLA) tensile specimen and flexural specimen. In order to characterize this effect, conduct tensile test and flexural test. The rapid prototyping specimen were printed at different infill percentage (30%, 50% and 70%) and different infill pattern (Grid, triangle and line) but the rest of the printing parameters were kept constant. Two different results were analyzed for these tests, tensile properties (Ultimate Tensile Strength, Tensile Stress at break, Ductility at UTS) and flexural properties (Flexural Stress, Flexural Modulus). Results showed that highest UTS is at 70% infill percentage 34.66MPa (Line pattern), highest Tensile Stress at break is at 70% infill percentage is 12.07MPa (Grid pattern), highest Ductility at UTS is at 70% infill percentage is 5.29% (Line pattern), highest Flexural Stress is at 70% infill percentage is 56.59 MPa (Grid pattern) and highest Flexural Modulus is at 70% infill percentage is 2278.48 MPa (Grid pattern). After comparing three polynomial graph for tensile properties, it conclude that line pattern is not affected by the constant printing parameter because tensile properties value increase by increasing infill percentage but triangle pattern is affected by constant printing parameter when printing at 70% and grid pattern when printing at 50% due to decreasing tensile properties value. After comparing two polynomial graph for flexural properties, it conclude that grid pattern is not affected by the constant printing parameter because flexural properties value increase by increasing infill percentage but triangle pattern and line pattern are affected by constant printing parameter when printing at 70% due to decreasing flexural properties value.

## TABLE OF CONTENT

<b>DECLARATION</b>	
<b>TITLE PAGE</b>	
<b>ACKNOWLEDGEMENTS</b>	<b>ii</b>
<b>ABSTRAK</b>	<b>iii</b>
<b>ABSTRACT</b>	<b>iv</b>
<b>TABLE OF CONTENT</b>	<b>v</b>
<b>LIST OF TABLES</b>	<b>viii</b>
<b>LIST OF FIGURES</b>	<b>ix</b>
<b>LIST OF SYMBOLS</b>	<b>x</b>
<b>LIST OF ABBREVIATIONS</b>	<b>xi</b>
<b>CHAPTER 1 INTRODUCTION</b>	<b>1</b>
1.1 Background of Study	1
1.2 Problem Statement	2
1.3 Objective of Research	2
1.4 Scope of Research	2
1.5 Thesis Overview	3
<b>CHAPTER 2 LITERATURE REVIEW</b>	<b>4</b>
2.1 Introduction	4
2.2 Additive Manufacturing	4
2.2.1 The Benefits of Additive Manufacturing	5
2.3 Rapid Prototyping	6

2.4	3D Printing	6
2.4.1	RepRap	7
2.5	Fused Deposition Modeling	8
2.5.1	Fused Deposition Modeling Materials Properties	9
2.5.2	Advantages and Disadvantages of FDM	10
2.6	Material	10
2.6.1	Polylactic Acid	10
2.7	Computer Aided Design	11
2.8	Testing Method	11
2.8.1	Tensile Test and Flexural Test	11
2.9	Printing parameter	12
2.10	Tensile properties	13
2.11	Flexural properties	15
<b>CHAPTER 3 METHODOLOGY</b>		<b>16</b>
3.1	Introduction	16
3.2	Flow chart	17
3.3	Draw speciment using SolidWorks	18
3.4	Print speciment using 3D printer	19
3.5	Tensile Test and Flexural Test	20
3.6	Analyse data and plot graph using Microsoft Excel	23
<b>CHAPTER 4 RESULTS AND DISCUSSION</b>		<b>25</b>
4.1	Introduction	25
4.2	Effect on time taken to print, length of filament used and weight of speciment	25
4.3	Table of data for tensile properties	33

4.4	Effect on Ultimate Tensile strength, Tensile stress at break and Ductility	36
4.5	Table of data for flexural properties	42
4.6	Effect on Flexural Stress and Flexural Modulus	45
4.7	Summary	49
<b>CHAPTER 5 CONCLUSION</b>		<b>51</b>
5.1	Introduction	51
5.2	Conclusion	51
5.3	Recommendation	52
<b>REFERENCES</b>		<b>53</b>
<b>APPENDIX A</b>		<b>57</b>



## LIST OF TABLES

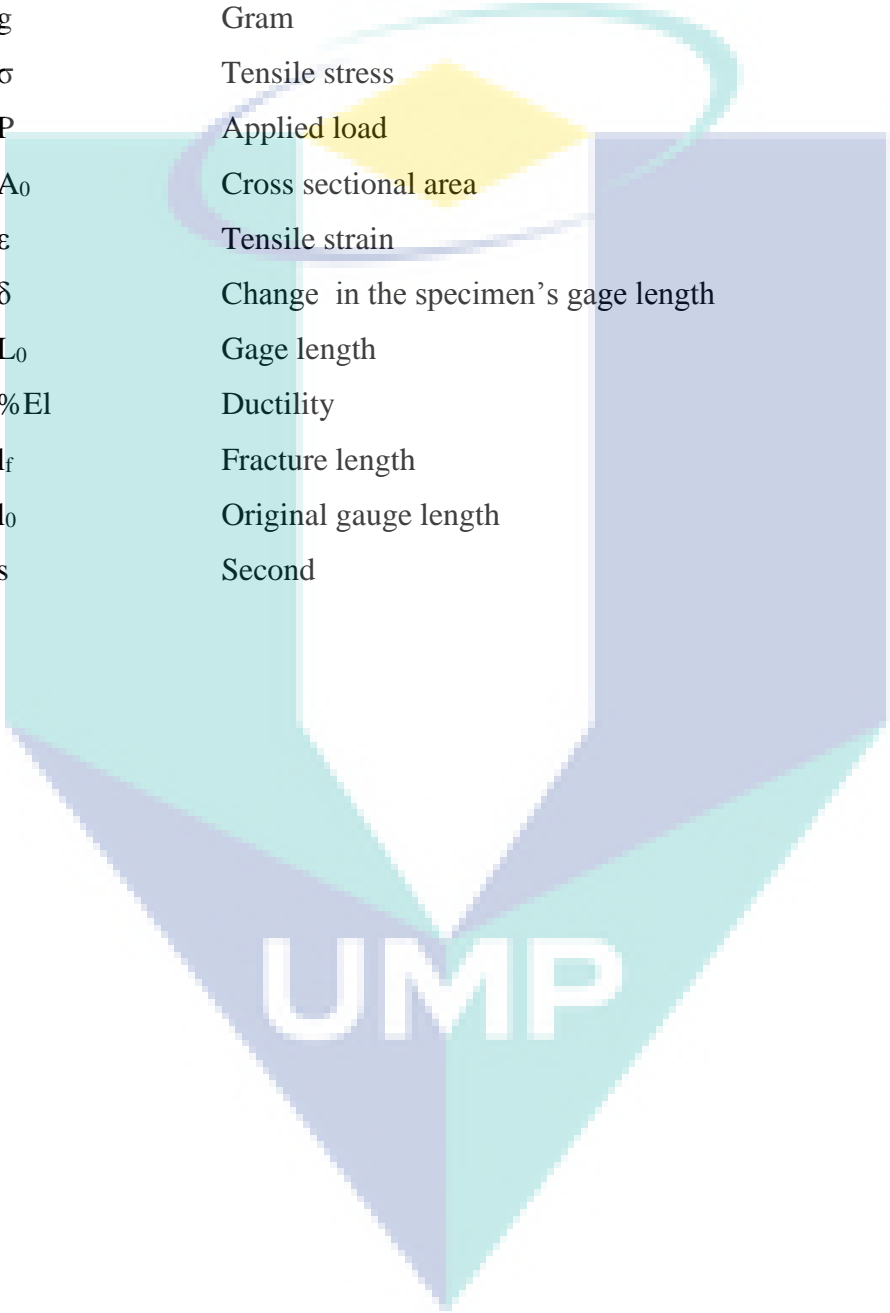
<b>Table</b>	<b>Title</b>	<b>Page</b>
Table 2.1	Benefits of Additive Manufacturing	5
Table 2.2	Comparison of open source printers	7
Table 2.3	Mechanical properties of FDM build materials	10
Table 2.4	Advantages and Disadvantages of FDM	10
Table 2.5	Layer Thickness Examples	13
Table 3.1	Printing parameter	19
Table 3.2	Total rapid prototyping specimen for tensile test and flexural test	20
Table 3.3	Testing parameters	22
Table 4.1	Data from Cura software to print ASTM D638-10 sample	26
Table 4.2	Data from Cura software to print ASTM D790-10	29
Table 4.3	Structure inside rapid prototyping specimen	32
Table 4.4	Tensile properties for triangle pattern at 30% infill percentage	33
Table 4.5	Tensile properties for triangle pattern at 50% infill percentage	33
Table 4.6	Tensile properties for triangle pattern at 70% infill percentage	33
Table 4.7	Tensile properties for line pattern at 30% infill percentage	34
Table 4.8	Tensile properties for line pattern at 50% infill percentage	34
Table 4.9	Tensile properties for line pattern at 70% infill percentage	34
Table 4.10	Tensile properties for grid pattern at 30% infill percentage	35
Table 4.11	Tensile properties for grid pattern at 50% infill percentage	35
Table 4.12	Tensile properties for grid pattern at 70% infill percentage	35
Table 4.13	Complete average value of tensile properties	36
Table 4.14	Flexural properties for triangle pattern at 30% infill percentage	42
Table 4.15	Flexural properties for triangle pattern at 50% infill percentage	42
Table 4.16	Flexural properties for triangle pattern at 70% infill percentage	42
Table 4.17	Flexural properties for line pattern at 30% infill percentage	43
Table 4.18	Flexural properties for line pattern at 50% infill percentage	43
Table 4.19	Flexural properties for line pattern at 70% infill percentage	43
Table 4.20	Flexural properties for grid pattern at 30% infill percentage	44
Table 4.21	Flexural properties for grid pattern at 50% infill percentage	44
Table 4.22	Flexural properties for grid pattern at 70% infill percentage	44
Table 4.23	Complete average value of flexural properties	45



## LIST OF FIGURES

<b>Figure</b>	<b>Title</b>	<b>Page</b>
Figure 2.1	Schematic of FDM process	9
Figure 2.2	Stress-Strain curve	12
Figure 2.3	Ductility graph	14
Figure 2.4	Various type of plastic Stress-Strain diagram	14
Figure 3.1	Flow chart of the research	17
Figure 3.2	Tensile test specimen	18
Figure 3.3	Flexural test specimen	18
Figure 3.4	3D Printer	19
Figure 3.5	Tensile test set-up	21
Figure 3.6	Flexural test set-up	21
Figure 3.7	Interface of the software	21
Figure 4.1	Complete ASTM D638-10 specimen	26
Figure 4.2	The graph of Time taken to print 1 sample versus Infill Percentage for ASTM D638-10 specimen	28
Figure 4.3	ASTM D790-10 specimen for line pattern group at 30%	29
Figure 4.4	The graph of Time taken to print 1 sample versus Infill Percentage for ASTM D790-10 specimen	31
Figure 4.5	The graph of Ultimate Tensile Strength versus Infill Percentage	37
Figure 4.6	The graph of Tensile Stress at Break versus Infill Percentage	39
Figure 4.7	ASTM D638-10 after tensile test	40
Figure 4.8	The graph of Ductility at Ultimate Tensile Strength versus Infill	41
Figure 4.9	The graph of Flexural Stress versus Infill Percentage	46
Figure 4.10	The graph of Flexural Modulus versus Infill Percentage	48
Figure 4.11	ASTM D790-10 after flexural test	49

## LIST OF SYMBOLS



mm	Millimetre
min	Minute
g	Gram
$\sigma$	Tensile stress
P	Applied load
$A_0$	Cross sectional area
$\epsilon$	Tensile strain
$\delta$	Change in the specimen's gage length
$L_0$	Gage length
%El	Ductility
$l_f$	Fracture length
$l_0$	Original gauge length
s	Second

## LIST OF ABBREVIATIONS

ASTM	American Society of Testing Materials International
AM	Additive Manufacturing
CAD	Computer Aided Design
FDM	Fused Deposition Modeling
ISO	International Standards Organization
RP	Rapid Prototyping
RepRap	Replicating Rapid Prototyper
PLA	Polylactic Acid
UTS	Ultimate Tensile Strength



UMP

## CHAPTER 1

### INTRODUCTION

#### 1.1 Background of Study

The purpose of this chapter is to describe about the main point of this research regarding on Additive Manufacturing (AM) technique, Fused Deposition Modeling (FDM) by 3D printing to produce Rapid Prototyping (RP) specimen. Three synonyms commonly used to describe range of process are RP, AM and 3D printing, its main application is to fabricate parts from different type of material starting from Computer Aided Design (CAD) model through additive process and layer upon layer (Lanzotti, Grasso, Staiano, & Martorelli, 2015). AM process can be sub-divided into seven categories, material extrusion, material jetting and powder bed fusion utilize thermal reaction bonding, binder jetting, material jetting, vat photopolymerization and sheet lamination utilize chemical reaction bonding as state of fusion during production (Ivey, Melenka, Carey, & Ayranci, 2017). This thesis paper is based on material extrusion also known as Fused Deposition Modeling (FDM). It is a popular 3D printing method that involves extruding layers of material like Polylactic Acid (Alvarez C., Lagos C., & Aizpun, 2016).

FDM is widely used for fabricating thermoplastic parts that are used as RP specimen for functional testing like tensile test and flexural test with benefit of cheap cost, least waste and it can transform material easily (Ning, Cong, Qiu, Wei, & Wang, 2015). This paper presents an engineering approach for the thermoplastic polymer characterization made by FDM, 3D Printer. Tensile test and flexural test are performed for specimen with different infill percentage (30%, 50% and 70%) and different infill pattern (Grid, triangle and line). Tensile properties (Ultimate Tensile Strength, Tensile Stress at

break, Ductility at UTS) and flexural properties (Flexural Stress, Flexural Modulus) are gain from the test.

## 1.2 Problem Statement

There is only a few research on 3D printing at different infill percentage so the effect toward mechanical properties and printing parameter need to be study.

## 1.3 Objective of Research

The objectives of this research are:

- i. To study the effect of different infill percentage toward mechanical properties and printing parameter.
- ii. To study the effect of different infill pattern toward mechanical properties and printing parameter.

## 1.4 Scope of Research

The scope for this research can be summarized as follow:

- i. Use PLA filament with 1.75 mm thickness.
- ii. Follow ASTM D638-10 standard for tensile test.
- iii. Follow ASTM D790-10 standard for flexural test.
- iv. Printing parameter that change are only infill density and infill pattern, the others remain constant.

## 1.5 Thesis Overview

This thesis is mainly consisting of five main chapters; Introduction (Chapter 1), Literature Review (Chapter 2), Methodology (Chapter 3), Results and Discussion (Chapter 4), and Conclusions (Chapter 5). The first chapter; Introduction provides information of the research background and the problem statement concerning the research. The previous research were studied behalf on from many researchers are covered in Literature Review. Next, for the third chapter describes on the processes of this experimental work, which is includes the printing the specimen, tensile test, and flexural test which are covered in Methodology. The result and findings from the experimental works are presented in Result and Discussion in which this chapter emphasize on execution of the planning on Chapter 3. Finally, the conclusion from the related discussion and recommendation for new possibility of new findings for future works are covered in last chapter, Conclusion.

The logo of UIMP (Universitas Islam Malang) is a large, downward-pointing arrow shape. It is composed of four triangular sections meeting at a central point. The top-left and bottom-right sections are light blue, while the top-right and bottom-left sections are a slightly darker shade of blue. The letters 'UIMP' are printed in white, bold, sans-serif font across the center of the arrow.

UIMP

## CHAPTER 2

### LITERATURE REVIEW

#### 2.1 Introduction

The purpose of this chapter is to provide a review of past research efforts related to additive manufacturing, rapid prototyping, 3D printing and fused deposition modeling. A review of other relevant research studies is also provided. The review is organized chronologically to offer insight to how past research efforts have laid the groundwork for subsequent studies, including the present research effort. The review is detailed so that the present research effort can be properly tailored to add to the present body of literature as well as to justify the scope and direction of the present research effort.

#### 2.2 Additive Manufacturing

Additive manufacturing is a process of combining material to create an object from 3D model data(Ning et al., 2015).The world's horizon has captured additive manufacturing since Charles Hull invented the first new manufacturing technique called Stereo Lithography (SLA) in 1984(J. Wang, Xie, Weng, Senthil, & Wu, 2016). In the past, additive manufacturing for rapid prototyping is expensive due to its accurate fabrication of products and usage in production(Tymrak, Kreiger, & Pearce, 2014) but now it is not expensive anymore. The application of additive manufacturing has increased significantly in both volume and scope for the last ten years because of the existence of affordable 3D printing devices(Song et al., 2017). Additive manufacturing has advantages to fabricate complex geometries, rapid design to fabrication cycle times and generate low amount of waste material(Torrado et al., 2015).

## 2.2.1 The Benefits of Additive Manufacturing

Table 2.1 Benefits of Additive Manufacturing

<p>Rapid character of this technology</p>	<p>The speed advantage is not just in terms of the time it takes to build parts. The speeding up of the whole product development process relies much on the fact that we are using computers throughout. Since 3D CAD is being used as the starting point and the transfer to AM is relatively seamless, there is much less concern over data conversion or interpretation of the design intent. Just as 3D CAD is becoming What You See Is What You Get (WYSIWYG), so it is the same with AM and we might just as easily say that What you See Is What You Build (WYSIWYB). The seamlessness can also be seen in terms of the reduction in process steps.</p>
<p>Complexity of parts to be built</p>	<p>Most other manufacturing processes would require multiple and iterative stages to be carried out. As we include more features in a design, the number of these stages may increase dramatically. Even a relatively simple change in the design may result in a significant increase in the time required to build using conventional methods. AM can, therefore, be seen as a way to more effectively predict of time to fabricate models, regardless of what changes may be implemented during this formative stage of the product development. Similarly, the number of processes and resources required can be significantly reduced when using AM.</p>
<p>Technologies are within the repertoire of the craftsman and readily available</p>	<p>AM can be used to remove or at least simplify many of these multi-stage processes. With the addition of some supporting technologies like silicon-rubber molding, drills, polishers, and grinders it can be possible to manufacture a vast range of different parts with different characteristics. Workshops which adopt AM technology can be much cleaner, more streamlined and more versatile than before.</p>



Source:(Gibson, Rosen, & Stucker, 2010)

### **2.3 Rapid Prototyping**

Rapid Prototyping is a machinery use to build a complex part from Computer Aided Design (CAD) drawing by applying layer on it (Tekinalp et al., 2014). This equipment will advance the manufacturing industry by getting along with conventional manufacturing technique(Tekinalp et al., 2014).Rapid Prototyping make it possible to build physical model faster with more complex geometries.

### **2.4 3D Printing**

First patent was registered on March 11, 1986 till now has create many changes, most economists says the implementation and practice of 3D printing today recognized as third industrial revolution, mechanization in the nineteenth century and assembly-line mass production in the twentieth century(Lanzotti et al., 2015). 3D printing is one of rapid prototyping technology to fabricate 3D structure by deposition of a reactive binder liquid onto thin powder layers in mostly mechanical use(Christ, Schnabel, Vorndran, Groll, & Gbureck, 2015). 3D printing is a common technique used to manufacture prototypes(Melenka, Cheung, Schofield, Dawson, & Carey, 2016).3D printing made art, toys, tools, household items and high-value scientific instrument(Tymrak et al., 2014). 3D printing feedstock materials require development to meet the mechanical requirement of load-bearing components(Tekinalp et al., 2014).

One of the most flexible and innovative additive manufacturing technique is 3D printing because it create unique structure various properties(Weng, Wang, Senthil, & Wu, 2016).This technology advantage give mass-scale distribution in digital manufacturing(Tymrak et al., 2014). The advantages using 3D printing are low cost, fast production of samples and almost no waste material (Der Klift et al., 2016).Every machine definitely has it flaws, product printed by 3D printing has weakness points between layers, thermoplastic material tend to shrink during cooling process and create warp on it (Weng et al., 2016). The flaws of thermoplastic material can be overcome by improving it mechanical properties when fiber is reinforced into the material(Weng et al., 2016).

## 2.4.1 RepRap

RepRap founder is Adrian Bowyer, he is supported and influenced by many sponsor that offer complete lesson in assembling 3D printer(Tymrak et al., 2014). In 2005, Dr Adrian Bowyer from University of Bath, United Kingdom developed open-source 3D printer known as the Replicating Rapid Prototyper (RepRap) project(Lanzotti et al., 2015). Latest creation of RepRap is an open-source self-replicating rapid prototype that has made 3D printing with polymer based at cheaper price(Tymrak et al., 2014).

RepRap 3D printers are used in wide range of application such as conventional prototyping and engineering, customizing scientific equipment and technology related product manufacturing for sustainable development(Lanzotti et al., 2015). It fabricate object from acrylonitrile butadiene styrene (ABS) and polylactic acid (PLA), both material have low melting temperature for melt extrusion and also high melting temperature for prints to keep it shape at average temperature(Tymrak et al., 2014).RepRap also could be used for small- scale manufacturing or tool for sustainable development(Tymrak et al., 2014). The table 2.2 shows the characteristic of RepRap.

Table 2.2 Comparison of open source printers

Characteristics	RepRap	Fab@home
Ability to replicate	Yes, ~50%	No
Printable materials	ABS, polycaprolactone, polyactic acid, and HDPE	Most pastes including: silicone rubber caulk, epoxy, cheese, cake frosting, ceramic clay (mixed with ample water), PlayDoh, gypsum plaster, chocolate WindowArt, a product by Klutz, GE black silicone, GE white silicon, Crayola's squeezable paint, specially designed conductive pastes, FabEpoxy and hydrogels
Accuracy	0.5 diameter nozzle 0.1mm positioning accuracy	x-y resolution is about twice the nozzle diameter z resolution is about nozzle diameter. positioning is +/- 25 micrometers off and repeatability is around +/- 100 micrometers.
Ability to print electronics	Not well developed, not solely done by RepRap	Yes
Printable object size	1,110 cm <sup>3</sup> or 67.7 inches <sup>3</sup>	131 cm <sup>3</sup> or 8 inches <sup>3</sup>
Alternate head attachments	Granule extruder, Wax cutter,	Ice printing head, granule head, metal printing head, plastic printing head
Cost of parts	\$520 (RepRap, 2010)	\$2400 (Fab@home, 2010)
Deposition rate	15 cm <sup>3</sup> /hr	Unknown, prints very small objects

Source: (Pearce et al., 2010)

## 2.5 Fused Deposition Modeling

Stratasys Inc invented and developed FDM in the early 1990s is widely used technologies for fabricating plastic parts with the capacity to go against conventional processing technique(J. Wang et al., 2016).FDM patent turning point was marked in 2009 expiration, Crump developed the technique on 9 June 1992 that contribute to widespread open-source movement and created substantial cost decline for these technique(Lanzotti et al., 2015). FDM technique has higher potential for product manufacturing because it is able to compete with conventional polymer processing technique and create a wide range of application in medical, automotive and aeronautics(Carneiro, Silva, & Gomes, 2015). Final product of the FDM parts have limited mechanical properties(Tekinalp et al., 2014).

There are significant void between deposition lines that impairs the mechanical properties of fabricated parts, when the extruded materials cools quickly from melting temperature to chamber temperature it cause development of inner stresses responsible for weak bond between two deposition lines that leads to inter and intra-layer deformation on the form of cracking, delamination or even parts fabrication failure(J. Wang et al., 2016). Disadvantages of FDM happen when parts are formed by additive manufacturing cause delamination that result in premature failure create lower elastic properties than injection moulded parts(Melenka et al., 2016).

FDM achieve the layer by layer build by depositing a material extruded through a nozzle in parallel lines for each individual layer(Tekinalp et al., 2014). In FDM process as show in Figure 2.5, the filament or spool is fed into the liquefier head with the help of feeding pressure produced from a driver gear and a grooved gearing then plastic parts is built layer by layer through depositing the filament materials which is heated to glass transition state and extruded through the extrusion nozzle at constant temperature(Ning et al., 2015).

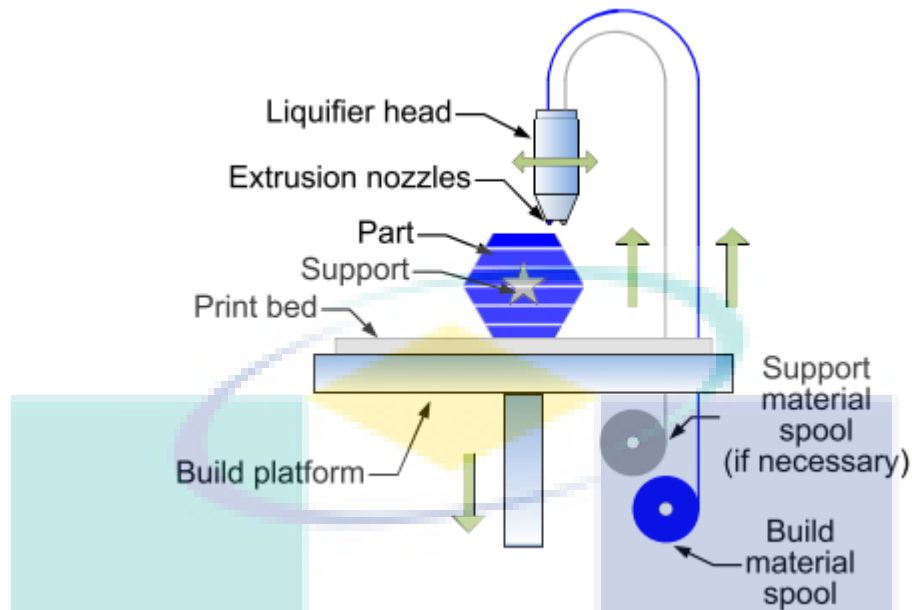


Figure 2.1 Schematic of FDM process

Source: (Ning et al., 2015)

Although a wide range of materials like metals and ceramics exist but thermoplastic are the most suitable filament material for FDM process (Milosevic, Stoof, & Pickering, 2017).

### 2.5.1 Fused Deposition Modeling Materials Properties

In reference (Cooper, 2001), FDM systems now have the capability to build parts with four different materials there are investment-casting wax (ICW06) is an industry-standard foundry wax that is used for many casting applications, ABS (P400) is a rigid plastic material that also comes in six colors: white, red, green, black, yellow, and blue, Medical Grade ABS (P500) has the strength of ABS but also can be sterilized to produce functional medical components and Elastomer (E20) provides a flexible build-material source that can be used for seals, gaskets, shoes, and other applications. The properties of each material is shown in Table 2.3.

Table 2.3 Mechanical properties of FDM build materials

<b>Material</b>	<b>Tensile Strength psi</b>	<b>Tensile Modulus Psi</b>	<b>Flexural Strength psi</b>	<b>Flexural Modulus psi</b>
P400	5000	360000	9500	380000
P500	5400	286000	8500	257000
ICW06	509	40000	619	40000
E20	930	10000	796	20000

Source: (Cooper, 2001)

## 2.5.2 Advantages and Disadvantages of FDM

Table 2.4 Advantages and Disadvantages of FDM

<b>Advantages</b>	<b>Disadvantages</b>
Strength and temperature capability of the build material	Mechanical process itself tends to be slower than laser-based systems, therefore lack of build speed
Safe and laser-free operation	Small features like a thin vertical column prove difficult to build with FDM, due to the fact that each layer must have a physical start-and-stop extrusion point.
Easy post processing with the new water soluble support material	Physical contact with the extrusion tip can sometimes topple, or at least shift, thin vertical columns and walls

Source: (Cooper, 2001)

## 2.6 Material

### 2.6.1 Polylactic Acid

PLA can be process using conventional plastic processing equipment due to its good mechanical properties (L. Wang, Gramlich, & Gardner, 2017). A renewable resource like PLA is biodegradable and able to retain good mechanical properties which promising for composite application for using ecologically friendly material (Li, Li, & Liu, 2016). PLA has been commercialized production line since 2003, from packaging to biomedical fields the usage of PLA is applied (L. Wang et al., 2017). However, PLA is brittle and improvement can be made by using fiber as reinforcement material (Li et al., 2016). Fiber

reinforcement can improve the properties of resins/polymeric materials(Tekinalp et al., 2014).

## **2.7 Computer Aided Design**

CAD is used to create a computerized 3D solid model of the component(Milosevic et al., 2017). CAD model of parts can be manufactured rapidly and directly without geometry limitation and specific tooling with high material utilization(Yang, Tian, Liu, Cao, & Li, 2017). SolidWorks software can be use to create 3D model designs by applying all the specific icon that require to complete a product(Dassault Systèmes SolidWorks Corporation, 2018).

## **2.8 Testing Method**

### **2.8.1 Tensile Test and Flexural Test**

In reference (Forster, 2015), the standards for plastics are ASTM D638 and ISO 527-2 while for composite are ASTM D3039 and ISO 5274-4. (Forster, 2015) said the geometry of utilize dog-bone or end tab specimens is based on the sample or type of composite thickness. Tension measurements provide Young's modulus, Poisson's ratio, Yield Stress, Strength, and Elongation to Break. (Forster, 2015) also said that ASTM D790 and ISO 178 are equivalent standards that utilizes a three point bend method to measure flexural modulus, flexural strength, flexural stress and strain at break within a 5 % strain limit.The graph of stress-strain curve should be like in Figure 2.2

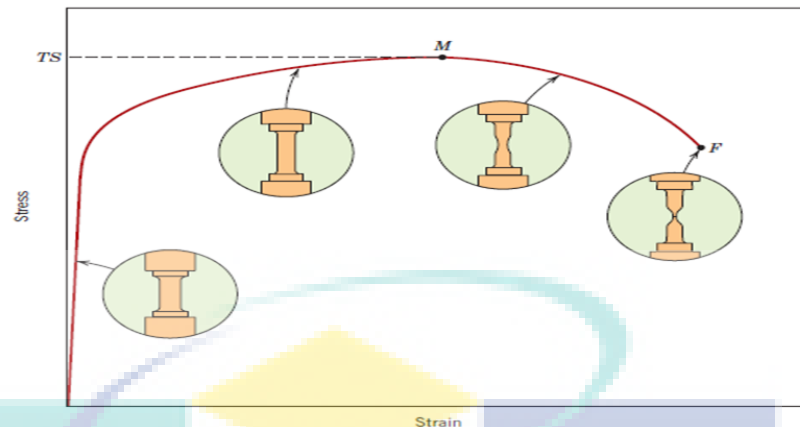


Figure 2.2 Stress-Strain curve  
 Source:(Callister & Rethwisch, 2007)

Typical engineering stress–strain behavior to fracture, point F. The tensile strength, TS is indicated at point M. The circular insets represent the geometry of the deformed specimen at various points along the curve.

## 2.9 Printing parameter

(Sculpteo, 2018)state that layer thickness in 3D printing is a measure of the layer height of each successive addition of material in the 3D printing process in which layers are stacked, the layer height is basically the vertical resolution of the z-axis. In Table 2.5, it show various measurement that is suitable according to type of machine.(Ćwikła, Grabowik, Kalinowski, Paprocka, & Ociepka, 2017), define infill density is percentage of infill of the space inside perimeters that is filled with melted material and infill pattern is filling technique drawn by the nozzle. A part with 50% infill compared to 25% is typically 25% stronger while a shift from 50% to 75% increases part strength by around 10%(Cain, 2018).

Table 2.5 Layer Thickness Examples

<b>Printer / Technology</b>	<b>Layer Thickness</b>
Professional fused deposition modelling for production (Stratasys, etc.)	0.17 mm to 0.33 mm
Office or fablab fused deposition modelling (Makerbot, Ultimaker, etc.)	0.10 mm to 0.33 mm
Selective laser sintering (SLS) - (EOS, 3D System)	0.060mm to 0.150 mm
Resin deposit (Stratasys Polyjet)	0.016mm to 0.028 mm
Material binding (3D Systems ZPrinter)	0.1 mm
Stereolithography, DLP, resin hardening by light or laser	0.05 mm to 0.15 mm
Wax deposition by piezoelectric head (Solidscape)	0.005 mm to 0.10 mm

Source:(Sculpteo, 2018)

In experiment (Ćwikła et al., 2017), the result prove that by increasing the infill value it reduces deformation so the strength improve when increasing the infill density. Honeycomb is the best infill pattern to maximise tensile strength according to (Ćwikła et al., 2017). The past journal usually use honeycomb pattern but not many try to experiment with line, triangle and grid pattern and compare each of it performance. Printing temperature for PLA is usually in between 215°C 235°C(Filaments.ca, 2014) . Print speed defines at which speed (mm/s) the print head moves while printing and travel speed is the speed at which the print head moves when it's not extruding, so when the print head is moving from one point to another(Anon(Ultimaker), 2016).

## 2.10 Tensile properties

The ultimate tensile strength (UTS) is the maximum engineering stress level reached in a tension test and ductility of a material is a measure of the extent to which a material will deform before fracture(Morton & Hearle, 2008). The graph for brittle and ductile material shown in Figure 2.3.



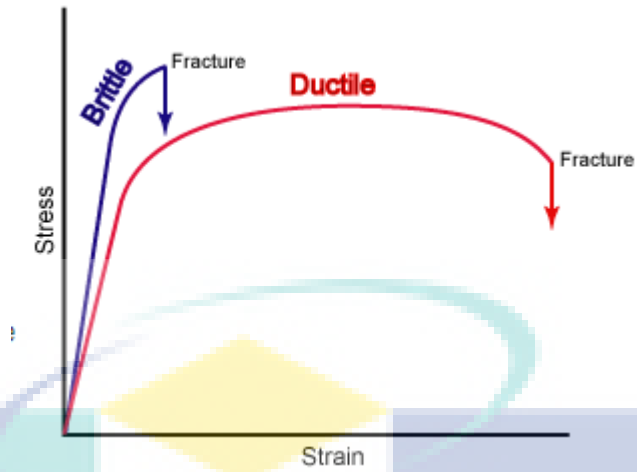


Figure 2.3 Ductility graph  
 Source:(NDT Resource Center, 2018)

The tensile strength at break is the tensile stress at the moment at which a test specimen tears(GmBH, 2018). The graph for tensile strength for various type of plastic in Figure 2.4.

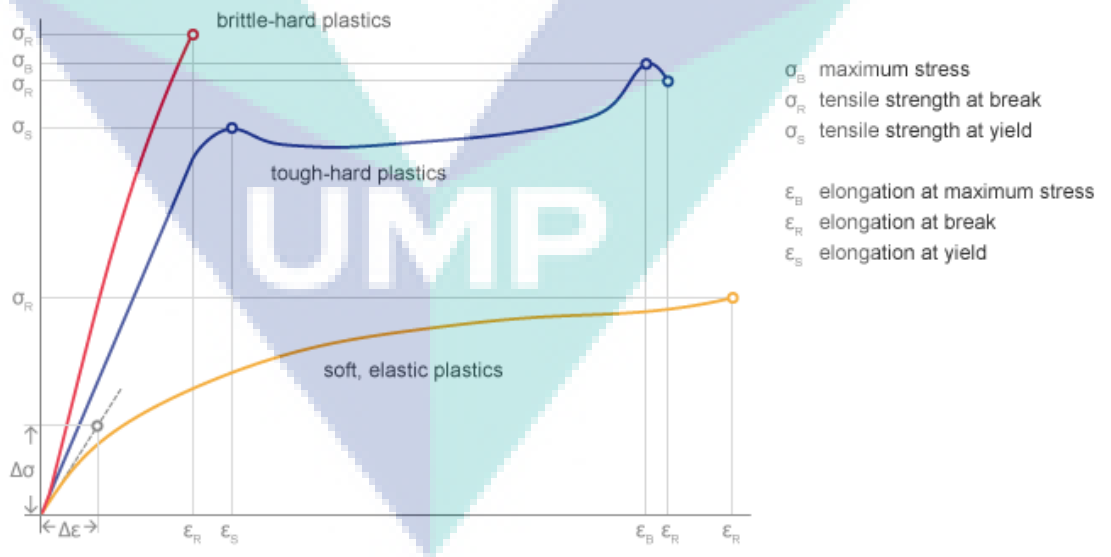
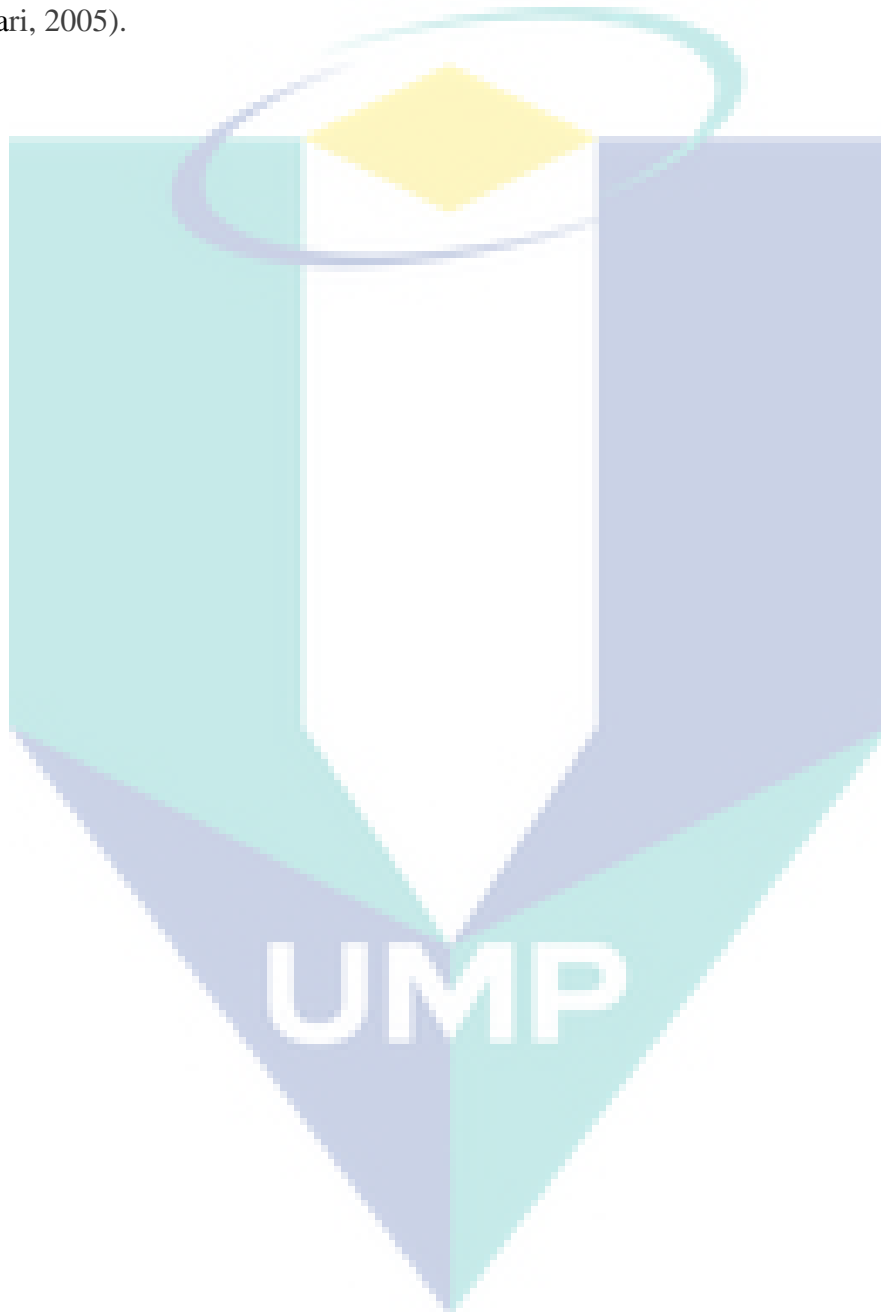


Figure 2.4 Various type of plastic Stress-Strain diagram  
 Source:(GmBH, 2018)

## 2.11 Flexural properties

Flexural strength is the maximum tension that can be loaded on the material without causing its fracture(S.R. Djafari Petroudy, 2017). Flexural modulus is a measure of the strength of adhesives and modulus data are most often used in stress analysis(James J. Licari, 2005).





## CHAPTER 3

### METHODOLOGY

#### 3.1 Introduction

In chapter 3, the method used for the experiment is being described in detail. Besides that, this chapter includes the flow of the study, information on preparation of rapid prototyping specimen, and the flow of experiment done using the suitable apparatus. The experiment is suggested to characterize the mechanical properties of thermoplastic when 3D print the specimen with printing parameter that are not constant, triangle pattern, line pattern and grid pattern (infill pattern) at 30%, 50% and 70% infill percentage (infill density). Through the flow chart, experiment setup is clearly shown the research design. In order to achieve the objectives of this research paper, the suitable apparatus and experimental setup is needed. Thus, the collected data will be analysed further and interpreted in suitable way to validate the result.

### 3.2 Flow chart

Figure 3.1 shows the detail methodology throughout this study starting from research until the analysis based on the main objective line up for the study.

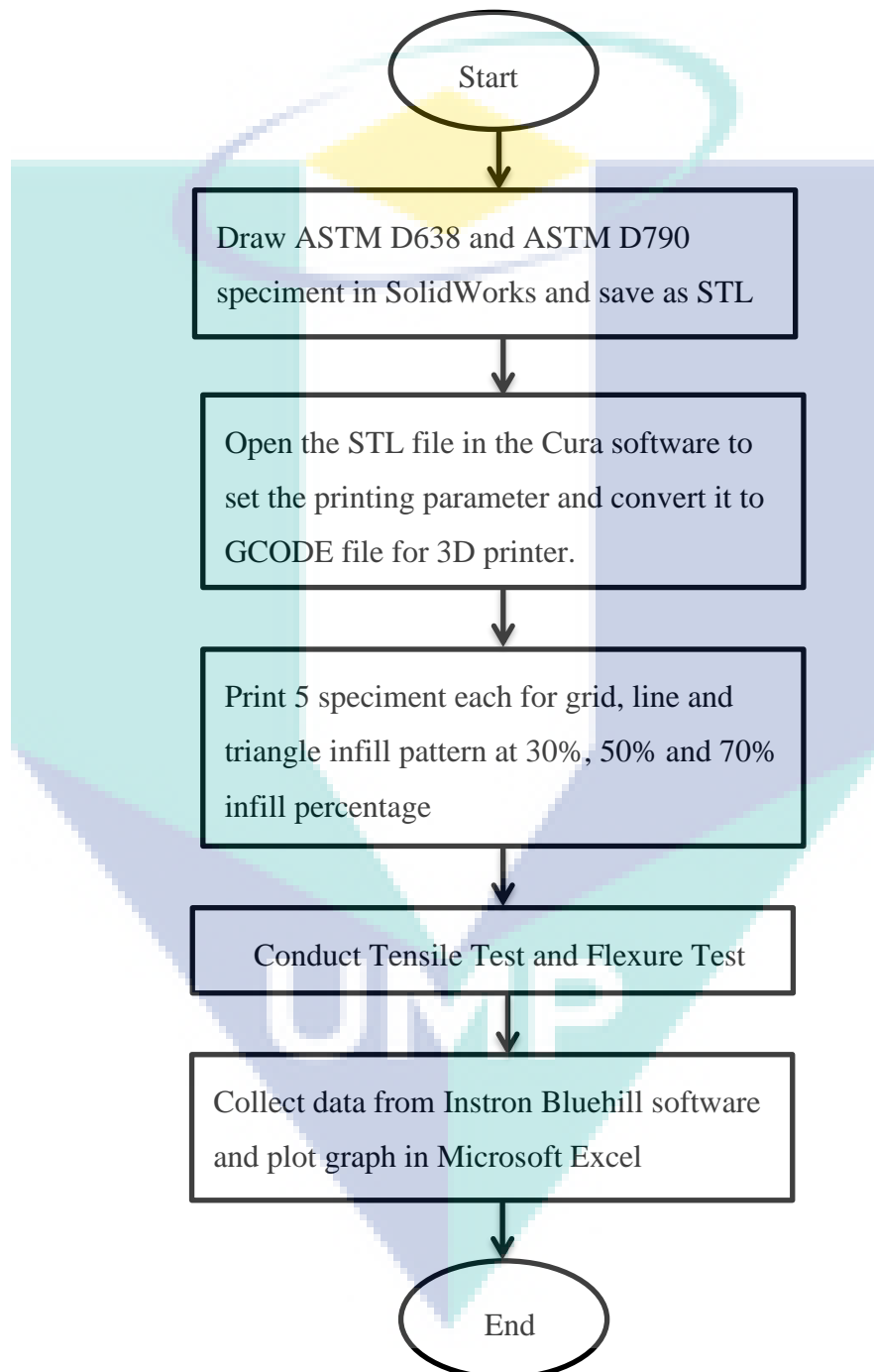


Figure 3.1 Flow chart of the research

### 3.3 Draw specimen using SolidWorks

The tensile test specimen and flexural test specimen were drawn in SolidWorks software according to ASTM D638-10 standard, Figure 3.2 and ASTM D790-10 standard, Figure 3.3. ASTM D638-10 is sketch using line and arc while ASTM D790-10 only use line. Both of the specimen use the same feature, extruded boss to create the thickness. The dimension of each specimen used mm unit is shown in Figure 3.2 and Figure 3.2. The part will be save as STL file because later on it need to be transfer to Cura software and convert the file to GCODE file.

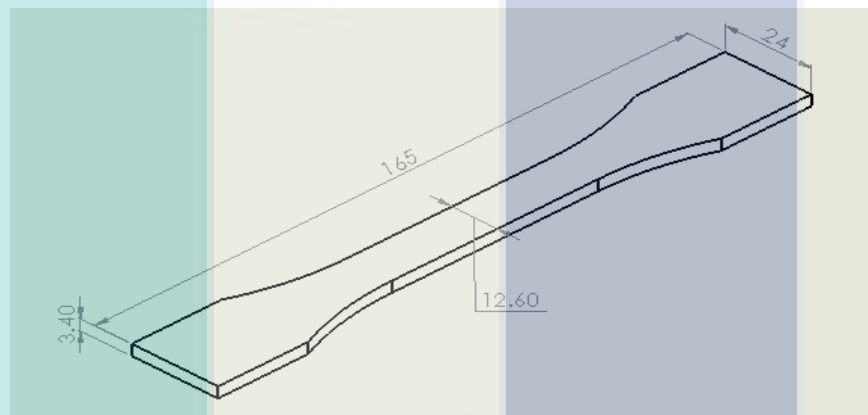


Figure 3.2 Tensile test specimen

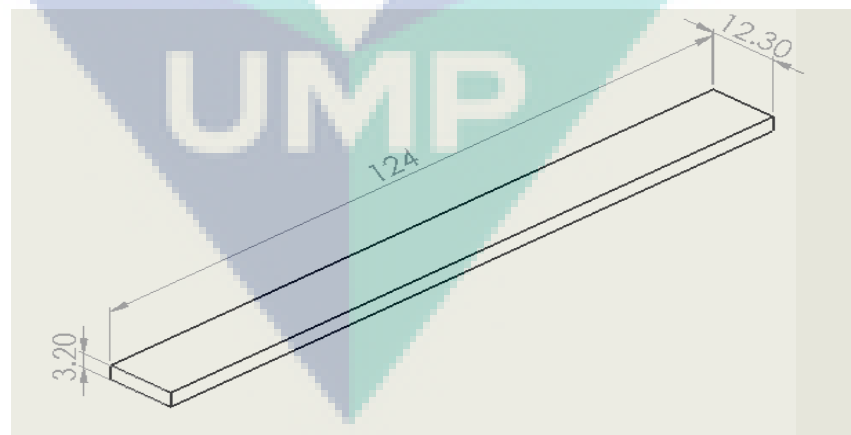


Figure 3.3 Flexural test specimen

### 3.4 Print specimen using 3D printer

The STL file is open in Cura software to set the printing parameter shown in Table 3.1 for the 3D printer in Figure 3.4. Layer height, printing temperature, buildplate temperature, diameter, print speed and travel speed are remain constant except for infill density and infill pattern. The nozzle diameter for 3D printer used is 0.4 mm. The material use to print the filament is white PLA filament with 0.2 mm diameter.

Table 3.1 Printing parameter

Layer Height	0.2 mm
Infill Density	30%, 50%, 70%
Infill Pattern	Grid, Line, Triangle
Printing Temperature	200 °C
Build Plate Temperature	60 °C
Diameter	1.75 mm
Print Speed	60 mm/s
Travel Speed	120 mm/s

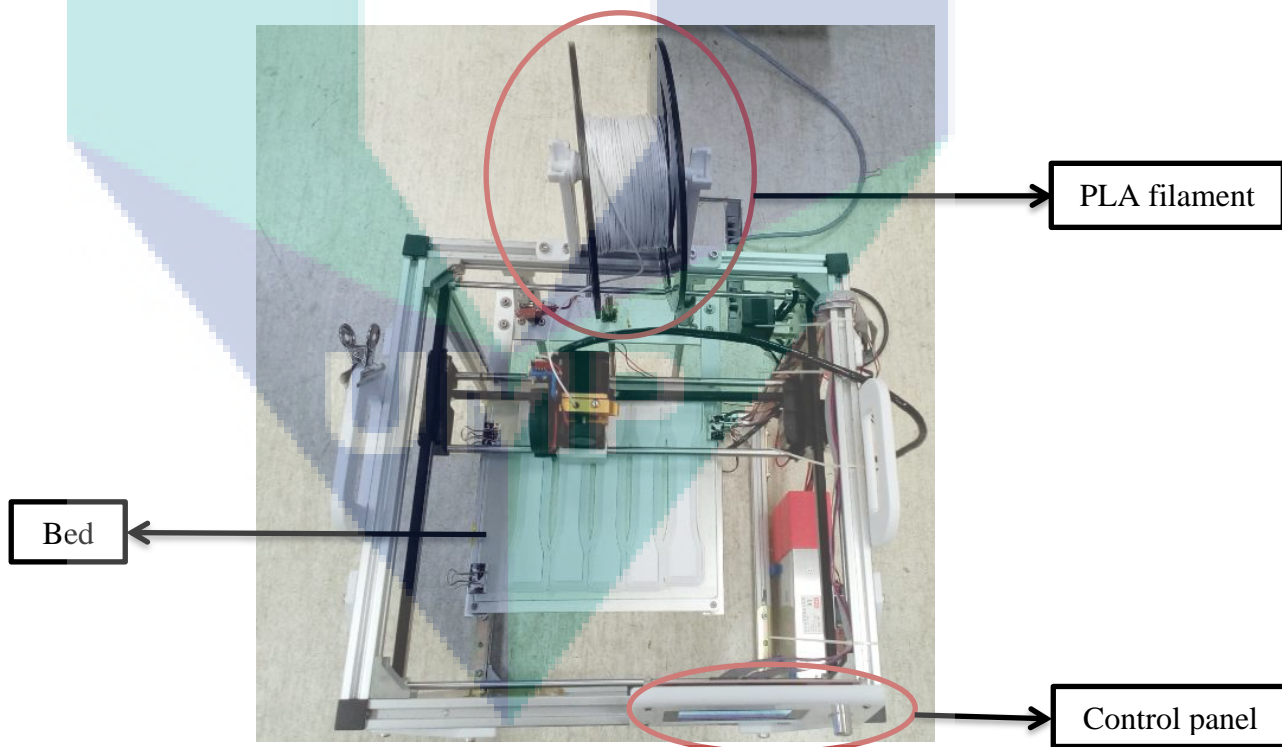


Figure 3.4 3D Printer

After printing parameter is key in, click the button to start slicing. The slicing will record the time taken to print, length of filament used and weight of the specimen. Then, save the file as GCODE file in SD card memory. Lastly, insert the SD card into the control panel and use the knob to search for the file. 3D printer can start to deposit the filament on the bed and produce rapid prototyping specimen for tensile test and flexure test after the file has been selected to print. Each pattern must be printed 5 specimen for different infill percentage. Table 3.2 below show the total amount of rapid prototyping specimen that need to be printed to conduct tensile test and flexural test.

Table 3.2 Total rapid prototyping specimen for tensile test and flexural test

<b>Infill Pattern</b>	<b>Infill Percentage</b>	<b>Amount of sample for tensile test</b>	<b>Amount of sample for flexural test</b>
Grid	30%	5	5
	50%	5	5
	70%	5	5
Line	30%	5	5
	50%	5	5
	70%	5	5
Triangle	30%	5	5
	50%	5	5
	70%	5	5
<b>Total</b>		45	45

### 3.5 Tensile Test and Flexural Test

The tensile test and flexural test is conducted using INSTRON 50kN shown in Figure 3.5, use fix grip and moveable grip to hold the specimen until it break and in Figure 3.6, three-point bending set-up contain one midway loading nose and two supports. The data of relationships between force (N) and displacement (mm) is collected by computer with the help data acquisition software shown in Figure 3.7. The software will collect the raw data in Excel format and display stress versus strain graph.

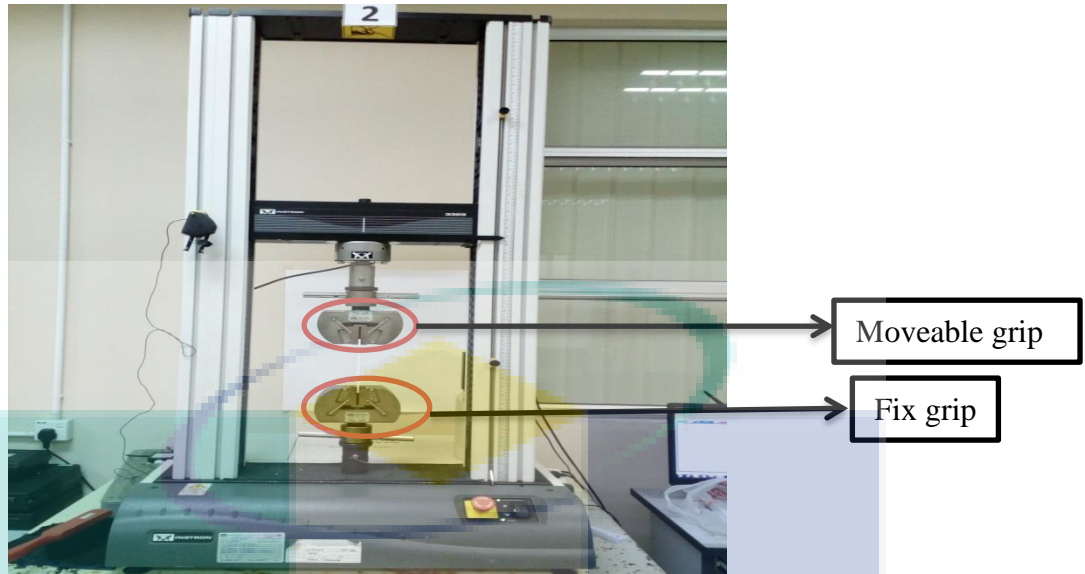


Figure 3.5 Tensile test set-up

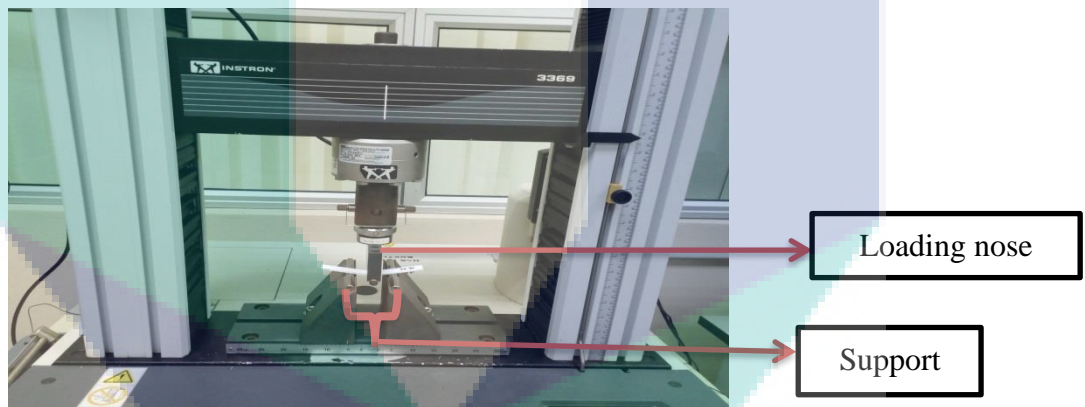


Figure 3.6 Flexural test set-up

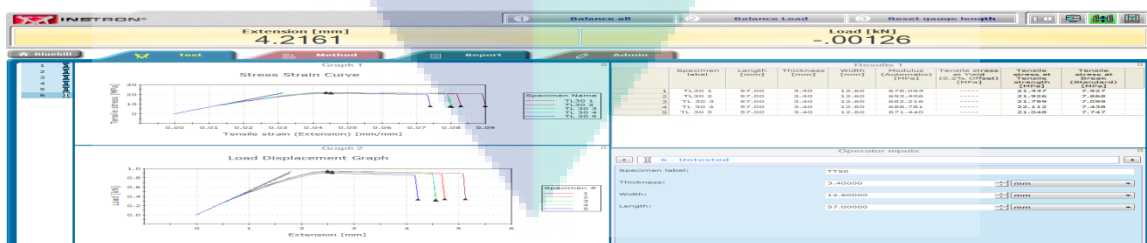


Figure 3.7 Interface of the software



Before start testing, a template is created for tensile test and flexural test in data acquisition software. Open the Instron Bluehill software, click “Method” icon, then “Open Method” to “Create Method”. Choose Test Type, Tension method for tensile test and Flexure method for flexural test. Next, click Specimen > Properties to specify the specimen default properties for each specimen. Key in the width: 12.6 mm, thickness: 3.4 mm and length: 57 mm (tensile test) and for flexural test, width: 3.2 mm, thickness: 12.3 mm and span: 52 mm. Span is length between two support that can be adjusted by the jig. Flexural test also set to stop when it reaches 5% strain limit.

Click Calculations > Setup to identify desired calculations that will be performed during or after the test is run. Maximum Flexure stress (MPa), Flexure strain (Extension) at Maximum Flexure stress (mm/mm) and Modulus (MPa) is chosen for flexural test result while for tensile the result choose to be shown in table are Tensile stress at Tensile strength (MPa) and Tensile Stress at Break (MPa). The testing parameter for tensile test and flexural test is shown in Table 3.3. Mark the distance between two grips so the jaw can be tightened according to the distance mark and same goes to distance between two support to avoid unbalance bending when loading nose is pushing down the specimen.

Table 3.3 Testing parameters

Categories	Tensile test	Flexural Test
Testing speed	5 mm/min	1.4 mm/min
Distance between two grips	130 mm	-
Distance between two supports	-	51.2mm

Lastly before click start, always balance load and reset gauge length first so the data taken will be from initial start and does not continue from previous test. The test will be conducted five time to get the average value. Tensile test specimen will be loaded until it break and flexural test only will be loaded within 5% strain limit.

### 3.6 Analyse data and plot graph using Microsoft Excel

The raw data is taken from the Instron Bluehill software to plot the stress versus strain graph for triangle pattern, line pattern and grid pattern at 30%, 50% and 70% infill percentage using scatter with smooth lines, chart type. The data for flexure strain and flexure stress are auto generated but not for tensile stress and tensile strain data. The tensile stress and tensile strain can be obtain using Eq.3.1 and Eq. 3.2.

$$\sigma = \frac{P}{A_0} \quad \text{Eq.3.1}$$

P, applied load taken from Load (N) data and  $A_0$ , cross sectional area is obtained by multiplying gauge length: 12.6 mm and thickness: 3.4 mm.

$$\varepsilon = \frac{\delta}{L_0} \quad \text{Eq.3.2}$$

$\delta$ , change in the specimen's gage length obtain by subtracting  $L$ , Extension (mm) and  $L_0$ , gage length: 57 mm.

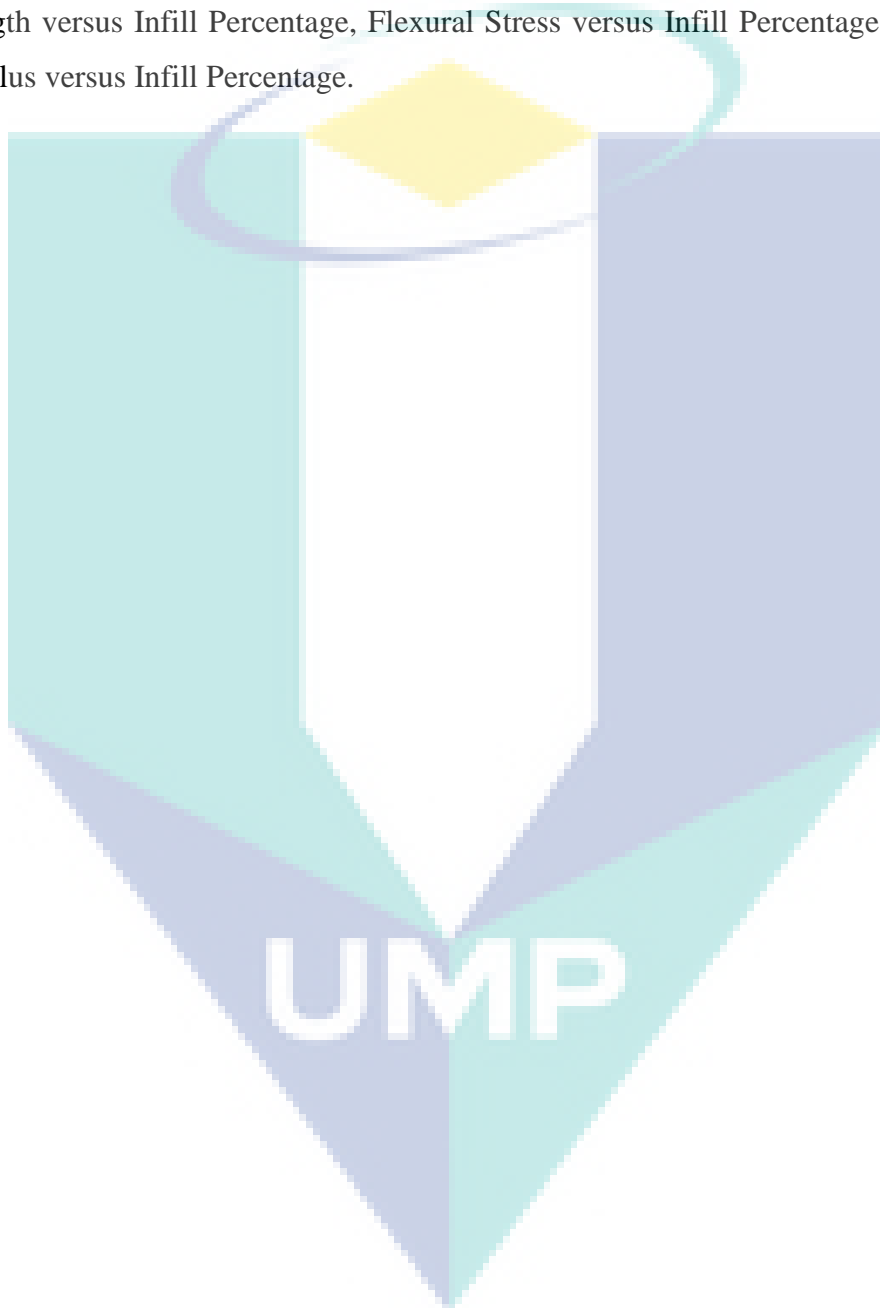
Next, calculate the average data of five specimen using formulae in Eq. 3.3.

$$\text{Average of 5 specimen} = \frac{\text{Total value of five specimen}}{5} \quad \text{Eq.3.3}$$

The average value taken are Ultimate Tensile strength (MPa), Tensile stress at break (MPa) and Ductility (%) from tensile test data and for flexural test the average of Flexural Stress(MPa) and Flexural Modulus(MPa) . Ultimate Tensile strength data is taken from Tensile stress at Tensile strength result from the auto generated table by Instron Bluehill software. Flexural Stress(MPa) and Flexural Modulus(MPa) data also taken from Maximum Flexure stress and Modulus auto generated result. The ductility is calculated using Eq. 3.4.

$$\%El = \left( \frac{l_f - l_0}{l_0} \right) \times 100 \quad \text{Eq.3.4}$$

$l_f$ , fracture length value is taken from Extension (mm) data and  $l_0$ , original gauge length is 57 mm same as length key in while conducting tensile test. After all the average value has been calculate, the graph that need to be plot using scatter with only markers and add polynomial trendline, chart type are Ultimate Tensile Strength versus Infill Percentage, Tensile Stress at Break versus Infill Percentage, Ductility at Ultimate Tensile Strength versus Infill Percentage, Flexural Stress versus Infill Percentage and Flexural Modulus versus Infill Percentage.



## CHAPTER 4

### RESULTS AND DISCUSSION

#### 4.1 Introduction

This chapter presents results of the tensile test and flexural test obtained by using INSTRON 50kN machine that generate data in Instron Bluehill software. The data were analyzed and tabulated. Then, graph are plotted for Ultimate Tensile strength (MPa), Tensile stress at break (MPa), Ductility (%), Flexural Stress (MPa) and Flexural Modulus (MPa). This chapter will explain the effect of triangle pattern, line pattern and grid pattern at 30%, 50% and 70% infill percentage toward mechanical properties.

#### 4.2 Effect on time taken to print, length of filament used and weight of specimen

Time taken to print, length of filament used and weight of specimen data are obtained from Cura software after start slicing. The higher the infill percentage, the longer the time taken to print rapid prototyping specimen (Percentage, 2017). This hypothesis proven in Table 4.1 below with the support of graph in Figure 4.2. A complete set of dog bone specimen (ASTM D638-10) can be seen in Figure 4.1. The weight and length of filament used also increases when calculate percentage different using Eq.4.1, Eq.4.2, Eq.4.3, Eq.4.4, Eq.4.7, Eq.4.8, Eq.4.9 and Eq.4.10. The structure in the specimen can be seen in Table 4.2, taken from Cura software .

Table 4.1 Data from Cura software to print ASTM D638-10 sample

Infill Pattern	Infill Percentage	Time Taken to Print 1 sample	Length of filament used for 1 sample	Weight for 1 sample
Grid	30%	45 minute	3.24 m	9 g
	50%	49 minute	3.63 m	10 g
	70%	52 minute	4.02 m	11 g
Line	30%	45 minute	3.24 m	9 g
	50%	49 minute	3.63 m	10 g
	70%	52 minute	4.02 m	11 g
Triangle	30%	45 minute	3.24 m	9 g
	50%	49 minute	3.63 m	10 g
	70%	52 minute	4.02 m	11 g

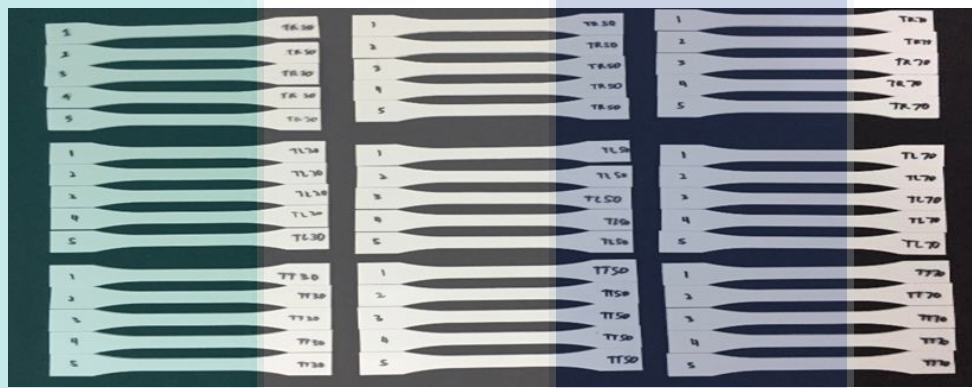


Figure 4.1 Complete ASTM D638-10 specimen

Percentage different of length of filament used for 1 sample (30% to 50%)

$$= \frac{3.63 m_{50\%} - 3.24 m_{30\%}}{3.24 m_{30\%}} \times 100\% = 12.04\% \text{ (increase)} \quad \text{Eq. 4.1}$$

Percentage different of length of filament used for 1 sample (50% – 70%)

$$= \frac{4.02 m_{70\%} - 3.63 m_{50\%}}{3.63 m_{50\%}} \times 100\% = 10.74\% \text{ (increase)} \quad \text{Eq.4. 2}$$

Percentage different of Weight for 1 sample (30% – 50%)

$$= \frac{10g_{50\%} - 9g_{30\%}}{9g_{30\%}} \times 100\% = 11.11\% \text{ (increase)} \quad \text{Eq.4.3}$$

Percentage different of Weight for 1 sample (50% – 70%)

$$= \frac{11g_{70\%} - 10g_{50\%}}{10g_{50\%}} \times 100\% = 10\% \text{ (increase)} \quad \text{Eq.4.4}$$

The length of filament used for 1 sample increase 12.04% when increasing infill percentage from 30% to 50% and increase 10.74% when increasing infill percentage from 50% to 70%. Then, weight for 1 sample also increase 11.11% when increasing infill percentage from 30% to 50% and increase 10% when increasing infill percentage from 50% to 70%. Time taken to print 1 sample are calculated in Eq.4.5 and Eq.4.6.

$$\begin{aligned} & \text{Percentage different of time taken to print 1 sample (30\% - 50\%)} \\ & = \frac{49 \text{ minute}_{50\%} - 45 \text{ minute}_{30\%}}{45 \text{ minute}_{30\%}} \times 100\% = 8.89\% \text{ (increase)} \end{aligned} \quad \text{Eq.4.5}$$

$$\begin{aligned} & \text{Percentage different of time taken to print 1 sample (50\% - 70\%)} \\ & = \frac{52 \text{ minute}_{70\%} - 49 \text{ minute}_{50\%}}{49 \text{ minute}_{50\%}} \times 100\% = 6.12\% \text{ (increase)} \end{aligned} \quad \text{Eq.4.6}$$

The time taken to print 1 sample sample increase 8.89% when increasing infill percentage from 30% to 50% and increase 6.12% when increasing infill percentage from 50% to 70%. The polynomial trend of the relationship between time taken to to print 1 sample sample and infill percentage is shown in Figure 4.2.

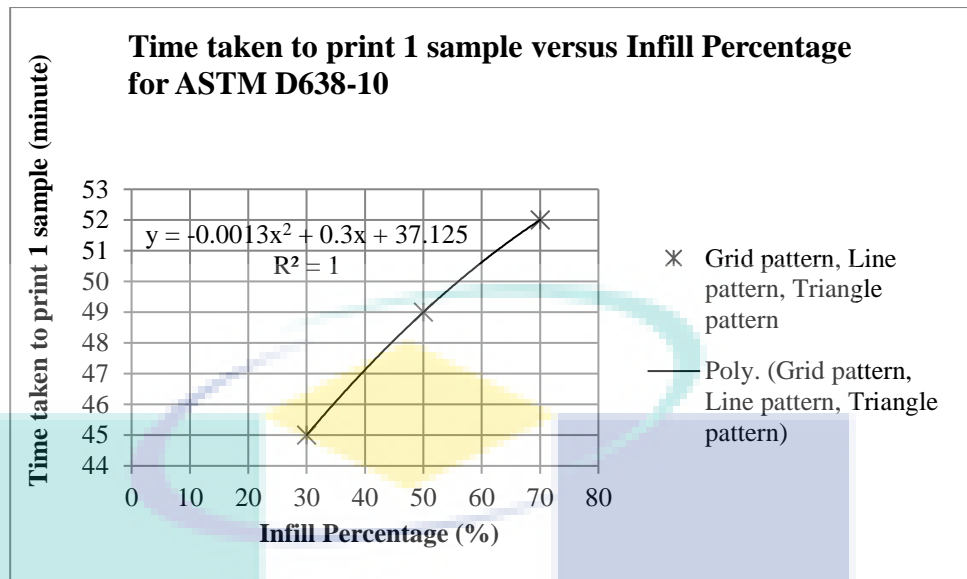


Figure 4.2 The graph of Time taken to print 1 sample versus Infill Percentage for ASTM D638-10 speciment

The graph in Figure 4.2 show time taken to print 1 sample with respect to the infill percentage at 30%,50% and 70%. Grid pattern, line pattern and triangle pattern have similar printing time so only one group of data is plot in the graph. The results show that time taken to print 1 sample is continuously increase to the infill percentage based on the polynomial trend.  $R^2$  value is 1, according to (To, 2015) the linear trendline is reliable because the  $R^2$  value near to 1. (Alvarez C. et al., 2016) result also state that the time the nozzle take to extrude the material on bed layer by layer increases when the infill percentage keep on increasing.

Table 4.2 Data from Cura software to print ASTM D790-10

Infill Pattern	Infill Percentage	Time Taken to Print 1 sample	Length of filament used for 1 sample	Weight for 1 sample
Grid	30%	25 minute	1.79 m	5 g
	50%	27 minute	1.96 m	5 g
	70%	28 minute	2.14 m	6 g
Line	30%	25 minute	1.79 m	5 g
	50%	27 minute	1.96 m	5 g
	70%	28 minute	2.14 m	6 g
Triangle	30%	25 minute	1.79 m	5 g
	50%	27 minute	1.96 m	5 g
	70%	28 minute	2.14 m	5 g



Figure 4.3 ASTM D790-10 specimen for line pattern group at 30% infill percentage

Percentage different of length of filament used for 1 sample (30% to 50%)

$$= \frac{1.96 m_{50\%} - 1.79 m_{30\%}}{1.79 m_{30\%}} \times 100\% = 9.5\% \text{ (increase)} \quad \text{Eq. 4.7}$$

Percentage different of length of filament used for 1 sample (50% – 70%)

$$= \frac{2.14 m_{70\%} - 1.96 m_{50\%}}{2.14 m_{50\%}} \times 100\% = 9.18\% \text{ (increase)} \quad \text{Eq. 4.8}$$

Percentage different of Weight for 1 sample (30% – 50%)

$$= \frac{5g_{50\%} - 5g_{30\%}}{5g_{30\%}} \times 100\% = 0\% \text{ (constant, no increase)} \quad \text{Eq. 4.9}$$

Percentage different of Weight for 1 sample (50% – 70%)

$$= \frac{6g_{70\%} - 5g_{50\%}}{5g_{50\%}} \times 100\% = 20\% \text{ (increase)} \quad \text{Eq. 4.10}$$



The length of filament used for 1 sample increase 9.5% when increasing infill percentage from 30% to 50% and increase 9.18% when increasing infill percentage from 50% to 70%. Then, weight for 1 sample remain constant when increasing infill percentage from 30% to 50% and increase 20% when increasing infill percentage from 50% to 70%. Time taken to print 1 sample are calculated in Eq.4.11 and Eq.4.12.

$$\begin{aligned} & \textit{Percentage different of time taken to print 1 sample (30\% - 50\%)} \\ & = \frac{27 \textit{ minute}_{50\%} - 25 \textit{ minute}_{30\%}}{25 \textit{ minute}_{30\%}} \times 100\% = 8\% \textit{ (increase)} \end{aligned} \quad \textit{Eq.4.11}$$

$$\begin{aligned} & \textit{Percentage different of time taken to print 1 sample (50\% - 70\%)} \\ & = \frac{28 \textit{ minute}_{70\%} - 27 \textit{ minute}_{50\%}}{27 \textit{ minute}_{50\%}} \times 100\% = 3.7\% \textit{ (increase)} \end{aligned} \quad \textit{Eq.4.12}$$

The time taken to print 1 sample sample increase 8% when increasing infill percentage from 30% to 50% and increase 3.7% when increasing infill percentage from 50% to 70%. The polynomial trend of the relationship between time taken to to print 1 sample sample and infill percentage is shown in Figure 4.4

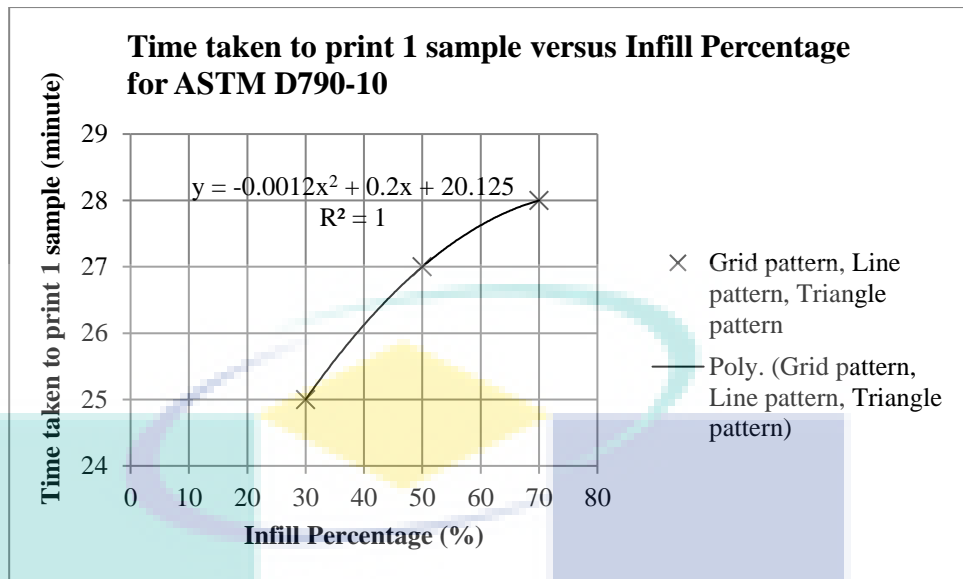
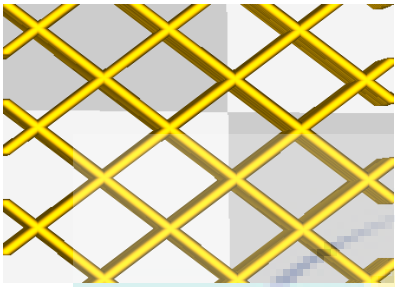
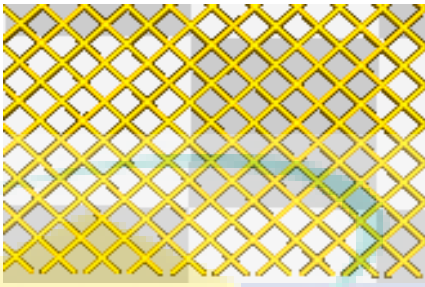
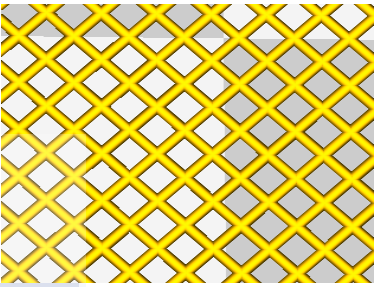
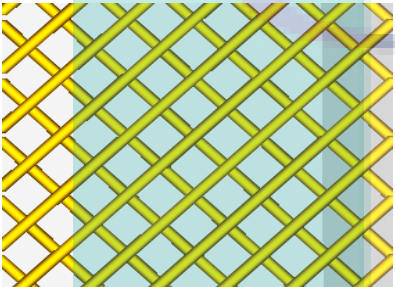
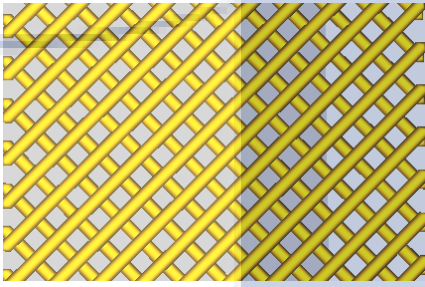
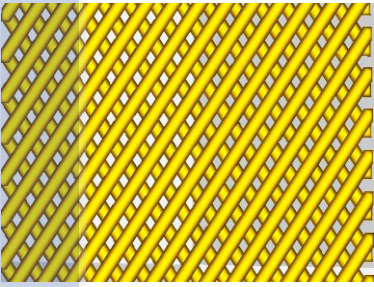
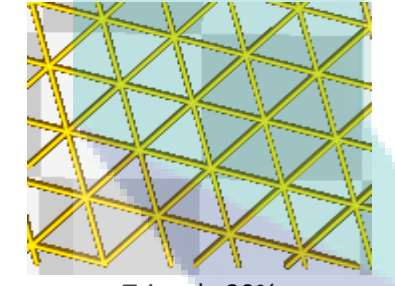
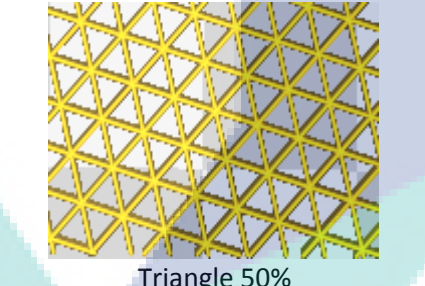
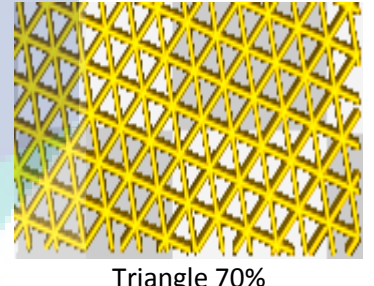


Figure 4.4 The graph of Time taken to print 1 sample versus Infill Percentage for ASTM D790-10 speciment

The graph in Figure 4.4 show time taken to print 1 sample with respect to the infill percentage at 30%,50% and 70%. Grid pattern, line pattern and triangle pattern have same printing time so only one group of data is plot in the graph. The results show that time taken to print 1 sample is gradually increase to the infill percentage based on the polynomial trend.  $R^2$  value is 1 so the data is perfect fit.

Table 4.3 Structure inside rapid prototyping specimen

Structure		
 Grid 30%	 Grid 50%	 Grid 70%
 Line 30%	 Line 50%	 Line 70%
 Triangle 30%	 Triangle 50%	 Triangle 70%

The structure in Table 4.2 produce the same result as (Patel, 2017), there are lesser amount of voids in the infill when increasing infill density. As can be observed from Table 4.2, the gap are getting closer in between the pattern from 30% to 70% infill percentage. The most void can be seen at 30% while the least void is at 70%. 50% void is in between 30% and 70%.

### 4.3 Table of data for tensile properties

The tabulated data is generated from Microsoft Excel by using Eq.3.3 to get the average value, Ultimate Tensile strength use Eq.3.1, Tensile stress at break gain by taking lowest stress value and Ductility at Ultimate Tensile Strength use Eq.3.4.

Table 4.4 Tensile properties for triangle pattern at 30% infill percentage

Sample	Ultimate Tensile strength	Tensile stress at break	Ductility at Ultimate Tensile Strength
	MPa	MPa	%
1	20.91	7.56	4.24
2	21.85	7.99	4.24
3	21.41	7.22	4.39
4	22.96	8.89	4.68
5	22.04	8.44	4.39
<b>Average</b>	21.83	8.02	4.39

Table 4.5 Tensile properties for triangle pattern at 50% infill percentage

Sample	Ultimate Tensile Strength	Tensile stress at break	Ductility at Ultimate Tensile Strength
	MPa	MPa	%
1	30.50	11.64	3.95
2	35.10	13.24	4.97
3	31.77	11.49	4.68
4	32.25	11.04	4.68
5	31.82	11.89	4.83
<b>Average</b>	32.29	11.86	4.62

Table 4.6 Tensile properties for triangle pattern at 70% infill percentage

Sample	Ultimate Tensile Strength	Tensile stress at break	Ductility at Ultimate Tensile Strength
	MPa	MPa	%
1	29.79	11.67	4.09
2	27.65	10.11	3.80
3	28.39	10.74	3.80
4	29.70	10.91	3.95
5	29.04	10.62	3.95
<b>Average</b>	28.91	10.81	3.92

Table 4.7 Tensile properties for line pattern at 30% infill percentage

Sample	Ultimate Tensile Strength	Tensile stress at break	Ductility at Ultimate Tensile Strength
	MPa	MPa	%
1	21.44	7.93	4.39
2	21.93	7.87	4.39
3	21.80	7.10	4.53
4	22.11	7.44	4.39
5	21.05	7.75	4.53
<b>Average</b>	21.66	7.62	4.44

Table 4.8 Tensile properties for line pattern at 50% infill percentage

Sample	Ultimate Tensile Strength	Tensile stress at break	Ductility at Ultimate Tensile Strength
	MPa	MPa	%
1	24.46	8.69	5.12
2	24.81	8.65	4.82
3	24.08	9.07	4.53
4	23.20	7.95	4.39
5	24.07	8.56	4.68
<b>Average</b>	24.12	8.58	4.71

Table 4.9 Tensile properties for line pattern at 70% infill percentage

Sample	Ultimate Tensile Strength	Tensile stress at break	Ductility at Ultimate Tensile Strength
	MPa	MPa	%
1	34.47	11.22	5.56
2	34.65	11.26	5.41
3	34.96	11.74	4.97
4	34.39	11.86	5.26
5	34.81	11.04	5.26
<b>Average</b>	34.66	11.42	5.29

Table 4.10 Tensile properties for grid pattern at 30% infill percentage

Sample	Ultimate Tensile Strength	Tensile stress at break	Ductility at Ultimate Tensile Strength
	MPa	MPa	%
1	25.39	8.88	4.53
2	25.29	8.80	4.53
3	27.03	10.13	4.68
4	26.52	9.10	4.53
5	25.80	8.84	4.97
<b>Average</b>	26.01	9.15	4.65

Table 4.11 Tensile properties for grid pattern at 50% infill percentage

Sample	Ultimate Tensile Strength	Tensile stress at break	Ductility at Ultimate Tensile Strength
	MPa	MPa	%
1	23.76	8.15	4.39
2	23.95	8.20	4.39
3	22.79	8.49	4.53
4	23.72	8.74	4.24
5	24.44	8.40	4.24
<b>Average</b>	23.73	8.40	4.36

Table 4.12 Tensile properties for grid pattern at 70% infill percentage

Sample	Ultimate Tensile Strength	Tensile stress at break	Ductility at Ultimate Tensile Strength
	MPa	MPa	%
1	33.50	11.86	5.12
2	33.64	11.78	4.68
3	33.04	11.56	4.68
4	34.45	11.97	4.68
5	34.55	13.17	4.68
<b>Average</b>	33.84	12.07	4.77

#### 4.4 Effect on Ultimate Tensile strength, Tensile stress at break and Ductility

Table 4.13 Complete average value of tensile properties

Type of Pattern	Infill Percentage (%)	Ultimate Tensile Strength (MPa)	Tensile Stress at Break (MPa)	Ductility at Ultimate Tensile Strength (%)
Triangle pattern	30	21.83	8.02	4.39
	50	32.29	11.86	4.62
	70	28.91	10.81	3.92
Line pattern	30	21.66	7.62	4.44
	50	24.12	8.58	4.71
	70	34.66	11.42	5.29
Grid pattern	30	26.01	9.15	4.65
	50	23.73	8.40	4.36
	70	33.84	12.07	4.77

Percentage different of UTS for Triangle pattern (30% – 50%)

$$= \frac{32.29MPa_{50\%} - 21.83MPa_{30\%}}{21.83MPa_{30\%}} \times 100\% = 47.92\% \text{ (increase)}$$

Eq.4.13

Percentage different of UTS for Triangle pattern (50% – 70%)

$$= \frac{28.91MPa_{70\%} - 32.29MPa_{50\%}}{32.29MPa_{50\%}} \times 100\% = -10.47\% \text{ (decrease)}$$

Eq.4.14

Percentage different of UTS for Line pattern (30% – 50%)

$$= \frac{24.12MPa_{50\%} - 21.66MPa_{30\%}}{21.66MPa_{30\%}} \times 100\% = 10.2\% \text{ (increase)}$$

Eq.4.15

Percentage different of UTS for Line pattern (50% – 70%)

$$= \frac{34.66MPa_{70\%} - 24.12MPa_{50\%}}{24.12MPa_{50\%}} \times 100\% = 43.7\% \text{ (increase)}$$

Eq.4.16

Percentage different of UTS for Grid pattern (30% – 50%)

$$= \frac{23.73MPa_{50\%} - 26.01MPa_{30\%}}{26.01MPa_{30\%}} \times 100\% = -9.61\% \text{ (decrease)}$$

Eq.4.17

Percentage different of UTS for Grid pattern (50% – 70%)

$$= \frac{33.84MPa_{70\%} - 23.73MPa_{50\%}}{23.73MPa_{50\%}} \times 100\% = 42.6\% \text{ (increase)}$$

Eq.4.18

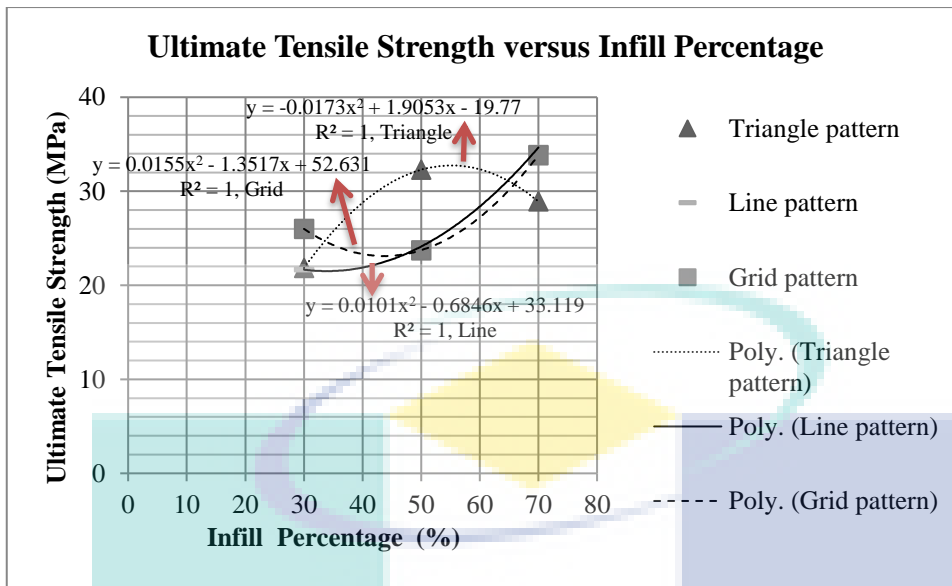


Figure 4.5 The graph of Ultimate Tensile Strength versus Infill Percentage

The graph in Figure 4.5 result show, the highest UTS value at 30% infill percentage is 26.01 MPa (Grid pattern), at 50% infill percentage is 32.29 MPa (Triangle pattern) and at 70% infill percentage is 34.66 MPa (Line pattern). All three trend are reliable data because  $R^2=1$ . The specimen UTS value mean that it can reach maximum stress value before start necking (Callister & Rethwisch, 2007). UTS for line pattern increase 10.2% when increasing infill percentage from 30% to 50% and increase 43.7% when increasing infill percentage from 50% to 70%. Line pattern result prove that by increasing the infill percentage, UTS value will increase too like in (Baich, 2015) result but they call infill percentage as infill density. Line pattern is not affected by the constant printing parameter(Layer height, printing temperature, buildplate temperature, diameter, print speed and travel speed) because UTS value increase by increasing infill percentage. Triangle pattern and Grid pattern are affected by constant printing parameter because it decrease -10.47% (50%-70%,Triangle) and -9.61% (30%-50%, Grid). Triangle pattern UTS value increase 47.92% (30%-50%) while Grid pattern increase 42.6% (50%-70% ). Hence, Triangle pattern affected by constant printing paramater when printing at 70% and Grid pattern when printing at 50%.



*Percentage different of Tensile Stress at Break for Triangle pattern*

*(30% – 50%)*

$$= \frac{11.86MPa_{50\%} - 8.02MPa_{30\%}}{8.02MPa_{30\%}} \times 100\% = 47.88\% \text{ (increase)} \quad \text{Eq.4.19}$$

*Percentage different of Tensile Stress at Break for Triangle pattern*

*(50% – 70%)*

$$= \frac{10.81MPa_{70\%} - 11.86MPa_{50\%}}{11.86MPa_{50\%}} \times 100\% = -8.85\% \text{ (decrease)} \quad \text{Eq.4.20}$$

*Percentage different of Tensile Stress at Break for Line pattern*

*(30% – 50%)*

$$= \frac{8.58MPa_{50\%} - 7.62MPa_{30\%}}{7.62MPa_{30\%}} \times 100\% = 12.6\% \text{ (increase)} \quad \text{Eq.4.21}$$

*Percentage different of Tensile Stress at Break for Line pattern*

*(50% – 70%)*

$$= \frac{11.42MPa_{70\%} - 8.58MPa_{50\%}}{8.58MPa_{50\%}} \times 100\% = 33.1\% \text{ (increase)} \quad \text{Eq.4.22}$$

*Percentage different of Tensile Stress at Break for Grid pattern*

*(30% – 50%)*

$$= \frac{8.40MPa_{50\%} - 9.15MPa_{30\%}}{9.15MPa_{30\%}} \times 100\% = -8.2\% \text{ (decrease)} \quad \text{Eq.4.23}$$

*Percentage different of Tensile Stress at Break for Grid pattern*

*(50 – 70%)*

$$= \frac{12.07MPa_{70\%} - 8.40MPa_{50\%}}{8.40MPa_{50\%}} \times 100\% = 43.7\% \text{ (increase)} \quad \text{Eq.4.24}$$

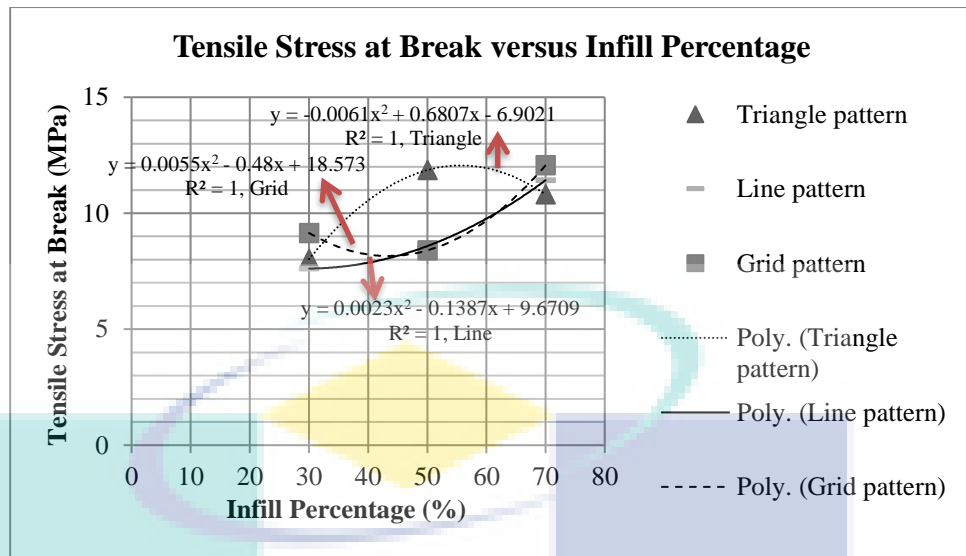


Figure 4.6 The graph of Tensile Stress at Break versus Infill Percentage

The highest Tensile Stress at Break in Figure 4.6 at 30% infill percentage is 9.15 MPa (Grid pattern), 50% infill percentage is 11.86 MPa (Triangle pattern) and 70% infill percentage is 12.07 MPa (Grid pattern). Tensile Stress at Break is the tensile stress at the point where the specimen completely fracture or call as breaking point(PhysicsNet.co.uk, 2010). All three trend are reliable data because  $R^2=1$ . Tensile Stress at Break for line pattern increase 12.6% when increasing infill percentage from 30% to 50% and increase 33.1% when increasing infill percentage from 50% to 70%. The polynomial trend increase steadily in line pattern, this prove that the UTS value of line pattern in Figure 4.5 is relevant because it can extend the breaking point by increasing infill percentage. Line pattern is not affected by the constant printing parameter(Layer height, printing temperature, buildplate temperature, diameter, print speed and travel speed) because Tensile Stress at Break value increase by increasing infill percentage. Triangle pattern and Grid pattern are affected by constant printing parameter because it decrease -8.85% (50%-70%,Triangle) and -9.61% (30%-50%, Grid). Triangle pattern Tensile Stress at Break value increase 47.88% (30%-50%) while Grid pattern increase 43.7% (50%-70%). Hence, Triangle pattern affected by constant printing parameter when printing at 70% and Grid pattern when printing at 50%.

$$\begin{aligned} & \text{Percentage different of Ductility at UTS for Triangle pattern (30\% - 50\%)} \\ & = \frac{4.62_{50\%} - 4.39_{30\%}}{4.39_{30\%}} \times 100\% = 5.24\% \text{ (increase)} \end{aligned} \quad \text{Eq.4.25}$$

$$\begin{aligned} & \text{Percentage different of Ductility at UTS for Triangle pattern (50\% - 70\%)} \\ & = \frac{3.92_{70\%} - 4.62_{50\%}}{4.62_{50\%}} \times 100\% = -15.15\% \text{ (decrease)} \end{aligned} \quad \text{Eq.4.26}$$

$$\begin{aligned} & \text{Percentage different of Ductility at UTS for Line pattern (30\% - 50\%)} \\ & = \frac{4.71_{50\%} - 4.44_{30\%}}{4.44_{30\%}} \times 100\% = 6.08\% \text{ (increase)} \end{aligned} \quad \text{Eq.4.27}$$

$$\begin{aligned} & \text{Percentage different of Ductility at UTS for Line pattern (50\% - 70\%)} \\ & = \frac{5.29_{70\%} - 4.71_{50\%}}{4.71_{50\%}} \times 100\% = 12.31\% \text{ (increase)} \end{aligned} \quad \text{Eq.4.28}$$

$$\begin{aligned} & \text{Percentage different of Ductility at UTS for Grid pattern (30\% - 50\%)} \\ & = \frac{4.36_{50\%} - 4.65_{30\%}}{4.65_{30\%}} \times 100\% = -6.24\% \text{ (decrease)} \end{aligned} \quad \text{Eq.4.29}$$

$$\begin{aligned} & \text{Percentage different of Ductility at UTS for Grid pattern} \\ & \text{(50 - 70\%)} \\ & = \frac{4.77_{70\%} - 4.36_{50\%}}{4.36_{50\%}} \times 100\% = 9.4\% \text{ (increase)} \end{aligned} \quad \text{Eq.4.30}$$

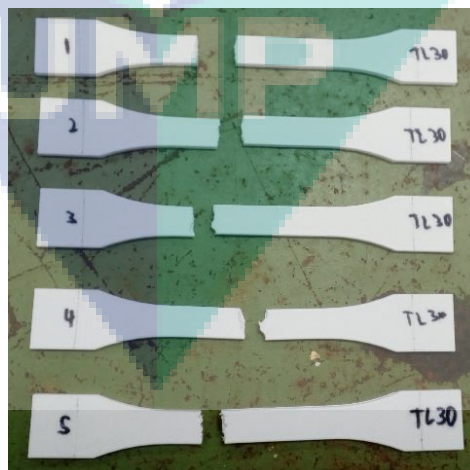


Figure 4.7 ASTM D638-10 after tensile test

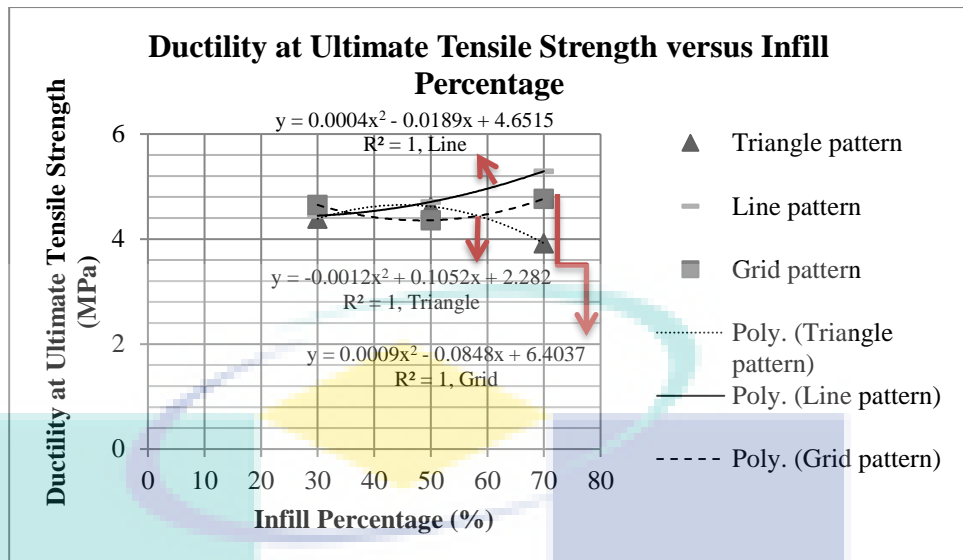


Figure 4.8 The graph of Ductility at Ultimate Tensile Strength versus Infill Percentage

Figure 4.8 show highest Ductility at Ultimate Tensile Strength for 30% infill percentage is 4.65% (Grid pattern), 50% infill percentage is 4.71 % (Line pattern) and 70% infill percentage is 5.29% (Line pattern). Ductility is measure of the degree of plastic deformation continuous at breaking point(Callister & Rethwisch, 2007). All three trend are reliable data because  $R^2=1$ . Ductility at Ultimate Tensile Strength for line pattern increase 6.08% when increasing infill percentage from 30% to 50% and increase 12.31% when increasing infill percentage from 50% to 70%. The polynomial trend increase progressively in line pattern. Line pattern is not affected by the constant printing parameter(Layer height, printing temperature, buildplate temperature, diameter, print speed and travel speed) because Ductility at Ultimate Tensile increase by increasing infill percentage. Triangle pattern and Grid pattern are affected by constant printing parameter because it decrease -15.15%(50%-70%,Triangle) and -6.24% (30%-50%, Grid). Triangle pattern Tensile Stress at Break value increase 5.24% (30%-50%) while Grid pattern increase 9.4%(50%-70%). Hence, Triangle pattern affected by constant printing paramater when printing at 70% and Grid pattern when printing at 50%.

#### 4.5 Table of data for flexural properties

The tabulated data is from Microsoft Excel by using Eq.3.3 to get the average value. The Flexural stress and Flexural Modulus value are auto generated by Instron Bluehill software.

Table 4.14 Flexural properties for triangle pattern at 30% infill percentage

Sample	Flexural stress	Flexural Modulus
	MPa	MPa
1	30.88	1312.94
2	27.65	1220.68
3	31.71	1332.36
4	34.88	1487.37
5	35.66	1549.16
<b>Average</b>	32.16	1380.5

Table 4.15 Flexural properties for triangle pattern at 50% infill percentage

Sample	Flexural stress	Flexural Modulus
	MPa	MPa
1	29.95	1411.17
2	32.26	1525.13
3	34.45	1533.11
4	37.79	1718.83
5	32.87	1529.99
<b>Average</b>	33.46	1543.65

Table 4.16 Flexural properties for triangle pattern at 70% infill percentage

Sample	Flexural stress	Flexural Modulus
	MPa	MPa
1	20.6	972.28
2	25.93	1140.98
3	28.56	1178.1
4	25.66	1152.79
5	29.66	1246.07
<b>Average</b>	26.08	1138.04

Table 4.17 Flexural properties for line pattern at 30% infill percentage

Sample	Flexural stress	Flexural Modulus
	MPa	MPa
1	51.98	1969.93
2	51.95	1912.49
3	48.31	1804.95
4	48.04	1824.14
5	34.92	1377.69
<b>Average</b>	47.04	1777.84

Table 4.18 Flexural properties for line pattern at 50% infill percentage

Sample	Flexural stress	Flexural Modulus
	MPa	MPa
1	57.13	2252.66
2	54.69	2058.97
3	50.59	1971.32
4	54.86	2155.28
5	57.17	2150.21
<b>Average</b>	54.89	2117.69

Table 4.19 Flexural properties for line pattern at 70% infill percentage

Sample	Flexural stress	Flexural Modulus
	MPa	MPa
1	23.34	938.6
2	19.74	811.83
3	7.79	143.23
4	18.07	816.45
5	4.29	120.46
<b>Average</b>	14.65	566.12

Table 4.20 Flexural properties for grid pattern at 30% infill percentage

Sample	Flexural stress	Flexural Modulus
	MPa	MPa
1	50.71	2040.05
2	49.86	1989.11
3	51.26	2038.94
4	49.13	1943.11
5	52.78	2171.75
<b>Average</b>	50.75	2036.59

Table 4.21 Flexural properties for grid pattern at 50% infill percentage

Sample	Flexural stress	Flexural Modulus
	MPa	MPa
1	57.39	2265.8
2	49.75	2024.96
3	55.82	2207.57
4	56.16	2265.34
5	53.3	2069.59
<b>Average</b>	54.48	2166.65

Table 4.22 Flexural properties for grid pattern at 70% infill percentage

Sample	Flexural stress	Flexural Modulus
	MPa	MPa
1	57.27	2008.41
2	56.73	2340.37
3	51.47	2092.39
4	58.2	2489.16
5	59.26	2462.07
<b>Average</b>	56.59	2278.48

#### 4.6 Effect on Flexural Stress and Flexural Modulus

Table 4.23 Complete average value of flexural properties

Pattern	Infill percentage (%)	Flexural Stress (MPa)	Flexural Modulus (MPa)
Triangle pattern	30	32.16	1,380.50
	50	33.46	1,543.65
	70	26.08	1,138.04
Line pattern	30	47.04	1,777.84
	50	54.89	2,117.69
	70	14.65	566.12
Grid pattern	30	50.75	2,036.59
	50	54.48	2,166.65
	70	56.59	2,278.48

$$\begin{aligned} & \text{Percentage different of Flexural Stress for Triangle pattern (30\% – 50\%)} \\ & = \frac{33.46MPa_{50\%} - 32.16MPa_{30\%}}{32.16MPa_{30\%}} \times 100\% = 4.04\% \text{ (increase)} \end{aligned} \quad \text{Eq.4.31}$$

$$\begin{aligned} & \text{Percentage different of Flexural Stress for Triangle pattern (50\% – 70\%)} \\ & = \frac{26.08MPa_{70\%} - 33.46MPa_{50\%}}{33.46MPa_{50\%}} \times 100\% = -22.06\% \text{ (decrease)} \end{aligned} \quad \text{Eq.4.32}$$

$$\begin{aligned} & \text{Percentage different of Flexural Stress for Line pattern (30\% – 50\%)} \\ & = \frac{54.89MPa_{50\%} - 47.04MPa_{30\%}}{47.04MPa_{30\%}} \times 100\% = 16.69\% \text{ (increase)} \end{aligned} \quad \text{Eq.4.33}$$

$$\begin{aligned} & \text{Percentage different of Flexural Stress for Line pattern (50\% – 70\%)} \\ & = \frac{14.65MPa_{70\%} - 54.89MPa_{50\%}}{54.89MPa_{50\%}} \times 100\% = -73.31\% \text{ (decrease)} \end{aligned} \quad \text{Eq.4.34}$$

$$\begin{aligned} & \text{Percentage different of Flexural Stress for Grid pattern (30\% – 50\%)} \\ & = \frac{54.48MPa_{50\%} - 50.75MPa_{30\%}}{50.75MPa_{30\%}} \times 100\% = 7.35\% \text{ (increase)} \end{aligned} \quad \text{Eq.4.35}$$

$$\begin{aligned} & \text{Percentage different of Flexural Stress for Grid pattern (50 – 70\%)} \\ & = \frac{56.59MPa_{70\%} - 54.48MPa_{50\%}}{54.48MPa_{50\%}} \times 100\% = 3.87\% \text{ (increase)} \end{aligned} \quad \text{Eq.4.36}$$



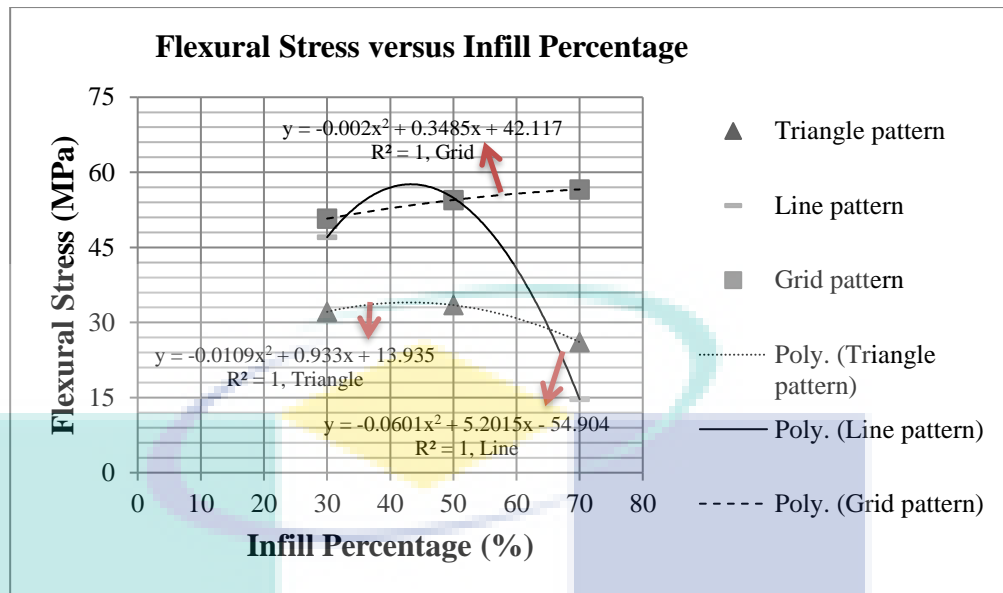


Figure 4.9 The graph of Flexural Stress versus Infill Percentage

The graph in Figure 4.9 represent the result for highest Flexural Stress at 30% infill percentage is 50.75 MPa (Grid pattern), at 50% infill percentage is 54.89 MPa (Line pattern) and 70% infill percentage is 56.59 MPa (Grid pattern). Flexural Stress is the ability of the material to withstand bending forces applied perpendicular to its longitudinal axis (S.R. Djafari Petroudy, 2017). All three trend are reliable data because  $R^2=1$ . Flexural Stress for grid pattern increase 7.35% when increasing infill percentage from 30% to 50% and increase 3.87% when increasing infill percentage from 50% to 70%. The polynomial trend increase gently in grid pattern. Grid pattern is not affected by the constant printing parameter (Layer height, printing temperature, buildplate temperature, diameter, print speed and travel speed) because Flexural Stress value increase by increasing infill percentage. Triangle pattern and line pattern are affected by constant printing parameter because it decrease -22.06% (50%-70%, Triangle) and -73.31 (50%-70%, Line). Triangle pattern Tensile Stress at Break value increase 4.04% (30%-50%) while line pattern increase 16.69% (30%-50%). Hence, Triangle pattern and line pattern are affected by constant printing parameter when printing at 70% .

*Percentage different of Flexural Modulus for Triangle pattern (30% – 50%)*

$$= \frac{1,543.65MPa_{50\%} - 1,380.50MPa_{30\%}}{1,380.50MPa_{30\%}} \times 100\% = 11.82\% \text{ (increase)} \quad \text{Eq.4.37}$$

*Percentage different of Flexural Modulus for Triangle pattern (50% – 70%)*

$$= \frac{1,138.04MPa_{70\%} - 1,543.65MPa_{50\%}}{1,543.65MPa_{50\%}} \times 100\% = -26.28\% \text{ (decrease)} \quad \text{Eq.4.38}$$

*Percentage different of Flexural Modulus for Line pattern (30% – 50%)*

$$= \frac{2,117.69MPa_{50\%} - 1,777.84MPa_{30\%}}{1,777.84MPa_{30\%}} \times 100\% = 19.12\% \text{ (increase)} \quad \text{Eq.4.39}$$

*Percentage different of Flexural Modulus for Line pattern (50% – 70%)*

$$= \frac{566.12MPa_{70\%} - 2,117.69MPa_{50\%}}{2,117.69MPa_{50\%}} \times 100\% = -73.28\% \text{ (decrease)} \quad \text{Eq.4.40}$$

*Percentage different of Flexural Modulus for Grid pattern (30% – 50%)*

$$= \frac{2,166.65MPa_{50\%} - 2,036.59MPa_{30\%}}{2,036.59MPa_{30\%}} \times 100\% = 6.39\% \text{ (increase)} \quad \text{Eq.4.41}$$

*Percentage different of Flexural Modulus for Grid pattern (50 – 70%)*

$$= \frac{2,278.48MPa_{70\%} - 2,166.65MPa_{50\%}}{2,166.65MPa_{50\%}} \times 100\% = 5.16\% \text{ (increase)} \quad \text{Eq.4.42}$$

UMP

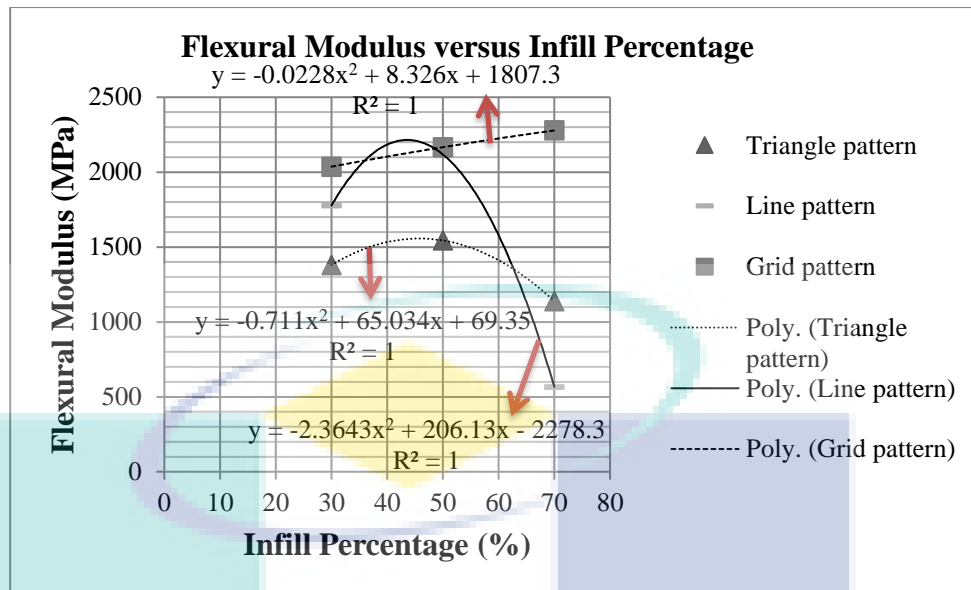


Figure 4.10 The graph of Flexural Modulus versus Infill Percentage

The result in Figure 4.10 show the highest Flexural Modulus at 30% infill percentage is 2036.59 MPa (Grid pattern), at 50% infill percentage is 2166.65 MPa (Grid pattern) and 70% infill percentage is 2278.48 MPa (Grid pattern). Flexural Modulus is a measure of the stiffness during the first or initial step of the bending process (James J. Licari, 2005). All three trend are reliable data because  $R^2=1$ . Flexural Stress for grid pattern increase 6.39% when increasing infill percentage from 30% to 50% and increase 5.16% when increasing infill percentage from 50% to 70%. The polynomial trend increase moderately in grid pattern. Grid pattern is not affected by the constant printing parameter (Layer height, printing temperature, buildplate temperature, diameter, print speed and travel speed) because Flexural Stress value increase by increasing infill percentage. Triangle pattern and line pattern are affected by constant printing parameter because it decrease -26.28% (50%-70%, Triangle) and -73.28 (50%-70%, Line). Triangle pattern Tensile Stress at Break value increase 11.82% (30%-50%) while line pattern increase 19.12% (30%-50%). Hence, Triangle pattern and line pattern are affected by constant printing parameter when printing at 70% .

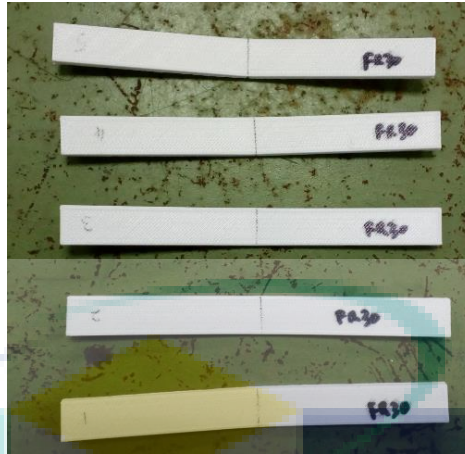


Figure 4.11 ASTM D790-10 after flexural test

#### 4.7 Summary

Time taken to print, length of filament used and weight of specimen increases when increasing infill percentage. Type of infill pattern and constant printing parameter does affect the printing time graph for ASTM D638-10 and ASTM D790-10 sample because the polynomial trend is gradually increase when increasing infill percentage. ASTM D638-10 sample prove the time taken to print 1 sample increase 8.89% when increasing infill percentage from 30% to 50% and increase 6.12% when increasing infill percentage from 50% to 70%. ASTM D790-10 sample prove the time taken to print 1 sample increase 8% when increasing infill percentage from 30% to 50% and increase 3.7% when increasing infill percentage from 50% to 70%. There are lesser amount of voids in the infill when increasing infill density because the gap are getting closer in between the pattern from 30% to 70% infill percentage. The most void can be seen at 30% while the least void is at 70%. 50% void is in between 30% and 70%.

Effect on tensile properties, the highest UTS value at 30% infill percentage is 26.01 MPa (Grid pattern), at 50% infill percentage is 32.29 MPa (Triangle pattern) and at 70% infill percentage is 34.66 MPa (Line pattern). The highest Tensile Stress at Break in Figure 4.6 at 30% infill percentage is 9.15 MPa (Grid pattern), 50% infill percentage is 11.86 MPa (Triangle pattern) and 70% infill percentage is 12.07 MPa (Grid pattern). Highest Ductility at Ultimate Tensile Strength for 30% infill percentage is 4.65% (Grid pattern), 50% infill percentage is 4.71% (Line pattern) and 70% infill percentage is 5.29% (Line pattern). After comparing three polynomial graph, it conclude that line pattern is not affected by the constant printing parameter(Layer height, printing temperature, buildplate temperature, diameter, print speed and travel speed) because tensile properties value increase by increasing infill percentage but triangle pattern is affected by constant printing parameter when printing at 70% and grid pattern when printing at 50% due to decreasing tensile properties value.

Effect on flexural properties, the highest Flexural Stress at 30% infill percentage is 50.75 MPa (Grid pattern), at 50% infill percentage is 54.89 MPa(Line pattern) and 70% infill percentage is 56.59 MPa (Grid pattern) . Highest Flexural Modulus at 30% infill percentage is 2036.59 MPa (Grid pattern), at 50% infill percentage is 2166.65 MPa (Grid pattern) and 70% infill percentage is 2278.48 MPa (Grid pattern). After comparing two polynomial graph, it conclude that grid pattern is not affected by the constant printing parameter(Layer height, printing temperature, buildplate temperature, diameter, print speed and travel speed) because flexural properties value increase by increasing infill percentage but triangle pattern and line pattern are affected by constant printing parameter when printing at 70% due to decreasing flexural properties value.

## CHAPTER 5

### CONCLUSION

#### 5.1 Introduction

In this chapter, all the result and discussion from chapter 4 will be concluded based on the research objective. Recommendation also will be given for future studies to explore more printing parameter that affect the mechanical properties.

#### 5.2 Conclusion

In conclusion after conducting tensile and flexural test, I manage to study the effect of different infill percentage toward mechanical properties and printing parameter that stated in first objective and also second objective that require to study the effect of different infill pattern toward mechanical properties and printing parameter. Both objective has been achieve when plotting polynomial graph . Mechanical properties that are being considered are tensile properties(Ultimate Tensile Strength, Tensile Stress at Break, Ductility) and flexural properties (Flexural Stress, Flexural Modulus) while infill pattern are grid, line and triangle. The constant printing parameter are layer height, printing temperature, buildplate temperature, diameter, print speed and travel speed. After comparing three polynomial graph result for tensile properties, I found that line pattern is not affected by the constant printing parameter because tensile properties value increase by increasing infill percentage but triangle pattern is affected by constant printing parameter when printing at 70% and grid pattern when printing at 50% due to decreasing tensile properties value. Hence, this prove that line pattern perform best in tensile properties when increasing infill percentage with constant printing parameter.

Next, after comparing two polynomial graph for flexural properties, I found that grid pattern is not affected by the constant printing parameter because flexural properties value increase by increasing infill percentage but triangle pattern and line pattern are affected by constant printing parameter when printing at 70% due to decreasing flexural properties value. Hence, this prove that grid pattern perform best in flexural properties when increasing infill percentage with constant printing parameter.

### 5.3 Recommendation

There are several recommendation for future studies to explore more printing parameter that can affect the mechanical properties of the rapid prototyping specimen which are:

- i. Shells, the number of layers on the outside of a print.
- ii. Wiggle, infill pattern
- iii. Printing temperature



UMP

## REFERENCES

- Alvarez C., K. L., Lagos C., R. F., & Aizpun, M. (2016). Investigando la influencia del porcentaje de relleno en las propiedades mecánicas, de elementos impresos con ABS por el método de modelado por deposición fundida. *Ingeniería E Investigacion*, 36(3), 110–116. <https://doi.org/10.15446/ing.investig.v36n3.56610>
- Anon(Ultimaker). (2016). Speed | Professional 3D printing made accessible | Ultimaker. Retrieved from <https://ultimaker.com/en/resources/20419-speed>
- Baich, L. (2015). Study of infill print design on production cost-time of 3D printed ABS parts Study of infill print design on production cost-time of 3D printed ABS parts Liseli Baich , Guha Manogharan \* and Hazel Marie, (December). <https://doi.org/10.1504/IJRAPIDM.2015.074809>
- Cain, P. (2018). Selecting the optimal shell and infill parameters for FDM 3D Printing | 3D Hubs. Retrieved from <https://www.3dhubs.com/knowledge-base/selecting-optimal-shell-and-infill-parameters-fdm-3d-printing>
- Callister, W., & Rethwisch, D. (2007). *Materials science and engineering: an introduction. Materials Science and Engineering* (Vol. 94). [https://doi.org/10.1016/0025-5416\(87\)90343-0](https://doi.org/10.1016/0025-5416(87)90343-0)
- Carneiro, O. S., Silva, A. F., & Gomes, R. (2015). Fused deposition modeling with polypropylene. *Materials and Design*, 83, 768–776. <https://doi.org/10.1016/j.matdes.2015.06.053>
- Christ, S., Schnabel, M., Vorndran, E., Groll, J., & Gbureck, U. (2015). Fiber reinforcement during 3D printing. *Materials Letters*, 139, 165–168. <https://doi.org/10.1016/j.matlet.2014.10.065>
- Cooper, K. G. (2001). *Rapid Prototyping Technology: Selection and Application*. Retrieved from [www.dekker.com](http://www.dekker.com)
- Ćwikła, G., Grabowik, C., Kalinowski, K., Paprocka, I., & Ociepka, P. (2017). The influence of printing parameters on selected mechanical properties of FDM/FFF 3D-printed parts. *IOP Conference Series: Materials Science and Engineering*, 227(1). <https://doi.org/10.1088/1757-899X/227/1/012033>
- Dassault Systèmes SolidWorks Corporation. (2018). 3D CAD | SOLIDWORKS. Retrieved June 6, 2018, from <https://www.solidworks.com/category/3d-cad>

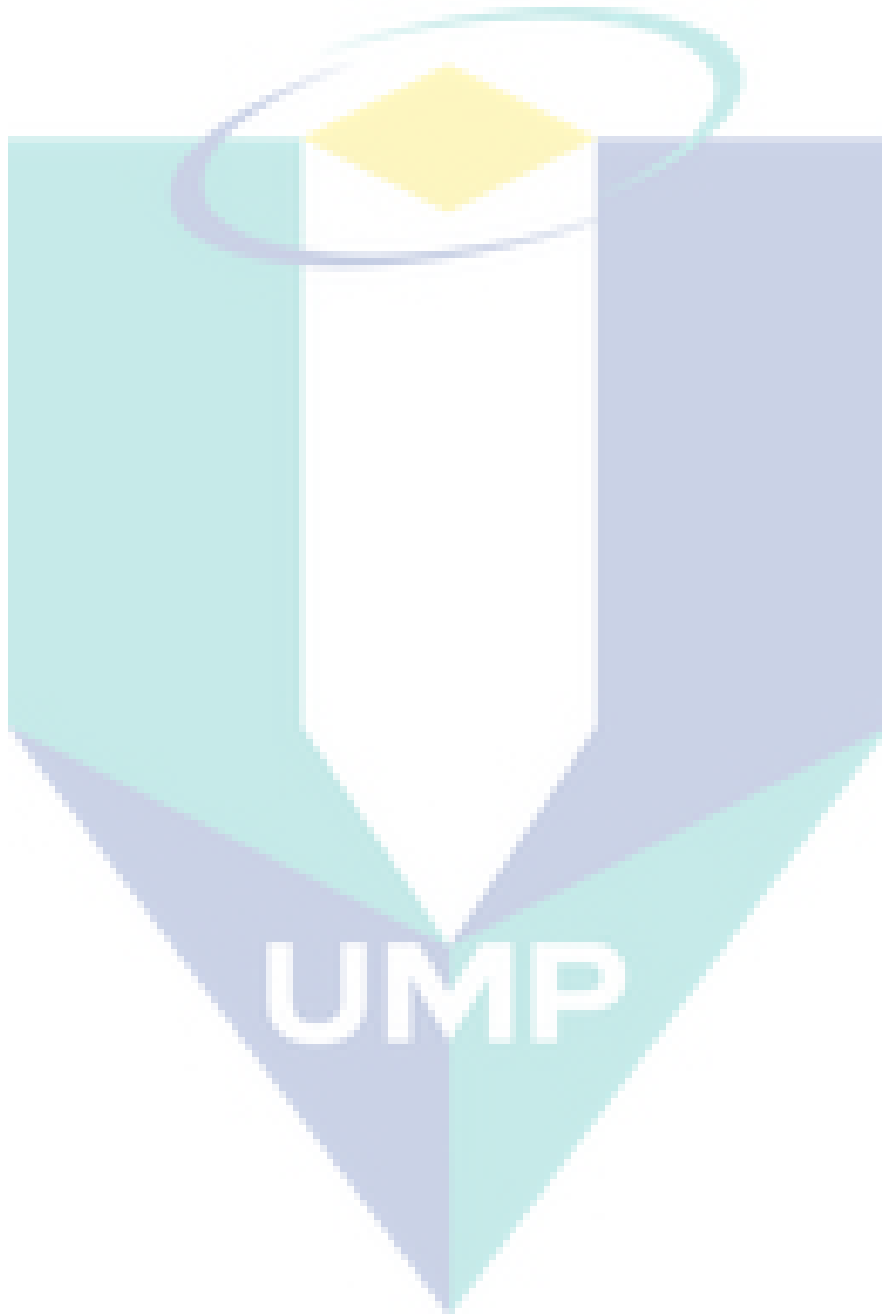


- Der Klift, F. Van, Koga, Y., Todoroki, A., Ueda, M., Hirano, Y., & Matsuzaki, R. (2016). 3D Printing of Continuous Carbon Fibre Reinforced Thermo-Plastic (CFRTP) Tensile Test Specimens. *Open Journal of Composite Materials*, 6(1), 18–27. <https://doi.org/10.4236/ojcm.2016.61003>
- Filaments.ca. (2014). 3D Printing Temperatures & Printing Guidelines – Filaments.ca. Retrieved from <https://filaments.ca/pages/temperature-guide>
- Forster, A. M. (2015). Materials Testing Standards for Additive Manufacturing of Polymer Materials: State of the Art and Standards Applicability. <https://doi.org/10.6028/NIST.IR.8059>
- Gibson, I., Rosen, D. W., & Stucker, B. (2010). *Additive Manufacturing Technologies. Climate Change 2013 - The Physical Science Basis* (Vol. 31). <https://doi.org/10.1007/978-1-4419-1120-9>
- GmbH, E. (2018). Tensile strength at break. Retrieved from <https://www.ensingerplastics.com/en/shapes/engineering-solutions/mechanical-properties>
- Ivey, M., Melenka, G. W., Carey, J. P., & Ayranci, C. (2017). Characterizing short-fiber-reinforced composites produced using additive manufacturing. *Advanced Manufacturing: Polymer & Composites Science*, 340(September), 1–11. <https://doi.org/10.1080/20550340.2017.1341125>
- James J. Licari, D. W. S. (2005). flexural modulus - an overview | ScienceDirect Topics. Retrieved May 25, 2018, from <https://www.sciencedirect.com/topics/chemistry/flexural-modulus>
- Lanzotti, A., Grasso, M., Staiano, G., & Martorelli, M. (2015). The impact of process parameters on mechanical properties of parts fabricated in PLA with an open-source 3-D printer. *Rapid Prototyping Journal*, 21(5), 604–617. <https://doi.org/10.1108/RPJ-09-2014-0135>
- Li, N., Li, Y., & Liu, S. (2016). Rapid prototyping of continuous carbon fiber reinforced polylactic acid composites by 3D printing. *Journal of Materials Processing Technology*, 238, 218–225. <https://doi.org/10.1016/j.jmatprotec.2016.07.025>
- Melenka, G. W., Cheung, B. K. O., Schofield, J. S., Dawson, M. R., & Carey, J. P. (2016). Evaluation and prediction of the tensile properties of continuous fiber-reinforced 3D printed structures. *Composite Structures*, 153, 866–875. <https://doi.org/10.1016/j.compstruct.2016.07.018>

- Milosevic, M., Stoof, D., & Pickering, K. L. (2017). Characterizing the Mechanical Properties of Fused Deposition Modelling Natural Fiber Recycled Polypropylene Composites. <https://doi.org/10.3390/jcs1010007>
- Morton, W. E., & Hearle, J. W. S. (2008). Tensile properties. <https://doi.org/10.1533/9781845694425.274>
- NDT Resource Center. (2018). Tensile Properties. Retrieved June 6, 2018, from <https://www.nde-ed.org/EducationResources/CommunityCollege/Materials/Mechanical/Tensile.php>
- Ning, F., Cong, W., Qiu, J., Wei, J., & Wang, S. (2015). Additive manufacturing of carbon fiber reinforced thermoplastic composites using fused deposition modeling. *Composites Part B: Engineering*, 80, 369–378. <https://doi.org/10.1016/j.compositesb.2015.06.013>
- Patel, D. M. (2017). Effects of Infill Patterns on Time , Surface Roughness and Tensile Strength in 3D Printing, 5(3), 566–569.
- Pearce, J. M., Morris Blair, C., Laciak, K. J., Andrews, R., Nosrat, A., & Zelenika-Zovko, I. (2010). 3-D Printing of Open Source Appropriate Technologies for Self-Directed Sustainable Development. *Journal of Sustainable Development*, 3(4), 17–29. <https://doi.org/10.5539/jsd.v3n4p17>
- Percentage, I. (2017). 3D Printing Tech Tips : Infill Percentage And Pattern Explained. Retrieved from <https://3dplatform.com/3d-printing-tech-tips-infill-percentage-and-pattern-explained/>
- PhysicsNet.co.uk. (2010). Stress & Strain – tensile stress, tensile strain, elastic strain energy, breaking stress, plastic , brittle. Retrieved May 17, 2018, from <http://physicsnet.co.uk/a-level-physics-as-a2/materials/stress-strain/>
- S.R. Djafari Petroudy. (2017). Flexural Strength - an overview | ScienceDirect Topics. Retrieved May 25, 2018, from <https://www.sciencedirect.com/topics/materials-science/flexural-strength>
- Sculpteo. (2018). Layer Thickness : Precision of 3D Printing. Retrieved from <https://www.sculpteo.com/en/glossary/layer-thickness-definition/>
- Song, Y., Li, Y., Song, W., Yee, K., Lee, K. Y., & Tagarielli, V. L. (2017). Measurements of the mechanical response of unidirectional 3D-printed PLA. *Materials and Design*, 123, 154–164. <https://doi.org/10.1016/j.matdes.2017.03.051>


- Tekinalp, H. L., Kunc, V., Velez-Garcia, G. M., Duty, C. E., Love, L. J., Naskar, A. K., ... Ozcan, S. (2014). Highly oriented carbon fiber-polymer composites via additive manufacturing. *Composites Science and Technology*, *105*, 144–150. <https://doi.org/10.1016/j.compscitech.2014.10.009>
- To, A. (2015). Choosing the best trendline for your data. *Microsoft*. Retrieved from <https://support.office.com/en-us/article/choosing-the-best-trendline-for-your-data-1bb3c9e7-0280-45b5-9ab0-d0c93161daa8>
- Torrado, A. R., Shemelya, C. M., English, J. D., Lin, Y., Wicker, R. B., & Roberson, D. A. (2015). Characterizing the effect of additives to ABS on the mechanical property anisotropy of specimens fabricated by material extrusion 3D printing. *Additive Manufacturing*, *6*, 16–29. <https://doi.org/10.1016/j.addma.2015.02.001>
- Tymrak, B. M., Kreiger, M., & Pearce, J. M. (2014). Mechanical properties of components fabricated with open-source 3-D printers under realistic environmental conditions. *Materials and Design*, *58*, 242–246. <https://doi.org/10.1016/j.matdes.2014.02.038>
- Wang, J., Xie, H., Weng, Z., Senthil, T., & Wu, L. (2016). A novel approach to improve mechanical properties of parts fabricated by fused deposition modeling. *JMADE*, *105*, 152–159. <https://doi.org/10.1016/j.matdes.2016.05.078>
- Wang, L., Gramlich, W. M., & Gardner, D. J. (2017). Improving the impact strength of Poly(lactic acid) (PLA) in fused layer modeling (FLM). *Polymer (United Kingdom)*, *114*, 242–248. <https://doi.org/10.1016/j.polymer.2017.03.011>
- Weng, Z., Wang, J., Senthil, T., & Wu, L. (2016). Mechanical and thermal properties of ABS / montmorillonite nanocomposites for fused deposition modeling 3D printing. *JMADE*, *102*, 276–283. <https://doi.org/10.1016/j.matdes.2016.04.045>
- Yang, C., Tian, X., Liu, T., Cao, Y., & Li, D. (2017). 3D printing for continuous fiber reinforced thermoplastic composites: mechanism and performance. *Rapid Prototyping Journal*, *23*(1), 209–215. <https://doi.org/10.1108/RPJ-08-2015-0098>

**APPENDIX A : PUBLISHED PAPERS**



# The energy-absorbing characteristics of filament wound hybrid carbon fiber-reinforced plastic/polylactic acid tubes with different infill pattern structures

Journal of Reinforced Plastics and Composites  
0(0) 1–22  
© The Author(s) 2019  
Article reuse guidelines:  
sagepub.com/journals-permissions  
DOI: 10.1177/0731684419868018  
journals.sagepub.com/home/jrp  
SAGE

MA Quanjin<sup>1,2</sup>, Idris M Sahat<sup>1</sup>, Mohd R Mat Rejab<sup>1,2</sup> , Shukur Abu Hassan<sup>3</sup>, Bo Zhang<sup>2</sup> and Mubin NM Merzuki<sup>1</sup>

## Abstract

The study aims to investigate the effect of different infill pattern structures on the energy-absorbing characteristics of single filament wound carbon fiber-reinforced plastic tubes, single polylactic acid and hybrid carbon fiber-reinforced plastic/polylactic acid tubes under quasi-static axial compression condition, which were fabricated using filament winding and additive manufacturing techniques. Five infill pattern structures of single polylactic acid tubes and hybrid tubes were studied and compared on their energy-absorbing characteristics, which referred to normal, triangle, square, hexagonal and tetrahedral patterns. It concluded that the effect of the infill pattern structure had a significant influence on energy-absorbing characteristics of single polylactic acid and hybrid carbon fiber-reinforced plastic/polylactic acid tubes. For pure polylactic acid tubes, the triangle infill pattern tube represented the highest values of energy absorption ( $EA$ ) of 0.75 kJ, specific energy absorption ( $SEA$ ) of 28.50 J/g, compressive strength and modulus of 69.72 MPa and 1.40 GPa, yield strength of 27.80 MPa, peak crushing force ( $F_{peak}$ ) of 23.13 kN and mean crushing force ( $F_{mean}$ ) of 18.82 kN. For the hybrid carbon fiber-reinforced plastic/polylactic acid tube, tetrahedral infill pattern tube showed the highest values of  $EA$  with 0.99 kJ,  $SEA$  with 29.66 J/g,  $F_{peak}$  with 22.68 MPa and yield strength with 29.91 MPa. Energy absorption interaction ( $EA_{interaction}$ ) and interaction ratio ( $\varphi_e$ ) of all specimens were evaluated, which showed that the tetrahedral infill pattern tube recorded the highest of all hybrid tubes with 259.92 J and 35.72 %. The result revealed that the tetrahedral pattern displayed better crashworthiness in terms of crushing force efficiency ( $CFE$ ),  $EA$  and  $SEA$  in the hybrid structure, which had greater potential to apply as energy absorbers. Moreover, triangle and square infill patterns of hybrid tubes provided the negative interaction effect results, which conducted lower energy-absorbing characteristics compared to individual tubes, respectively.

## Keywords

Carbon fiber-reinforced plastic, hybrid carbon fiber-reinforced plastic/polylactic acid tube, infill pattern structure, energy-absorbing characteristics

## Introduction

For the advanced crashworthiness and energy-absorbing characteristics, composite structures have been developed as energy absorbers to increase the safety-conscious conditions in modern transportation.<sup>1</sup> Numerous experimental and theoretical findings have advanced energy-absorbing characteristics of the hybrid structures over the past several decades, which commonly selected various materials such as metals and different types of polymers.<sup>2–7</sup> The commercial applications of the thin-walled structure have mostly

<sup>1</sup>Faculty of Mechanical & Manufacturing Engineering, Universiti Malaysia Pahang, Pahang, Malaysia

<sup>2</sup>School of Mechanical Engineering, Ningxia University, Yinchuan, China

<sup>3</sup>Centre for Advanced Composite Materials, Faculty of Engineering, Universiti Teknologi Malaysia, Skudai, Johor, Malaysia

## Corresponding authors:

Mohd R Mat Rejab, Universiti Malaysia Pahang, Pekan 26600, Pahang, Malaysia.

Email: ruzaimi@ump.edu.my

Ma Quanjin, Universiti Malaysia Pahang, Pekan 26600, Pahang, Malaysia.

Email: neromaquanjin@gmail.com

been used as energy absorption (*EA*) such as webbed fuselage structures,<sup>8</sup> steering columns,<sup>9</sup> landing gears of helicopters,<sup>10</sup> and crash boxes.<sup>11–13</sup> Recently, lightweight energy-absorbing structures gained increasing attention for meeting the higher requirements of crashworthiness in the automotive and aerospace aspects. Therefore, it is an essential problem to reduce structure weight while providing higher energy-absorbing characteristics to increase the vehicle crash safety once accident occurs. Based on this purpose, lightweight materials such as composite and potential plastics gradually have higher opportunity to replace the metal materials in the modern automotive industries.

Plastic materials, such as polylactic acid (PLA) and acrylonitrile butadiene styrene (ABS) have rapidly drawn attention due to mature additive manufacturing. Plastic material is generally used and developed in commercial facilities and short lifespan applications according to several advantages such as high strength and modulus. Moreover, PLA production represents the cost-efficient and non-petroleum plastic due to the fact that it naturally degrades when exposed to the natural environment and its recycle utilization.<sup>14,15</sup> PLA plastic material structure and several mechanical properties have been studied to highlight its potential application. For example, Rodríguez-Panes et al.<sup>16</sup> carried out the effects of layer height, infill density and layer orientation on the mechanical performance of PLA and ABS test specimens. The results obtained by ABS specimens showed a lower variability than PLA specimens. Fernández-Vicente et al.<sup>17</sup> evaluated the influence of two controllable variables such as infill pattern and density factors, which aimed to save time and material consumption. The results determined that different infill patterns cause a variation of less than 5% in maximum tensile strength. In addition, PLA plastic material was provided as a safer alternative to the possible ABS plastic and gained greater attention attributed to its low cost equipment, variability and easy operation.<sup>18</sup> From the structural design perspective, mechanical properties of PLA structure could be affected by several factors such as layer thickness, orientation,<sup>19,20</sup> raster angle, processing temperature,<sup>21</sup> infill density and pattern structure,<sup>17</sup> and feed rate.<sup>19</sup> Furthermore, PLA with lower infill density was more efficient in energy dissipation, which is considered the mass of the specimens. To the best of our knowledge, there was no previous study on the effects of infill pattern structures of PLA tubular specimens on energy-absorbing characteristics. This study elucidated a novel approach to determine the effect of infill pattern structures on structural properties of single PLA and hybrid CFRP/PLA tubes, which advanced the potential application used in lightweight structure and automotive engineering.

Composite, as a relatively commercial material of engineering materials, has rapidly applied automotive transportation according to its respectively higher mechanical properties. Driven by its advantages, composite material is gradually used to replace the conventional metal material in automobile engineering<sup>22,23</sup> and space shuttle.<sup>24</sup> The crushing behavior and energy-absorbing characteristics of thin-walled metallic structures have been studied under different loading conditions such as axial crushing,<sup>25,26</sup> oblique compression,<sup>27,28</sup> and transverse crushing<sup>29,30</sup> using numerical and experimental methods, which were mainly affected by its design geometry,<sup>31,32</sup> material type,<sup>30</sup> and loading condition.<sup>5,33</sup> Unlike the traditional thin-walled metallic structure, the crushing mechanism of composites is far complex, which includes fiber breakage, fiber buckling, matrix cracking, matrix crushing, fiber matrix debonding, and delamination,<sup>5,34–36</sup> which were discovered and studied to contribute on crashworthiness. From the structural perspective, energy-absorbing characteristics of composite tubes are affected by many essential factors such as material type,<sup>30</sup> geometry structure,<sup>31,37</sup> trigger mechanism,<sup>22</sup> loading condition,<sup>33</sup> and winding angle.<sup>38</sup>

Noticeably, thin-walled metallic structures can regularly absorb impacting energy through a series of progressive folding and plastic deformation behavior. Compared with steel or aluminum tubes, composite tubes have a different energy-absorbing mechanism, which exhibits excellent capacity per mass.<sup>39</sup> Composite tubes are generally fabricated using filament winding technique due to its high production rate, product quality and repeatability compared to other composite fabrication processes. Carbon fiber is commonly used as reinforcement material, which offered a higher strength compared to glass fiber. Therefore, carbon fiber-reinforced plastic (CFRP) materials can provide higher energy-absorbing characteristics than glass fiber-reinforced plastic (GFRP) materials.<sup>5</sup>

In order to obtain excellent *EA* capability and lightweight structure feature together, it is rather difficult for CFRP material to fully replace metallic components in the automotive industry. For this aim, research interests have concentrated on hybrid composite structure products, which generally combined the metal feature with the higher mechanical properties and lightweight potentials, respectively. Recently, metals such as steel and aluminum are investigated to achieve the corresponding aim. In this perspective, Sun et al.<sup>40</sup> investigated the effects of winding angles and thickness on crashworthiness characteristics of CFRP and aluminum/CFRP hybrid tube under quasi-static crushing tests. It was found that both winding angle and wall thickness had essential influence on failure modes and crushing behaviors of CFRP and hybrid tubes.

Babbage and Mallick<sup>41</sup> conducted the experimental studies on energy-absorbing characteristics hybrid aluminum/composite tubes, and showed that crushing behaviors are largely affected by material parameters. It revealed that hybrid tubes showed a better *EA* capability than single tubes, which can be further improved by filling foam material. Eyvazian et al.<sup>42</sup> explored that corrugated metal composite tubes showed high *EA* characteristics according to uniformity of load versus displacement curves, reduction of initial peak load and failure mechanism behavior. Reuter and Tröster<sup>43</sup> investigated the crashworthiness of hybrid aluminum/CFRP tubes through experimental and numerical methods. It showed that hybrid tubes provided significant lightweight potentials, and the failure mode of the hybrid structure showed a mixture of *EA* mechanisms of its pure tubes.

With further exploration of hybrid structure, composite and concrete materials were studied to provide a better *EA* capability with lightweight features. For example, Xu et al.<sup>44</sup> explored the energy-absorbing characteristics of hybrid aramid/CFRP tubes. The bending mode showed the highest *EA*, whereas the buckling mode was the lowest and splaying mode was in between both modes. Karimi et al.<sup>45</sup> proposed a novel FRP-encased steel-concrete composite column, and discussed the advanced compressive behavior under axial loading. Feng et al.<sup>46</sup> studied a novel concrete-filled square steel tube (CFST) with an FRP-confined concrete core, which consisted of fiber-reinforced polymer (FRP), concrete and steel materials. It showed that the influence of the key design on mechanical characteristics were initial compressive stiffness, peak strain, ductility, and residual load-bearing capacity. Fam and Rizkalla<sup>47</sup> examined the behavior of concrete-filled glass fiber-reinforced polymer (GFRP) tubes under axial compression loading test, and it showed that strength and ductility of concrete were improved. The above-mentioned findings demonstrated the energy-absorbing characteristics and potential advantages of hybrid metal/composite with thin-walled structures. However, these studies lack hybrid structure combining with plastic material to become plastic/composite tube, especially for hybrid CFRP/PLA tubes, which are typically fabricated using additive manufacturing and filament winding techniques. Therefore, it is essential and necessary to study the infill pattern structures of hybrid CFRP/PLA tubes and observe its energy-absorbing characteristics of hybrid composite/plastic structures, which can have much potential to compete or even replace other hybrid components or structures according to excellent *EA* capacity, lightweight and environmental-friendly material features.

In this research study, PLA plastic material was used as the inner structure to replace steel or aluminum material. Carbon fiber was chosen as reinforcement

and epoxy resin as matrix to fabricate hybrid CFRP/PLA tube using the filament winding technique. Quasi-static axial crushing tests studied the effect of different infill pattern structures of single PLA and hybrid tubes on energy-absorbing characteristics. Moreover, a comparative research study on energy absorption (*EA*), specific energy absorption (*SEA*), compressive modulus and strength,  $F_{mean}$ ,  $F_{peak}$ , yield strength and crushing force efficiency (*CFE*) of the pure PLA tube, pure CFRP tube and hybrid CFRP/PLA tube were investigated to further observe the hybrid tubes with different infill pattern structures. Therefore, there is potential for improvement of single PLA and single CFRP tubes by using hybrid structure concept.

## Experimental methods

### Specimen preparation

In this study, 11 types of tubular tubes were prepared, which included one type of single-filament wound CFRP tubes, five types of different infill patterns single PLA tubes, and five types of hybrid CFRP/PLA tubes with different infill pattern structures. Three specimens from each type of tubular tubes were tested in this study, which offer a relatively steady and repeatability of experimental results. The specimen preparation procedure is shown in Figure 1(a). The height of all the specimens is 55 mm. The geometric dimensions of specimens are highlighted in Figure 1(b). Specimen thickness, mass, and stacking sequence are summarized in Table 1, which briefly provided one sample of single PLA and hybrid CFRP/PLA tubes with five infill patterns. The specimen is named according to infill pattern structures and type of material. For example, the specimen PLA-TRI represented a single PLA tube with triangle infill pattern structure. The specimen CP-TRI represented a hybrid CFRP/PLA tube, which consists of an inner PLA tube and an outer CFRP tube with two ply layers and  $\pm 45^\circ$  winding angle.

Filament wound CFRP tubes are made of Pyrofil TR30S 3K carbon fiber (provided by Pyrofil Department, Mitsubishi Rayon Co., Ltd) and D.E. R.<sup>TM</sup>331<sup>TM</sup> epoxy resin (supplied by Salju Bistari Sdn. Bhd) using the laboratory scale three-axis filament winding machine (manufactured by Structural Material & Degradation Focus Group, Universiti Malaysia Pahang).<sup>48</sup> For filament wound CFRP tubes, specimens were cured at 25°C for 24 h on the mandrel at 50 r/min rotation speed for 2 h, and the fiber mass fraction was around 46.77%. PLA tubes are made of PLA with 1.75 mm diameter and 1.25 g/cm<sup>3</sup> density, which is fabricated by the Prusa i3 MK3 machine. Five different infill pattern structures are listed as follows: normal, triangle, square, hexagonal, and tetrahedral infill

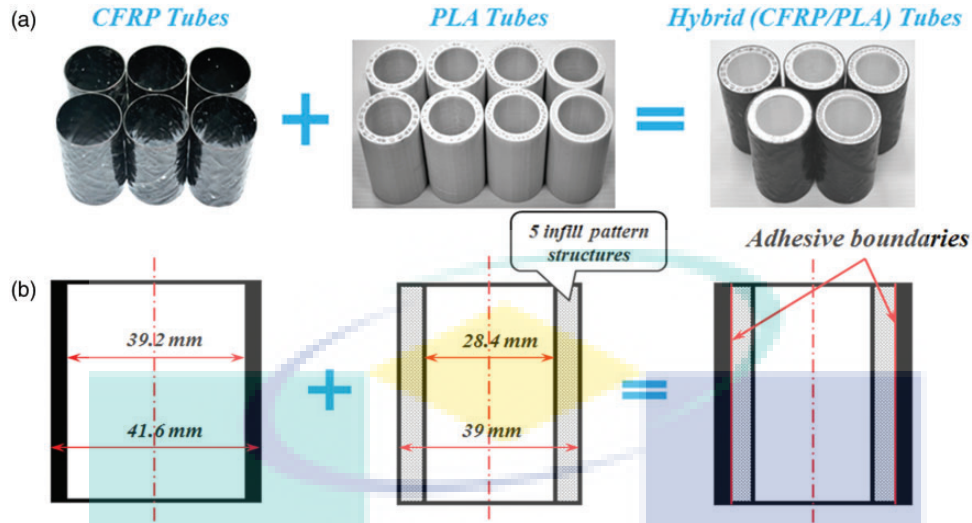


**Figure 1.** Specimen preparation: (a) individual specimen; (b) specimen schematic structure.

**Table 1.** Summary of several specimens in this study.

Specimens	Height (mm)	Wall thickness (mm)	Mass (g)	Stacking sequence
CFRP1	55	1.2	6.0	$(\pm 45^\circ)_2$
CFRP2	55	1.2	6.1	$(\pm 45^\circ)_2$
CFRP3	55	1.2	6.1	$(\pm 45^\circ)_2$
PLA-NOR	55	5.3	20.0	PLA layers
PLA-TRI	55	5.3	26.5	PLA layers
PLA-HEX	55	5.3	23.6	PLA layers
PLA-SQU	55	5.3	20.0	PLA layers
PLA-TET	55	5.3	25.9	PLA layers
CP-NOR	55	6.6	27.0	$(\pm 45^\circ)_2$ /PLA layers
CP-TRI	55	6.6	32.3	$(\pm 45^\circ)_2$ /PLA layers
CP-HEX	55	6.6	32.0	$(\pm 45^\circ)_2$ /PLA layers
CP-SQU	55	6.6	29.0	$(\pm 45^\circ)_2$ /PLA layers
CP-TET	55	6.6	33.3	$(\pm 45^\circ)_2$ /PLA layers

NOR: normal pattern; TRI: triangle pattern; HEX: hexagonal pattern; SQU: square pattern; TET: tetrahedral pattern; PLA: polylactic acid or polyactide; CFRP: carbon fiber-reinforced plastic; CP: hybrid CFRP/PLA tube.

pattern structures as shown in Figure 2. In order to specifically study the effects of infill pattern structures in the energy-absorbing characteristic of single and hybrid tubular structures, the infill density is equally set at 30% using the Slic3r software of Prusa i3 MK3 3D printing machine.

### Quasi-static axial compression tests

All the axial quasi-static compression tests were conducted in a standard universal testing machine INSTRON-3369 with the maximum loading capability of 50 kN. The loading speed of the upper crosshead was set constant at 4 mm/min throughout the tests. The

single CFRP tubes, single PLA tubes, and hybrid CFRP/PLA tubes were compacted at a 40 mm crushing displacement, which reaches 72% crushing length of original length. Three samples from each type of tubular conditions were investigated in this test, which offered a repeatable experimental data. The compressive strength and modulus,  $EA$  and yield strength were tested and recorded during the quasi-static crushing test. The load versus displacement curves were obtained by Bluehill software and the crushing behavior of specimens were photographed during the quasi-static compression test. Load plates were set parallel to each other before compressive tests.

### Crashworthiness characteristics criteria

All the test specimens underwent the quasi-static axial compression test, which determined compressive properties. Based on the previous studies on the crushing behavior of tubular structure in literature,<sup>38,40,49–52</sup> several typical compressive parameters were adopted to quantify the crashworthiness characteristics, such as  $EA$ ,  $SEA$ , mean crushing force ( $F_{mean}$ ), peak crushing force ( $F_{peak}$ ), crushing force efficiency ( $CFE$ ), and yield strength. Moreover, compressive properties of specimens were studied on compressive strength and modulus. The related crashworthiness criteria are shown as follows.

The average compressive strength of tubular structure was calculated using the following equation

$$\sigma_{avg} = \frac{4F}{\pi(D_o^2 - D_i^2)} \quad (1)$$

where  $F$  is crushing load,  $D_o$  and  $D_i$  are the outer and inner diameters of tubular structure, respectively.



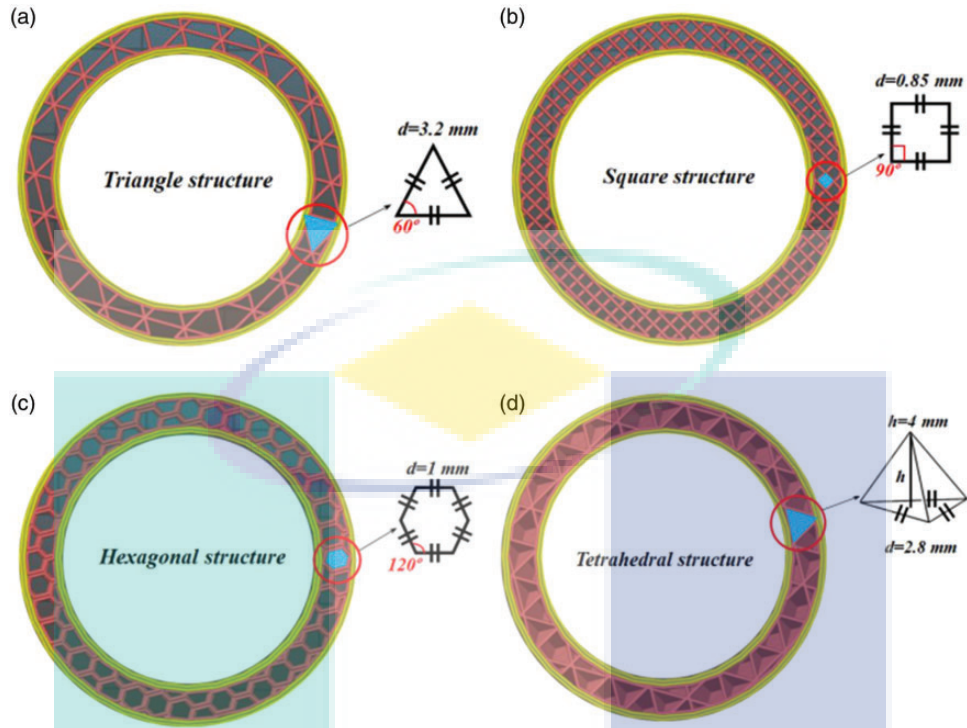


**Figure 2.** Four infill pattern structures by additive manufacturing: (a) triangle pattern; (b) square pattern; (c) hexagonal pattern; (d) tetrahedral pattern.

Compressive modulus of the tubular structure was obtained as follows

$$E = \frac{F}{A\varepsilon} \quad (2)$$

where  $F$  is crushing load along the longitudinal axis,  $A$  is the transverse cross-section area of specimen, and  $\varepsilon$  is the maximum strain along the longitudinal axis of the tubular structure.

The  $EA$  is defined and calculated mathematically as follows

$$EA = \int_0^d F(x)dx(J) \quad (3)$$

where  $F(x)$  is the instantaneous crushing load and  $d$  is crushing distance.

The  $SEA$  is total energy absorbed per unit mass, as

$$SEA = \frac{EA}{m} (J/g) \quad (4)$$

where  $m$  is the mass of each specimen. Obviously, a higher  $SEA$  value means the higher  $EA$  efficiency of specimen.

The peak crushing force ( $F_{peak}$ ) is directly obtained from the load versus displacement curve. The mean

crushing force ( $F_{mean}$ ) is calculated as

$$F_{mean} = \frac{EA}{d} (N) \quad (5)$$

The  $CFE$  is used to measure the uniformity of crushing force, as

$$CFE = \frac{F_{mean}}{F_{peak}} \quad (6)$$

A higher  $CFE$  value indicates the lower  $F_{peak}$  in comparison with  $F_{mean}$ , and lower acceleration ratio.

In addition, the yield point is the point on the stress-strain curve, which demonstrates the limit of elastic deformation and the beginning of plastic deformation. Yield strength is obtained and studied in the compression tests, which determines the limit of performance in single CFRP, single PLA and hybrid CFRP/PLA material type. The offset yield strength is the stress value at which 0.2 % plastic deformation starts, as discussed below.

## Results and discussion

### Crushing failure mode

Based on the previous studies<sup>9,36,38,40</sup> and related experimental results obtained from this study, four crushing failure modes were mainly identified of the

single PLA, single CFRP, and hybrid CFRP/PLA tubes, defined as the Mode I: progressive folding mode, Mode II: unstable local buckling mode, Mode III: progressive local buckling mode, and Mode IV: mid-length collapse, respectively, as illustrated in Figure 3.

Mode I is characterized in a form of stable local buckling of tubular wall, in which a number of small uniform symmetric folds appear in the tube wall, which resulted in relative stable plastic deformations. Mode II is distinguished in unstable local buckling of tubular wall, in which radial cracks propagated perpendicularly to the loading direction. This mode caused unstable crushing behavior and undesirable energy-absorbing characteristics. Mode III is characterized in a form of unstable progressive local non-buckling of the tubular wall, which resulted in unstable deformation. Mode IV is featured in a form of catastrophic collapse at the middle of the tube, which ultimately splits the tube into two separated parts following the fiber orientation transversely and causing lower *EA* capability.

### Results of single CFRP tubes

The crushing snapshot of CFRP tubes in the test is shown in Figure 4, which includes experimental setup

and the crushing behavior. In the elastic stage, the crushing force increased quickly to the peak crushing force of 5.03 kN at the displacement of 1.43 mm, where the CFRP tube underwent elastic deformation. Meanwhile, the crushing force decreased rapidly, where the specimen begins its plastic deformation stage. The crushing history of CFRP tubes is demonstrated in Figure 5, which highlights the crushing deformation history. Figure 6 shows the photographs of the damaged CFRP tubes, which is used to analyze the specimen failure mode.

Figure 6 shows the photographs of the three damaged CFRP tubes after compressive test, which aimed to analyze the crushing failure mode. As shown in Figure 6, for specimen CFRP1, several small regular folds were developed during the stable buckling in the tube wall and few cracks were observed. The *EA* is mainly based on fiber buckling, matrix plastic deformation, and friction of tube wall and two crossheads. For specimen CFRP2 and CFRP3, unstable buckling deformation is observed in the tube wall, which initiated and propagated some transverse cracks around some undamaged zones. The *EA* was mainly due to fiber buckling, transverse shearing, and friction between the tube wall and the crosshead. Moreover,

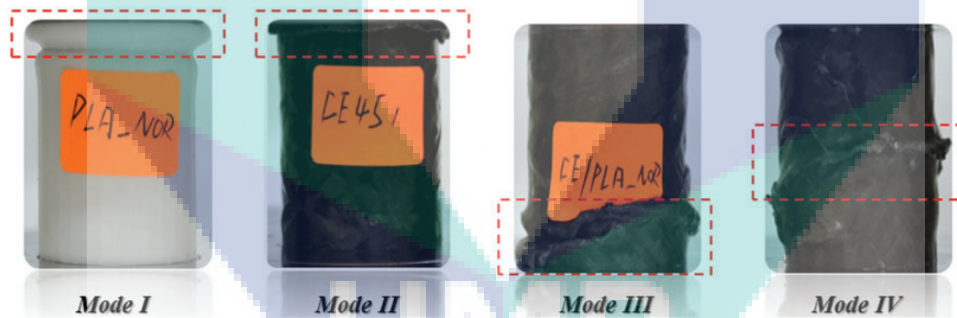


Figure 3. Typical crushing failure modes of the single PLA, single CFRP, and hybrid CFRP/PLA tubes.

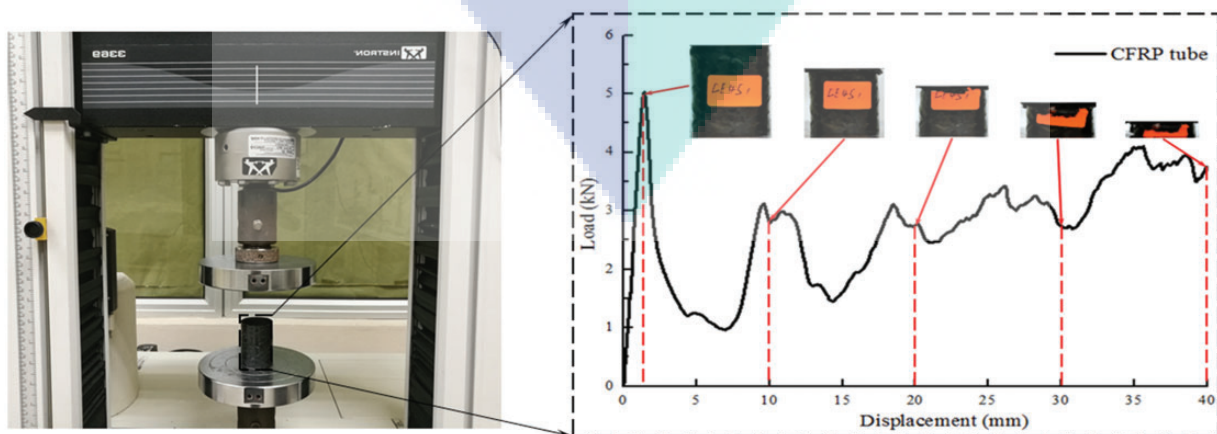
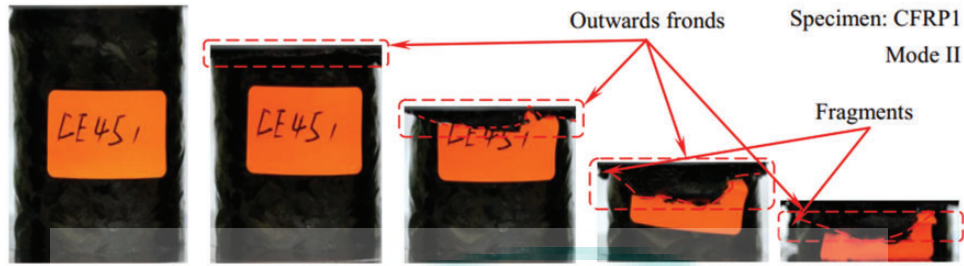
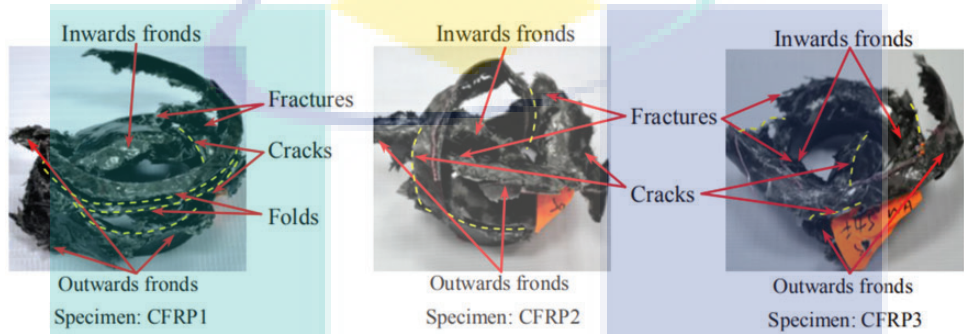


Figure 4. Experimental setup and the crushing behavior history of single CFRP tube in test.



**Figure 5.** The example history of crushing deformation behavior of single CFRP tube.



**Figure 6.** Typical single CFRP tubes after compression test.

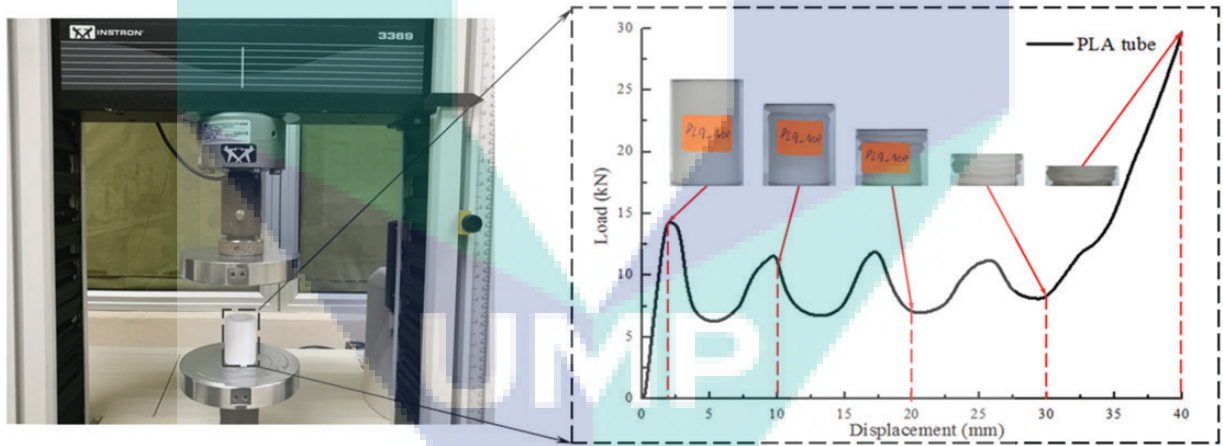


**Figure 7.** Experimental setup and the crushing behavior history of PLA tube in test.

some transverse cracks occurred and propagated as the crosshead moved further in the tests.

**Results of single PLA tubes**

The crushing history of PLA tube in compressive test is shown in Figure 7, which includes test setup and the crushing behavior history. In the elastic stage, the crushing force rise quickly to the peak crushing force of 14.29 kN at the displacement of 2.08 mm, where the PLA tube underwent the elastic deformation. The crushing force decreased rapidly, where the PLA tube

underwent the plastic deformation stage. The crushing behavior of PLA tubes was developed in the beginning with local buckling fold formed, which followed Mode I.

Figure 8 plotted the load–displacement curves of five infill pattern structures of PLA tubes under the quasi-static crushing tests. These curves show fairly similar trends and can be divided into two stages: namely elastic deformation stage and progressive deformation stage.<sup>40</sup> In the elastic deformation stage, the crushing load increased rapidly and soon reached the peak value. In addition, PLA tubes tend to collapse, and

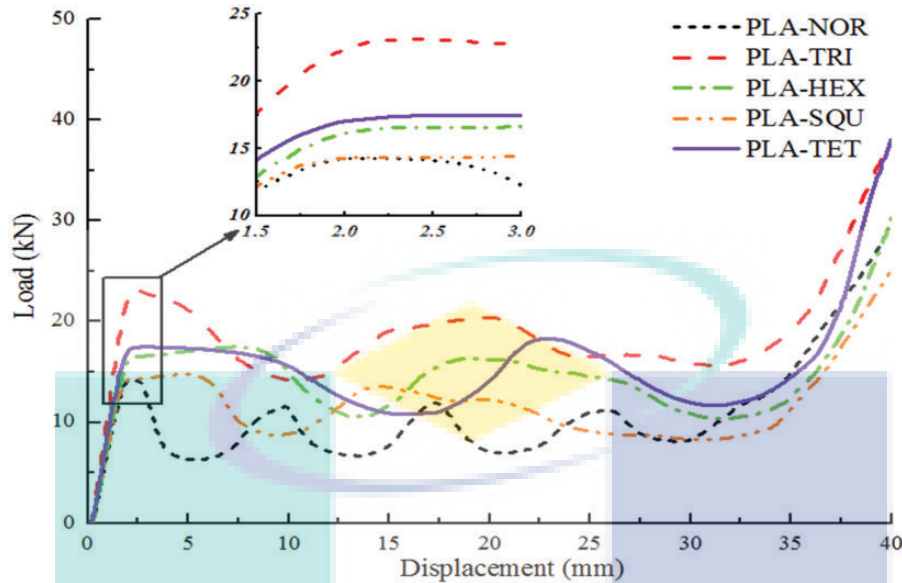


**Figure 8.** Typical load versus displacement curves of single PLA tubes with five infill pattern structures.

the crushing load drop abruptly to a lower level. Then, PLA tubes turned into the progressive deformation stage, where the crushing load fluctuated in a limited range around the mean force.

Those curves exhibited a rising trend of crushing load after 35 mm crushing displacement, which had researched 63 % damaged displacement of specimen length and provide much  $EA$  compared to elastic deformation stage. Note that the crushing behavior of PLA-NOR, PLA-TRI, PLA-HEX, PLA-SQU, and PLA-TET specimens were dominated by local buckling and formation of folds, which followed Mode I. From the above investigation, PLA-TRI specimen provides the highest peak crushing force of 23.13 kN, and the second is the PLA-TET specimen, which shows 17.50 kN peak crushing force. Interestingly, while PLA-NOR and PLA-SQU specimens have two different infill pattern structures and PLA-NOR specimen did not find voids on the top and bottom cross-section surface, their peak crushing forces were almost the same. This is probably explained by the infill pattern structure imperfection and infill structure printing method.

The crushing snapshots of PLA tubes with five infill pattern structures are shown in Figure 9. It can be seen that the failure of PLA-NOR, PLA-TRI, PLA-HEX, PLA-SQU, and PLA-TET specimens were in Mode I with local buckling deformation in the tube wall, and buckling paths initiated and propagated around the buckling zones as the crosshead moved further in the compressive test. As a result, buckling paths and regular folds occurred around the buckling zones, and some irregular buckling paths appeared as undamaged zones in the tube wall. For PLA-TRI and PLA-TET

specimens, triangle and tetrahedral infill pattern structures had the inclined tube wall compared to other infill structures, which resulted in several non-uniform folds from the inner and outer wall tube surfaces.

For PLA-NOR, PLA-HEX, and PLA-TET specimens, many small regular folds were developed during the stable local buckling in the tube wall and few cracks were observed. The  $EA$  was mainly due to plastic deformation, buckling cracks, and friction between the tube wall and crosshead. Interestingly, as for PLA-TRI and PLA-TET specimens, unstable buckling led to several undamaged zones between the buckling paths and several cracks around the tube wall, which resulted in the inclined tube wall around the slippage zones. The energy dissipation was due to initiation and propagation of non-uniform buckling, several cracks, plastic deformation, and frictional interaction between the tube wall and the two crossheads.

Figure 10 shows the photographs of the damaged PLA tubes with five infill pattern structures after compressive test according to 15 tested PLA tubes, which precisely evaluated crushing failure behavior according to damaged conditions. As shown in Figure 10(a), (b), and (c), for PLA-NOR, PLA-SQU, and PLA-TET specimens, many small regular folds were developed according to the stable local buckling in the inner and outer tube walls and regular buckling paths were observed. The  $EA$  was mainly due to buckling, plastic deformation, and friction between the tube wall and crosshead. For PLA-TRI and PLA-HEX specimens, unstable buckling led to several undamaged zones between the buckling paths and transverse cracks around the tube wall, which provided non-uniform

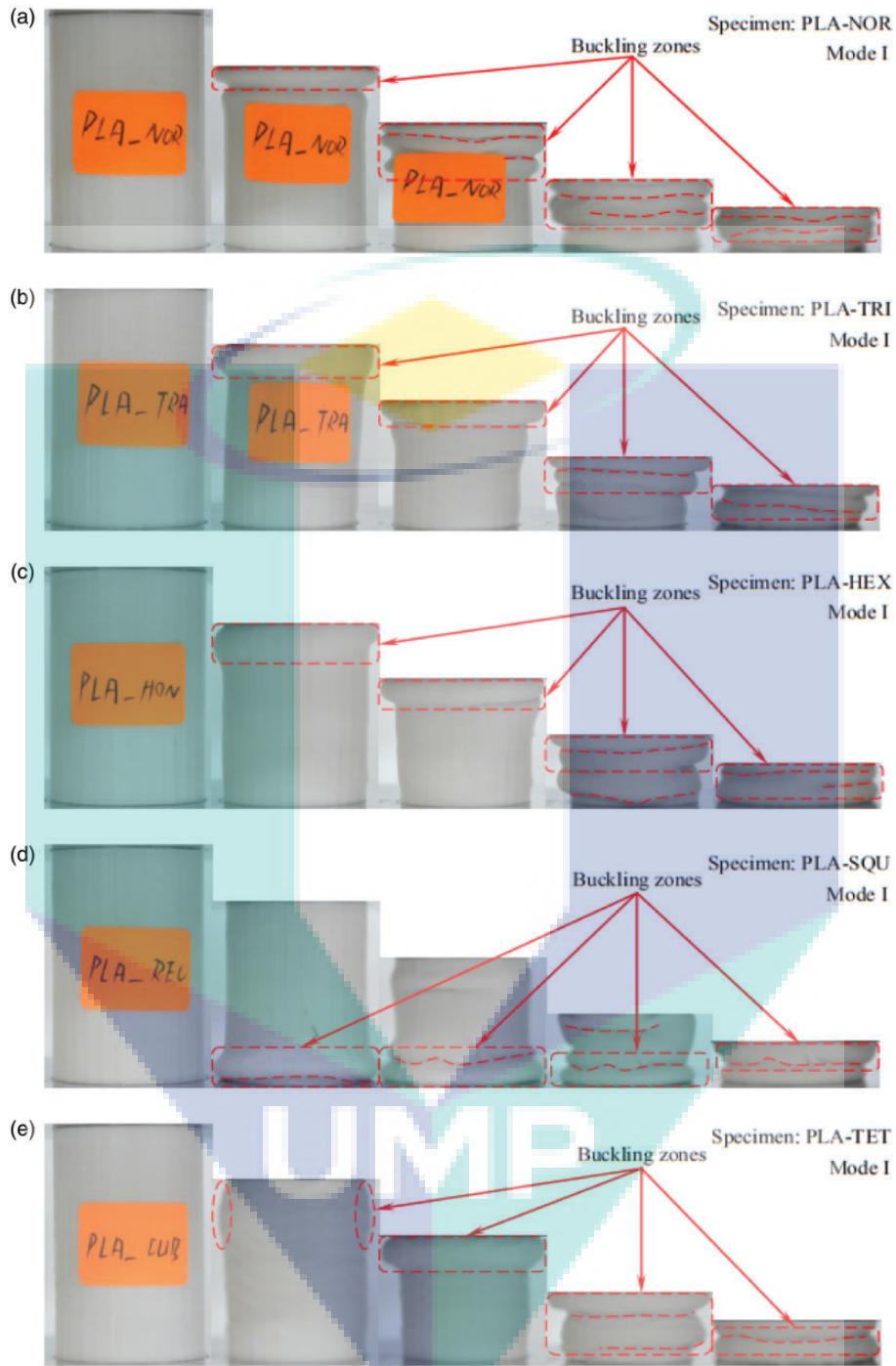


**Figure 9.** Typical crushing history of single PLA tubes with five infill pattern structures: (a) normal pattern; (b) triangle pattern; (c) hexagonal pattern; (d) square pattern; (e) tetrahedral pattern.

axisymmetric buckling folds with inclined walls in transverse zone. Few cracks were observed in the inner and outer tube walls, which were attributed to the initiation and propagation of transverse shearing. The *EA* was mainly due to buckling, transverse shearing, and friction between the tube wall and crosshead.

Deformed cross-section shape of single PLA tubes after compressive test was shown in Figure 11, which was used to measure and prove crushing failure deformation behavior. For PLA-NOR, PLA-HEX, and PLA-TET specimens, it was noted that the inner and outer folds developed a stable local buckling path,

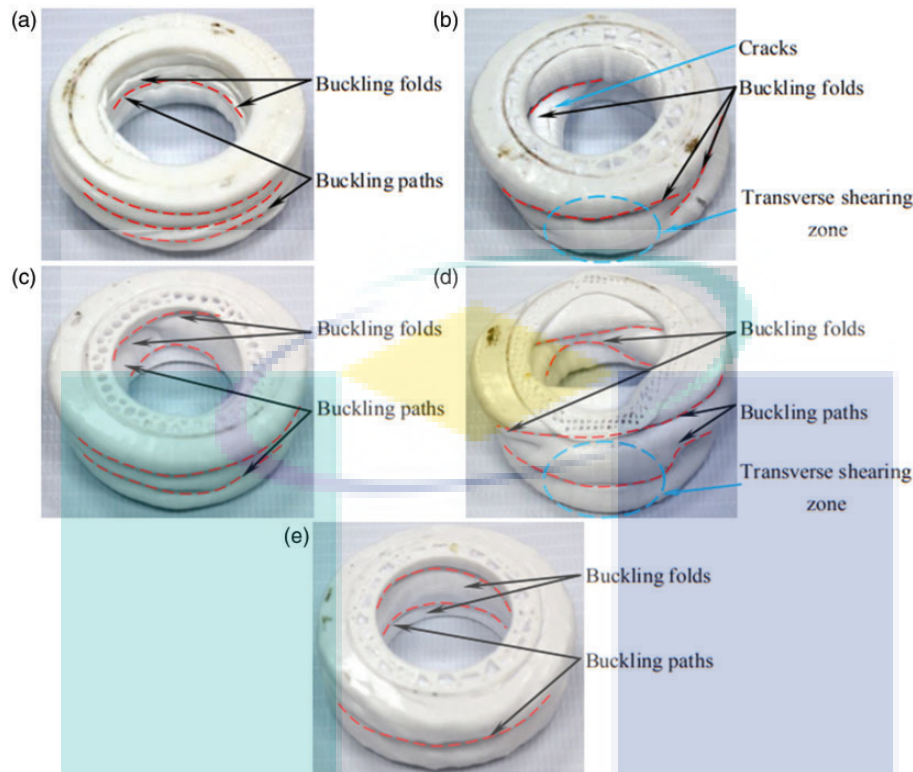


**Figure 10.** Typical single PLA tubes after compressive test: (a) normal pattern; (b) triangle pattern; (c) hexagonal pattern; (d) square pattern; (e) tetrahedral pattern.

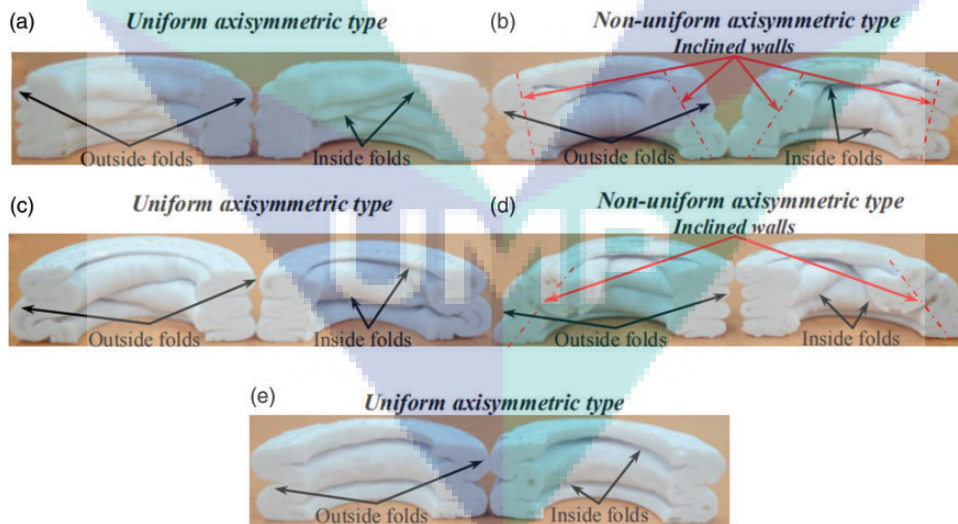


**Figure 11.** Typical deformed cross-section shape of single PLA tubes with five infill pattern structures after compression test: (a) normal pattern; (b) triangle pattern; (c) hexagonal pattern; (d) square pattern; (e) tetrahedral pattern.

respectively, and tube walls were parallel to axial direction, which led to favorable energy-absorbing characteristics like PLA-TRI and PLA-SQU specimens. The tubular walls were inclined to the axial direction based on transverse shearing, friction between the tube wall

and crosshead, which observed non-uniform axisymmetric buckling type.

To investigate the effects of five infill pattern structures on the energy-absorbing characteristics of single PLA tubes, the specimens were studied and discussed,

and the  $EA$ ,  $SEA$ , compressive strength and modulus,  $F_{peak}$ ,  $F_{mean}$ , yield strength, and  $CFE$  were plotted in Figure 12, which provided error bar on related parameters. As for the PLA-TRI specimen, values of  $EA$ ,  $SEA$ ,  $F_{peak}$ ,  $F_{mean}$ , compressive strength, and yield strength displayed the highest point compared to the other four infill pattern structures. The  $EA$  capability of the specimen was the best due to the unstable buckling in the tube wall, where several undamaged zones even remained as the effect of crushing behavior.

The effect of infill pattern structure on compressive strength and modulus was shown in Figure 12(b), which exhibited that the five infill pattern structures provided a similar trend according to two parameters. Interestingly, PLA-SQU specimen provided opposite trend points on  $F_{peak}$  and  $F_{mean}$ , which are indicated in Figure 12(c). With PLA-NOR, it was noted that normal infill pattern structure indicated the lowest values on  $EA$ ,  $SEA$ ,  $F_{peak}$ ,  $F_{mean}$ , yield strength, and  $CFE$ . The  $EA$  capability of the PLA-NOR specimen

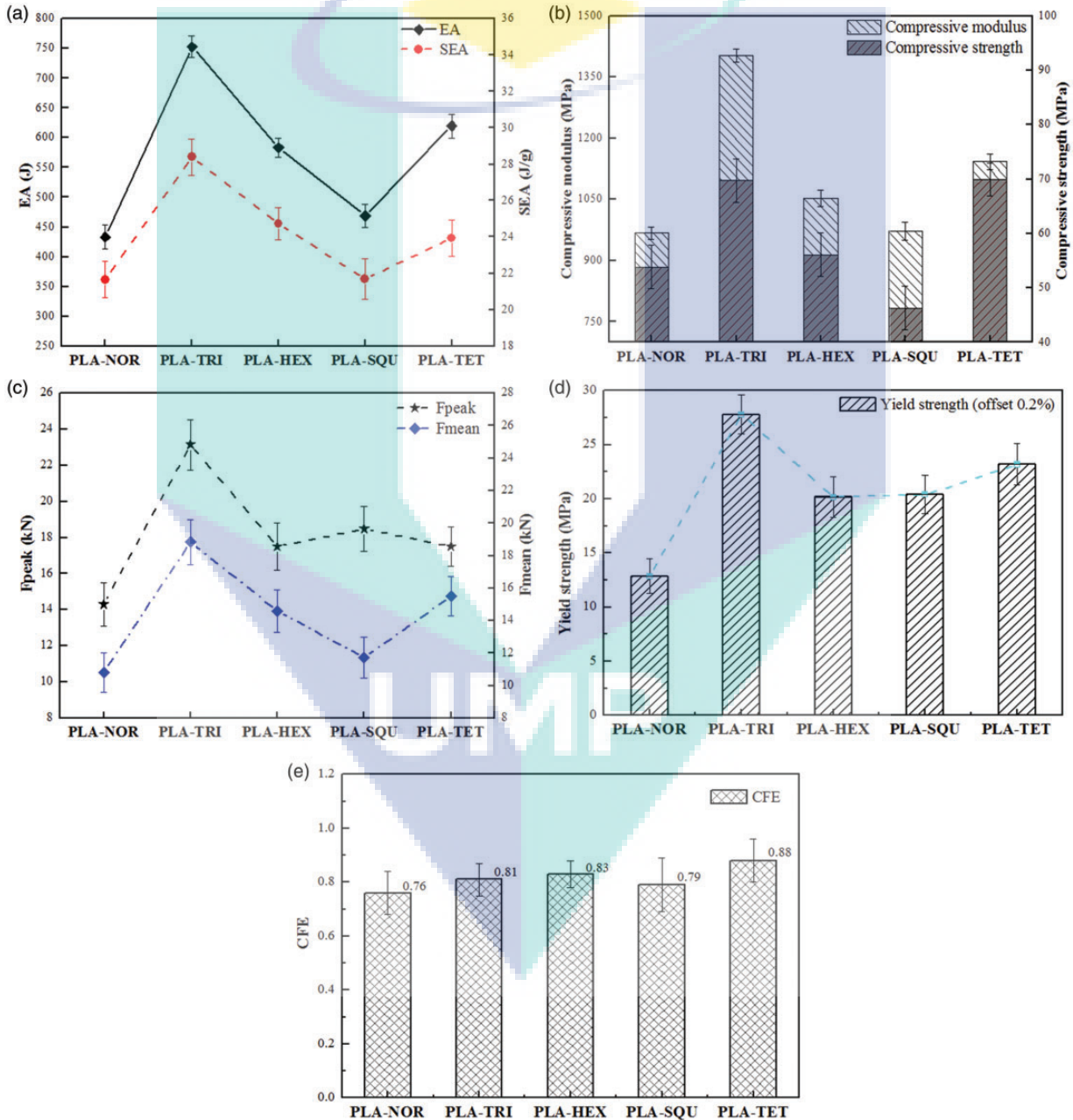


**Figure 12.** The effect of five infill pattern structures on energy-absorbing characteristics of single PLA tubes: (a) energy absorption and specific energy absorption; (b) compressive strength and modulus; (c)  $F_{peak}$  and  $F_{mean}$ ; (d) yield strength (offset 0.2%); (e) crushing force efficiency.

shows the lowest crashworthiness due to the stable local buckling deformation in the inner and outer tube walls.

From the above investigation, crushing performance of the single PLA tubes significantly affected significantly the infill pattern structures. For triangle infill pattern structures, the  $EA$ ,  $SEA$ , compressive modulus,  $F_{peak}$ ,  $F_{mean}$ , and yield strength tended towards the peak value, but the CFE did not exhibit such a peak trend value. On the contrary, normal infill pattern structures provided the lowest values on the  $EA$ ,  $SEA$ ,  $F_{peak}$ ,  $F_{mean}$ , yield strength, and CFE. However, it presents higher compressive parameters respectively.

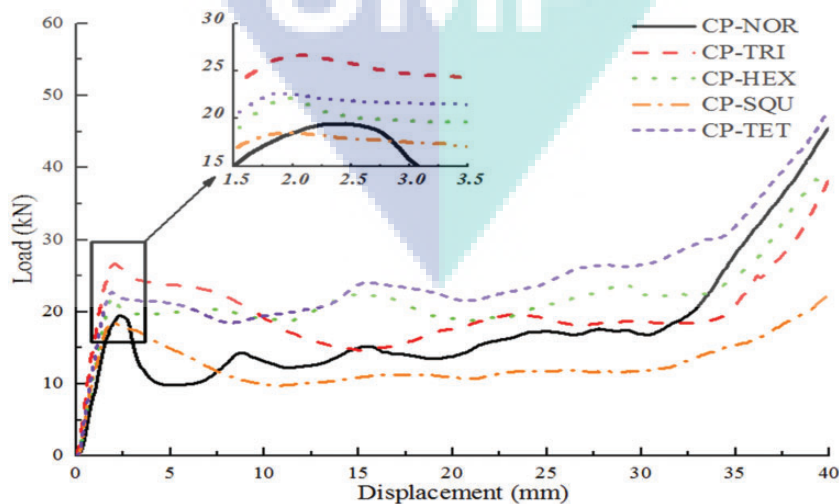
### Results of hybrid CFRP/PLA tubes

Figure 13 exhibited the load versus displacement curves of hybrid CFRP/PLA tubes with five infill patterns under the quasi-static crushing tests, which presented a similar crushing trend in its elastic deformation. Note that different fluctuation ranges and similar crushing trends were shown in the progressive deformation stage. Five curves presented similar crushing trends according to different infill pattern structure failure, which can be divided into three ranks. The first rank was occurred in CP-TRI specimen with triangle infill pattern structure, which showed the same rank in single PLA tube. The second rank was CP-HEX and CP-TET specimens with hexagonal and tetrahedral structures, which had the close peak force of 22.18 and 22.68 kN. The third rank consists of CP-NOR and CP-SQU specimens, which showed lower peak force respectively.

The crushing behavior of the hybrid CFRP/PLA tubes with five infill pattern structures is shown in

Figure 14, which obtains typical photograph from 15 tested hybrid CFRP/PLA tubes. Due to the interactive effect between the inner single PLA and outer CFRP tubes, the deformation modes from those individual PLA and individual CFRP tubes, and the all inner PLA tubes with five infill pattern structures in the hybrid structure are experienced in the single PLA tube deformation. Interestingly, regardless of the different infill pattern structures, all these CFRP/PLA tubes wrapped outside with the CFRP tubes exhibited Mode III or Mode IV deformation induced by buckling deformation of the inner PLA tube. Evidently, the constraints from the PLA tube largely affected the deformation modes of the outer CFRP tubes, which appeared to be more significant than the effect of infill pattern structures in this study. Furthermore, the deformation of the CFRP tubes in the hybrid structure was much more stable compared to the single counterparts.

The CP-NOR tube exhibited the failure of Mode III, in which stable buckling folds and crack paths tended to propagate along the axial direction. It was observed that the lamina bundles can only buckle due to the restriction from the inner PLA tube. The failure of CP-TRI tube was in Mode IV, which collapsed at the middle of specimen. There is no evidence that the progressive plastic deformation in the inner PLA tube strengthened the outer CFRP tube, which avoided a middle-length collapse. The failure of CP-HEX tube was in combination of Mode II, Mode IV in the outer CFRP tube and regular buckling fold in the inner PLA tube. It was observed that Mode II dominated the deformation of outer CFRP tube in the initial crushing stage, and then Mode III played a dominant role in the end of the test. The failure of CP-SQU tube



**Figure 13.** Typical load versus displacement curves of hybrid CFRP/PLA tubes with five infill pattern structures.



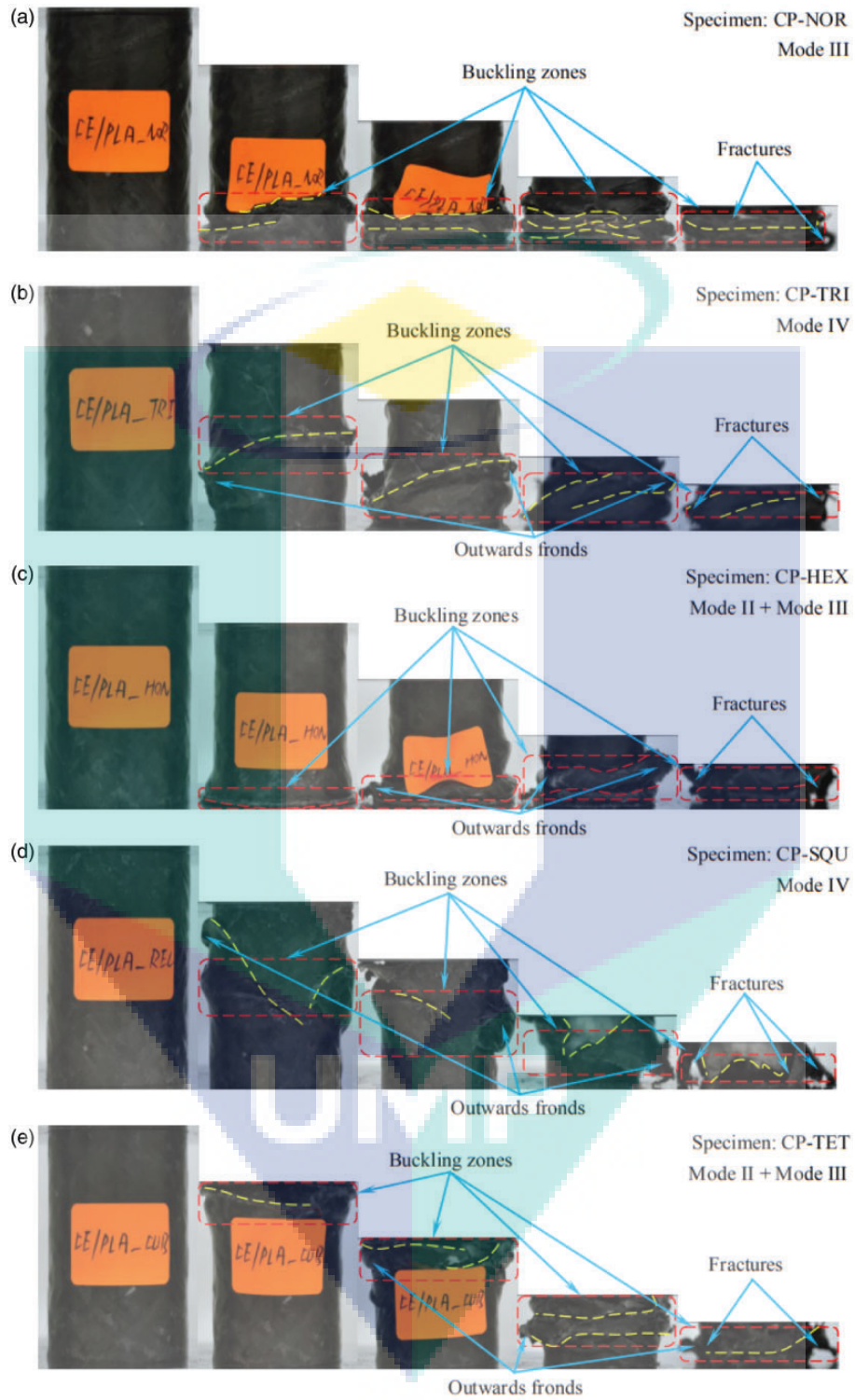


**Figure 14.** Typical crushing history of hybrid CFRP/PLA tubes with five infill pattern structures: (a) normal pattern; (b) triangle pattern; (c) hexagonal pattern; (d) square pattern; (e) tetrahedral pattern.

was similar to that of CP-TRI tube, with a series of outward fronds, fractures developed as a form of catastrophic collapse at the middle of the tube, which split the tube into two separated parts following the fiber

orientation transversely and provided lower *EA* capability.

The failure of the CP-TET tube was similar to that of CP-HEX; several buckling folds, outwards and

fracture observed in the outer CFRP tube as a result of plastic deformation in the inner PLA tube. It was noted that the folds of CP-TET and CP-TRI tubes were not as regular as CP-NOR tube. Figure 16 plots the load versus displacement curves of the CFRP/PLA tubes under the quasi-static crushing tests, and several energy-absorbing characteristics of the single CFRP tube, single PLA tube and hybrid CFRP/PLA tube calculated from these curves are briefly summarized in Table 2.

The damaged hybrid tubes with five infill patterns were typically shown in Figure 15, which exhibited the typical deformation behavior from 15 tested hybrid tubes. Interestingly, all the inner PLA tubes exhibited plastic deformation and finally developed into buckling fold patterns. As shown in Figure 15(a), (c), and (e), stable local buckling led to a series of regular small folds around the buckling paths and in the outer CFRP tube wall. In this condition, the *EA* mechanism was mainly attributed to fiber buckling, fracture of the outer CFRP tubes, plastic deformation of inner PLA tubes, as well as frictional contact between the tube wall and the crosshead. As shown in Figure 15(b) and (d), unstable local buckling led to a series of small non-uniform axisymmetric buckling and folds with inclined walls. In this case, the *EA* was mainly due to fiber buckling, transverse shearing, fracture of the CFRP tubes, plastic deformation of inner PLA tubes and frictional contact between the tube wall and the crosshead.

Deformed cross-section shape hybrid CFRP/PLA tubes after compressive tests are summarized and compared in Figure 16, which were typically selected from three repeatable tested results. For CP-NOR, CP-HEX, and CP-TET specimens, it was clearly noticed that the inner and outer folds of PLA tubes developed a stable local buckling path respectively, and tube

structure were almost parallel to the axial direction. The buckling type followed uniform axisymmetric type, and some outer folds overlapped with the CFRP tubes such as CP-NOR specimen. Several outer CFRP tubes were totally separated with the outer PLA tube, which might be caused by the adhesion type. For CP-TRI and CP-SQU specimens, tube walls were inclined to the axial direction based on infill pattern structure effect, transverse shearing, friction between the tube wall and crosshead, which was observed to be the non-uniform axisymmetric buckling type. It was shown that the outer CFRP tubes were poorly folded with triangle and hexagonal pattern structures of the inner PLA tube, which provided same deformed cross-section shape of single PLA tube after a compressive test in Figure 11. Compared to uniform axisymmetric buckling types, the non-uniform axisymmetric buckling types caused more cracks, fiber fracture, and failure damage of CFRP tubes. This type could easily cause unstable crushing and lead to unfavorable energy-absorbing characteristics.

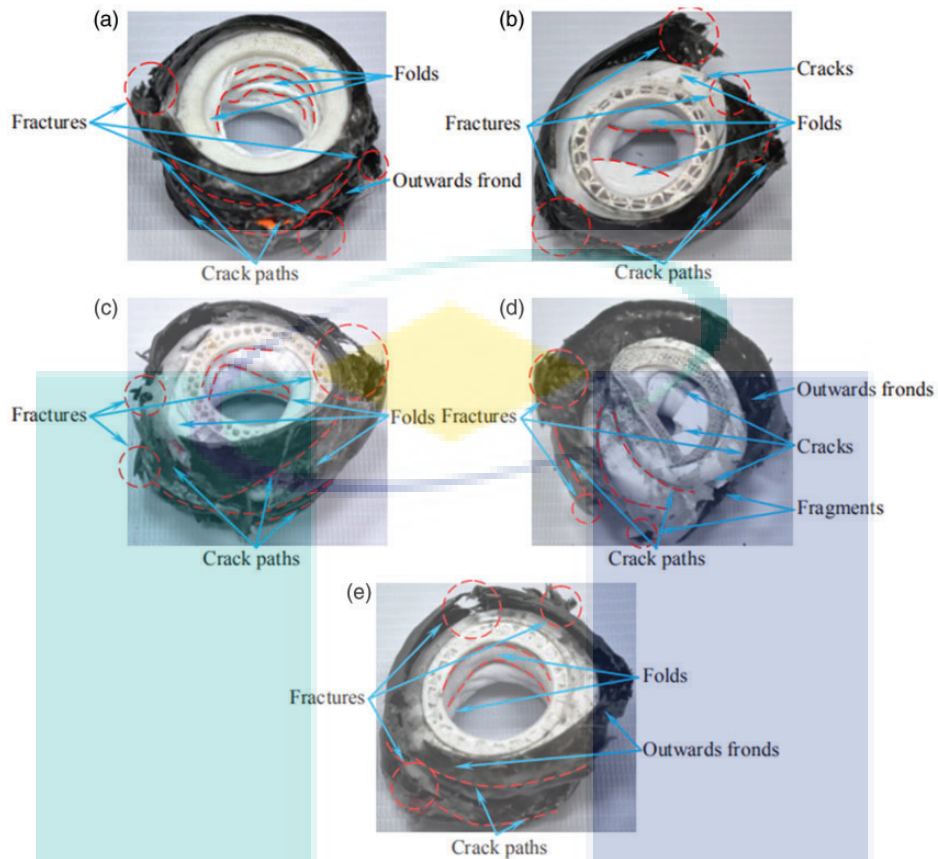
To investigate the effects of infill structure patterns on the quasi-static compression test on energy-absorbing characteristics of the hybrid tubes, the *EA*, *SEA*, compressive modulus and strength,  $F_{peak}$ ,  $F_{mean}$ , yield strength and *CFE* are studied with specific error bars on related parameters. Figure 17(a) showed the effects of infill pattern on the *EA* and *SEA* of hybrid tubes. The *EA* value was maximum at tetrahedral structure on CP-TET specimen with 987.59 J, which agreed with the specific *EA* trend. Moreover, the minimum value of specific *EA* shown in the square structure was 17.77 J/g, which was consistent with varying trends of *EA*.

Figure 17(b) plotted the effects of infill pattern on compressive modulus and strength of hybrid

**Table 2.** Summary of compressive characteristics of several specimens in this study.

Specimens	Failure mode	<i>EA</i> (kJ)	<i>SEA</i> (J/g)	Compressive strength (MPa)	Compressive modulus (MPa)	Yield strength (MPa)
CFRP1	Mode II	0.10	17.96	46.90	2737.37	26.41
CFRP2	Mode IV	0.11	18.39	48.43	2940.41	28.57
CFRP3	Mode III	0.10	17.11	43.61	2563.32	23.63
PLA-NOR	Mode I	0.43	21.65	53.82	967.86	12.84
PLA-TRI	Mode I	0.75	28.40	69.72	1401.88	27.80
PLA-HEX	Mode I	0.58	24.72	56.05	1052.95	20.16
PLA-SQU	Mode I	0.47	21.69	46.28	971.58	20.40
PLA-TET	Mode I	0.62	23.94	69.97	1142.60	23.19
CP-NOR	Mode III	0.71	26.34	67.97	981.68	18.32
CP-TRI	Mode IV	0.81	24.94	57.71	1643.40	24.39
CP-HEX	Mode II + III	0.88	27.43	58.59	1242.13	29.21
CP-SQU	Mode IV	0.52	17.77	33.42	1369.01	14.69
CP-TET	Mode II + III	0.99	29.66	70.63	1428.70	29.91

NOR: normal pattern; TRI: triangle pattern; HEX: hexagonal pattern; SQU: square pattern; TET: tetrahedral pattern; PLA: polylactic acid or polyactide; CFRP: carbon fiber-reinforced plastic; CP: hybrid CFRP/PLA tube.



**Figure 15.** Typical hybrid CFRP/PLA tubes after compression test: (a) normal pattern; (b) triangle pattern; (c) hexagonal pattern; (d) square pattern; (e) tetrahedral pattern.

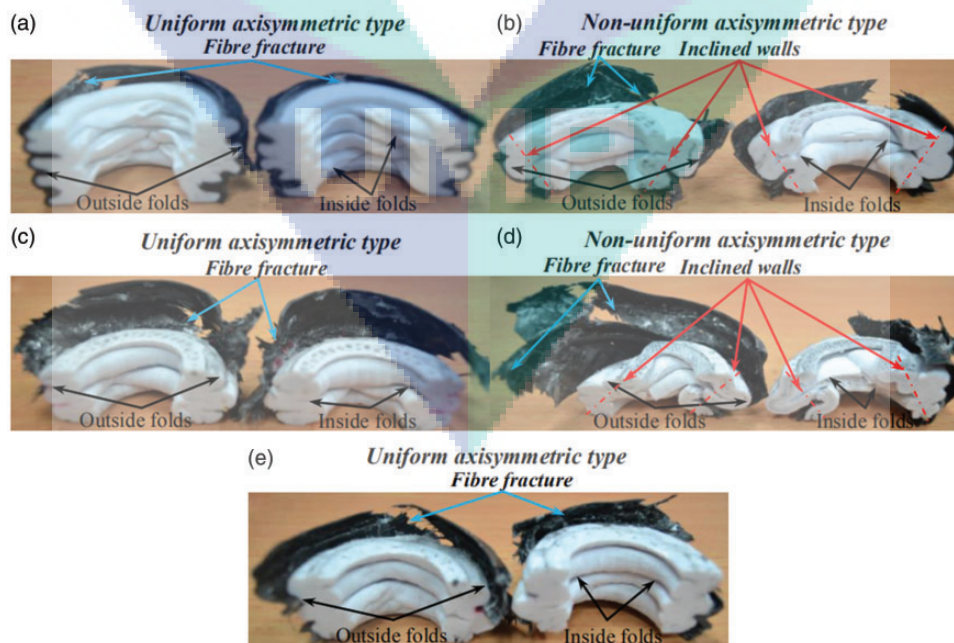


**Figure 16.** Typical deformed cross-section shape of hybrid CFRP/PLA tubes with five infill pattern structures after compression test: (a) normal pattern; (b) triangle pattern; (c) hexagonal pattern; (d) square pattern; (e) tetrahedral pattern.

CFRP/PLA tubes. The compressive modulus value was maximum at triangle pattern with 1643.40 MPa, and the minimum value happened at normal structure with 981.68 MPa. However, the compressive strength value was maximum at tetrahedral pattern with 70.63 MPa, and the minimum compressive strength value was 33.42 MPa. The effect of infill pattern on  $F_{peak}$  and  $F_{mean}$  of hybrid tubes are shown in Figure 17(d), which plotted the infill pattern structure trend. For square infill patterns, the minimum values of  $F_{peak}$

and  $F_{mean}$  were occurred. The maximum  $F_{peak}$  was 26.65 kN, which was shown in a triangular pattern. The  $F_{mean}$  trend showed a similar trend as yield strength, which shows the maximum value with tetrahedral pattern and the minimum value with square pattern. The crushing force efficiency was studied, which is shown in Figure 17(e). Based on the results, tetrahedral pattern of the hybrid tube with value of 1.09 CFE provided the lowest  $F_{peak}$  in comparison with  $F_{mean}$  and presented the lowest acceleration damages by the

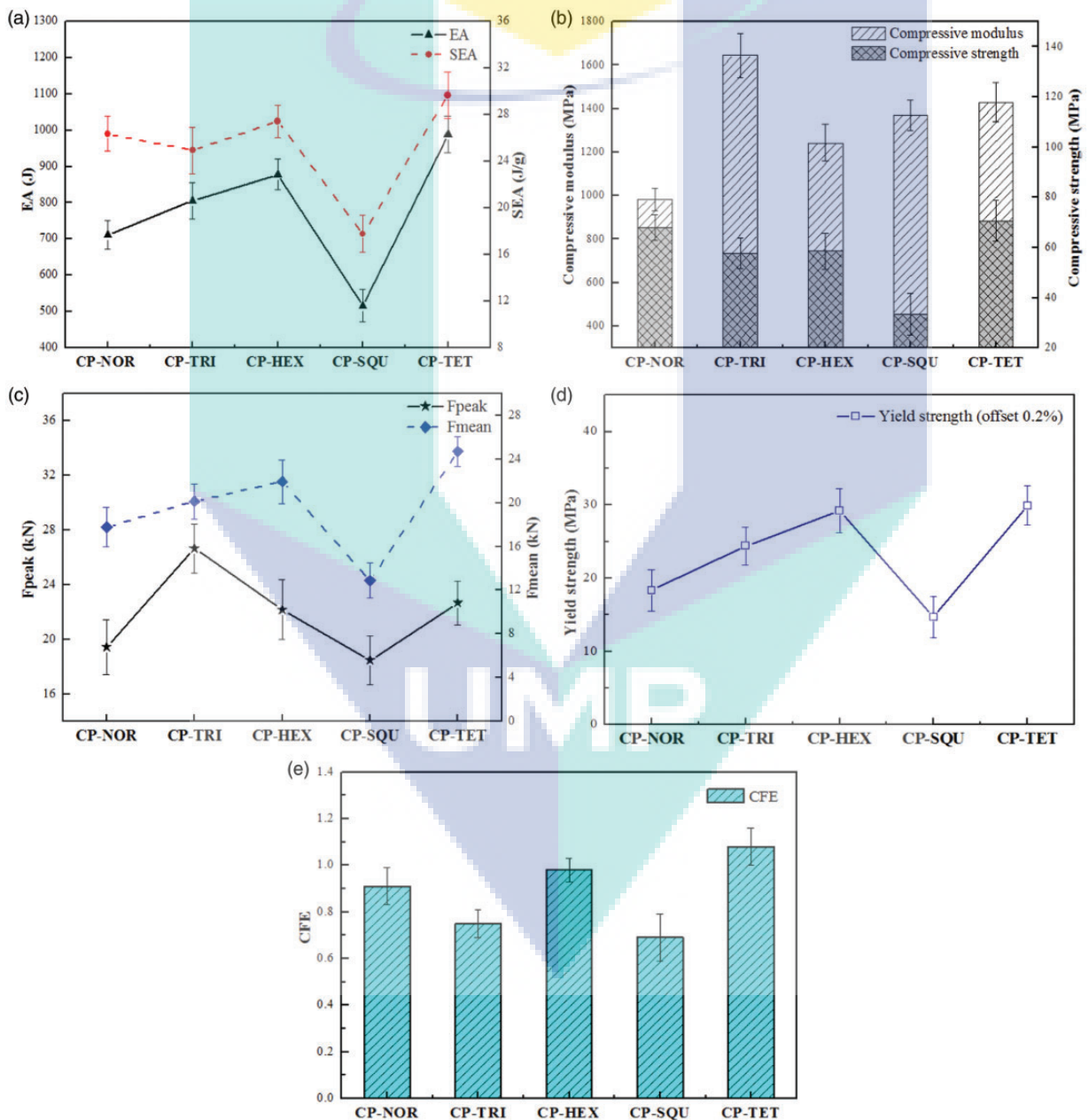


**Figure 17.** The effect of five infill pattern structures on energy-absorbing characteristics of hybrid CFRP/PLA tubes: (a) energy absorption and specific energy absorption; (b) compressive strength and modulus; (c)  $F_{peak}$  and  $F_{mean}$ ; (d) yield strength (offset 0.2%); (e) crushing force efficiency.

occupants. On the contrary, square patterns with value of 0.69  $CFE$  implied the highest  $F_{peak}$  in comparison with  $F_{mean}$ , and highest acceleration performed on quasi-static test.

**Comparison results between single PLA and hybrid CFRP/PLA tubes**

The load versus displacement curves of single PLA and hybrid CFRP/PLA tubes with five infill pattern structures were plotted in Figure 18. Based on the comparison results, hybrid tubes provided better

energy-absorbing characteristics compared to single PLA tubes. Moreover, crushing characteristics of single or hybrid tubes can be significantly affected by the infill pattern structures. It concluded that hybrid tubes provided a higher  $F_{peak}$  value than single PLA tubes with the same infill pattern structures, which improved around 1.15 to 1.36 times. Based on the overall crushing deformation behavior on single and hybrid tubes of load versus displacement curves, it can mainly be divided into two types, which are the continuous separated growth types and floating intersect growth types.

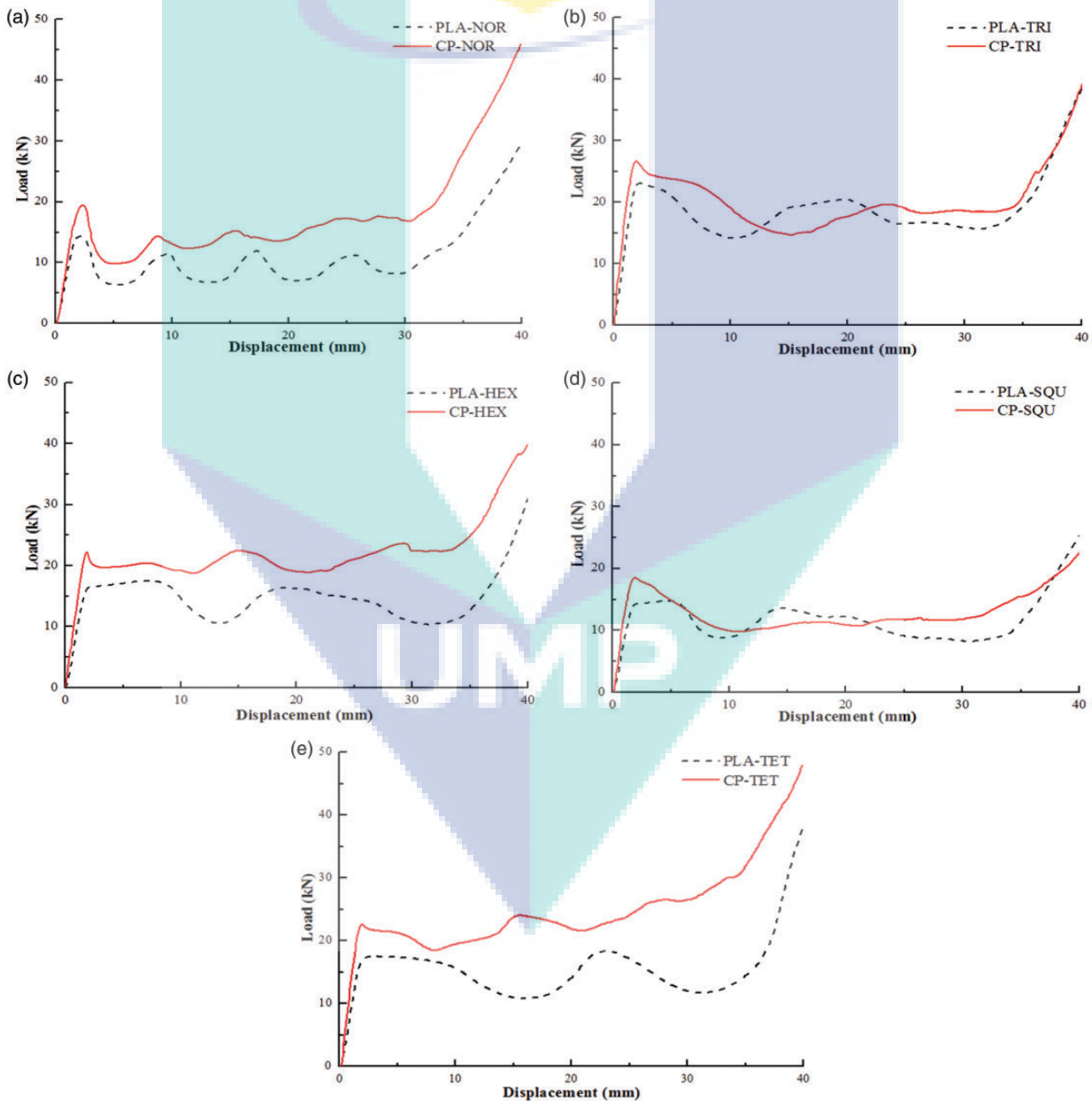


**Figure 18.** Typical load versus displacement curves comparison results between single PLA and hybrid CFRP/PLA tubes with five infill pattern structures: (a) normal pattern; (b) triangle pattern; (c) hexagonal pattern; (d) square pattern; (e) tetrahedral pattern.

Figure 18(a), (c), and (e) showed the continuous separated growth types, which exhibited that the rising tendency and the load–displacement curve of hybrid tube exceeded the load–displacement curve of single tube. Figure 18(b) and (d) presented the floating intersect growth types, which had a floating intersect between single and hybrid tubes of the load–displacement curves. In addition, it showed a lower net increasing EA value between single and hybrid tubes compared to continuous separated growth types, respectively. In order to more comprehensively compare and evaluate the crushing performance according to load versus displacement curves the infill pattern, material type, and four points of crushing displacements are summarized and analyzed in Table 3. The rising and decreasing trends were marked and highlighted, which evaluated the crushing performance according to displacement intervals with 10 mm rising values. It obtained more specific comparison results of

crushing performance behavior with five infill patterns and material types in four displacement points.

For the design of energy-absorbing application parts for automotive engineering, the effect of different infill patterns and hybrid structures could also be considered while pursuing better EA characteristics. Therefore, the behavior performance of hybrid structures is further analyzed together with single CFRP and PLA tubes on crashworthiness characteristics. To more intuitively compare the energy-absorbing characteristics of single PLA and hybrid CFRP/PLA tubes with different infill pattern structures, the radar map is shown in Figure 19. For comparison, it was evident that the hybrid structure performance is better compared to single PLA tubes. Radar maps of single PLA and hybrid CFRP/PLA tubes showed similar trends according to five infill pattern structures, which are provided in Figure 17. The hybrid CFRP/PLA tube with tetrahedral pattern had advantages in terms of a better EA, SEA, CFE,

**Table 3.** Load versus displacement curves of comparison analysis results for single PLA and hybrid CFRP/PLA tubes on five infill pattern structures.

Specimens	Infill pattern	Material type	Load values at four displacement points (kN)			
			10 mm	20 mm	30 mm	40 mm
1	Normal	PLA	11.17	7.09	8.37	38.33
2		CFRP/PLA	13.06 ↗	13.90 ↗	16.88 ↗	46.32 ↗
3	Triangle	PLA	14.16	20.38	15.75	38.58
4		CFRP/PLA	18.96 ↗	17.70 ↘	18.61 ↗	39.22 ↗
5	Square	PLA	8.88	12.23	8.32	25.13
6		CFRP/PLA	9.93 ↗	10.87 ↘	11.83 ↗	22.56 ↘
7	Hexagonal	PLA	14.81	16.25	10.82	30.65
8		CFRP/PLA	19.15 ↗	19.00 ↗	22.35 ↗	39.87 ↗
9	Tetrahedral	PLA	15.60	14.12	11.19	38.12
10		CFRP/PLA	19.48 ↗	21.83 ↗	26.46 ↗	48.01 ↗

↗: rising; ↘: declining; PLA: polylactic acid or polyactide; CFRP: carbon fiber-reinforced plastic.

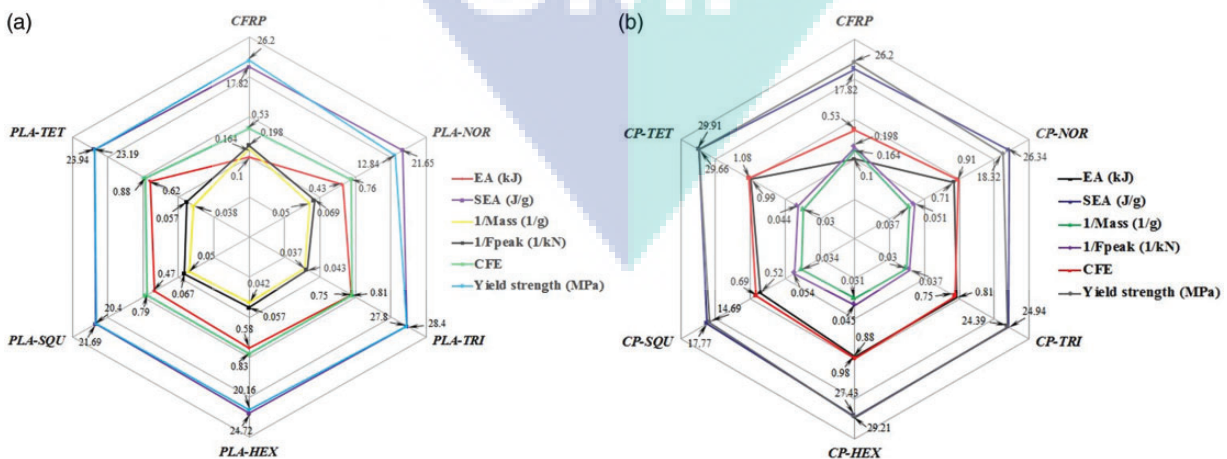


**Figure 19.** Radar maps of energy-absorbing characteristics with five infill pattern structures: (a) PLA tube; (b) hybrid CFRP/PLA tube.

and yield strength. Interestingly, for single CFRP tubes, a lower  $EA$  value compared to other single PLA and hybrid CFRP tubes was found, which indicated that the thin-walled structure of CFRP tubes showed lower  $EA$  on the crashworthiness.

Meanwhile, single PLA and hybrid tubes with hexagonal and square patterns only showed an advantage in mass reduction ( $1/Mass$ ). The results revealed that single PLA tubes with triangle and tetrahedral pattern structures provided better crashworthiness performance as pure structure perspective. Moreover, hybrid CFRP/PLA tubes with hexagonal and tetrahedral pattern structures had better energy-absorbing characteristics in terms of quasi-static compressive properties. Overall, from the engineering application perspective, it is clear that the hybrid CFRP/PLA tube with tetrahedral infill pattern structure had greater potential to be used in energy absorber after taking into consideration on performance, mass and costs.

From the above experimental results, it was found that some CFRP tube or PLA tube in the hybrid tube provided better crushing behavior than single CFRP or single PLA tubes. In order to further study the  $EA$  mechanization of hybrid CFRP/PLA tubes, the extra  $EA$  of interaction effect is defined and compared with  $EA$  of hybrid structure with the sum of  $EA$  of two individual tubes.<sup>40</sup> It was defined and calculated as follows

$$EA_{Interaction} = EA_{hybrid} - (EA_{CFRP} + EA_{PLA}) \quad (7)$$

where  $EA_{hybrid}$  is the energy absorption of the hybrid tube structure,  $EA_{CFRP}$  is the energy absorption of single CFRP tube, and  $EA_{PLA}$  is the energy absorption

of single PLA tube. Therefore,  $EA_{Interaction}$  is defined as the extra energy absorption by a hybrid structure.

In addition, the interaction effect ratio  $\varphi_e$  is defined as follows

$$\varphi_e = \frac{EA_{Interaction}}{(EA_{CFRP} + EA_{PLA})} \times 100\% \quad (8)$$

The value of zero refers to no interaction effect, for example, the value of 1.0 means the hybrid tube absorbs twice as much compared to the two individual specimens, which belongs to the positive interaction effect. Evidently, negative interaction effects were observed in this test, which is not found and discussed in previous study results.<sup>40</sup>

According to the load–displacement curves of the single PLA and single CFRP tubes,  $EA_{Interaction}$ ,  $EA_{CFRP}$ , and  $EA_{PLA}$  were calculated on five infill pattern structures. Figure 20 showed interaction effects between the single tube and hybrid tube, which studied  $EA$  interaction and interaction effect ratio. Figure 20 shows that the hybrid tube of normal, hexagonal, and tetrahedral patterns, which obtained the positive interaction effect. The  $EA$  capabilities of hybrid specimens exceed the sum of individual specimens. The energy-absorbing characteristics of hybrid tubes might explain the interactive effect, which is caused by the bond (epoxy adhesive) between the inner PLA tube and outer CFRP tube.

On the contrary, hybrid tube of triangle and square patterns showed a negative interaction effect, which was verified according to results of Figure 18, indicating that hybrid tubes had lower  $EA$  capability than the

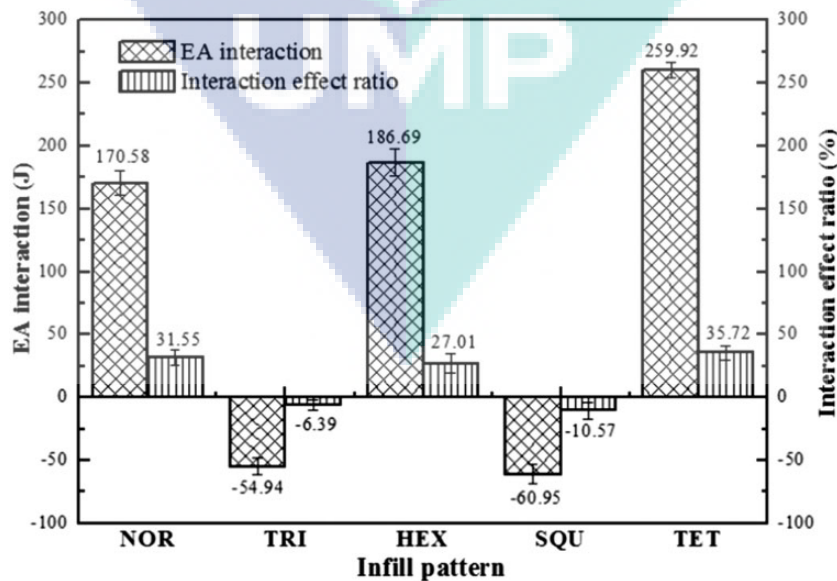


Figure 20. Interaction effect between the single tube and hybrid tubes on five infill pattern structures.

sum of the single CFRP tube and single PLA tube separately. The  $EA$  interaction value was maximum at tetrahedral pattern with 259.92 J, while it obtained the maximum interaction effect ratio ( $\varphi_e$ ) with 35.72 %. Furthermore, the  $EA$  interaction and interaction effect ratio had a similar trend according to the infill pattern structures.

On the one hand, the individual CFRP, such as CFRP1, is more prone to unstable buckling collapses. When the single CFRP tube was bonded to the outer PLA tube, the deformation behavior of the CFRP tube in the hybrid tube showed a much more stable performance compared to the single CFRP tube, as depicted in Figures 14 to 16. For instance, the  $EA$  of specimen CFRP1 improved 9.17 times in comparison with  $EA$  of the hybrid tube in tetrahedral pattern. As for single PLA tubes, the  $EA$  of the PLA-NOR and PLA-TRI specimen increased 1.65 times and 1.07 times compared to the corresponding infill pattern of hybrid tube, respectively.

## Conclusion

The energy-absorbing characteristics of single CFRP, single PLA tubes, and hybrid CFRP/PLA tubes were studied in this experimental test. The crushing deformation behavior, failure modes, load versus displacement curves, and effects of different infill pattern structures of PLA tubes on crashworthiness were investigated through quasi-static axial crushing test. In addition, the interaction effects between the two tubular specimens were identified. Within the limitation of this study, the following conclusion can be summarized:

1. For single CFRP tubes, all load versus displacements exhibited the elastic stage and progressive deformation stage. Furthermore, it was concluded that small thickness easily led to unstable deformation, which was studied based on CFRP specimen deformation behavior. The crushing behavior of CFRP tubes on quasi-static axial compression tests was studied, which includes  $EA$ ,  $SEA$ , compressive modulus and strength, yield strength,  $F_{peak}$ ,  $F_{mean}$ , and  $CFE$ .
2. For inner single PLA tubes, infill pattern structures considerably affected the energy-absorbing characteristics. The five infill pattern structures studied are normal, triangular, square, hexagonal, and tetrahedral patterns. For triangle infill patterns of single PLA tubes, the  $EA$ ,  $SEA$ , compressive modulus,  $F_{peak}$ ,  $F_{mean}$ , and yield strength have reached the maximum values, but the  $CFE$  did not show such a peak trend value. On the contrary, normal infill pattern of single PLA tubes had the minimum values on the  $EA$ ,  $SEA$ ,  $F_{peak}$ ,  $F_{mean}$ , yield strength, and

$CFE$ . However, it exhibited higher compressive parameters compared to triangle infill patterns.

3. Compared with the single CFRP tubes, all the hybrid tubes show more stable crushing deformation behavior due to the inner PLA tube support and interactive effects. The load–displacement curves demonstrated noticeable elastic deformation stage and progressive deformation stage. The tetrahedral pattern of hybrid CFRP/PLA tube obtained maximum values of  $EA$ ,  $SEA$ ,  $F_{peak}$ , yield strength, and  $CFE$ , which were 987.59 J, 29.66 J/g, 22.68 kN, 29.91 MPa and 1.09 improved 59.3 %, 23.9 %, 29.6 %, 28.8 %, and 22.4 %, respectively, compared to single PLA tubes with tetrahedral pattern. The maximum compressive modulus is 1643.40 MPa with triangle pattern, which increased 17.2 % based on single triangle pattern PLA tubes. Moreover, interaction effect between the CFRP tubes and PLA tubes was examined. Based on the experimental results, it obtained positive and unexpected negative interaction effect. It was observed that the maximum values of  $EA_{Interaction}$  and interaction effect ratio  $\varphi_e$  were 259.92 J and 35.7% on tetrahedral pattern. Evidently, it was noted that the hybrid tube of triangle and square patterns showed negative interaction effect, which were  $-54.94$  J,  $-6.39$  % and  $-60.95$  J,  $-10.57$  %, respectively.

## Highlights

1. The infill pattern structure plays an important role on the energy-absorbing characteristics in the inner single PLA and hybrid CFRP/PLA tubes.
2. Filament wound hybrid CFRP/PLA tubes have potential for improvement of the energy-absorbing characteristics compared to inner single PLA and outer CFRP tubes.
3. The triangle and tetrahedral infill pattern structures of hybrid CFRP/PLA and single PLA tubes exhibited better energy-absorbing characteristics under quasi-static axial crushing condition.

## Acknowledgements

This research work is strongly supported by the Structural Material & Degradation Focus Group (SMD) and the Human Engineering Focus Group (HEG), which provided the research materials and equipment.

## Declaration of conflicting interests

The author(s) declared no potential conflicts of interest with respect to the research, authorship, and/or publication of this article.



## Funding

The author(s) disclosed receipt of the following financial support for the research, authorship, and/or publication of this article: The Ministry of Education Malaysia (Fundamental Research Grant Scheme: RDU190158) and Universiti Malaysia Pahang (Internal Research Grant: PGRS180319) funded this research.

## ORCID iD

Mohd R Mat Rejab  <https://orcid.org/0000-0002-4030-6085>

## References

- Alia RA, Al-Ali O, Kumar S, et al. The energy-absorbing characteristics of carbon fiber-reinforced epoxy honeycomb structures. *Journal of Composite Materials* 2019; 53: 1145–1157.
- Sun G, Liu T, Huang X, et al. Topological configuration analysis and design for foam filled multi-cell tubes. *Eng Struct* 2018; 155: 235–250.
- Lau ST and Said Ma Yaakob MY. On the effect of geometrical designs and failure modes in composite axial crushing: a literature review. *Compos Struct* 2012; 94: 803–812.
- Yahaya R, Sapuan S, Jawaid M, et al. Effect of fibre orientations on the mechanical properties of kenaf-aramid hybrid composites for spall-liner application. *Defence Technol* 2016; 12: 52–58.
- Zhu G, Sun G, Liu Q, et al. On crushing characteristics of different configurations of metal-composites hybrid tubes. *Compos Struct* 2017; 175: 58–69.
- Shin KC, Lee JJ, Kim KH, et al. Axial crush and bending collapse of an aluminum/GFRP hybrid square tube and its energy absorption capability. *Compos Struct* 2002; 57: 279–287.
- Alia R, Guan Z, Jones N, et al. The energy-absorption characteristics of metal tube-reinforced polymer foams. *J Sandwich Struct Mater* 2015; 17: 74–94.
- Heimbs S, Strobl F, Middendorf P, et al. Composite crash absorber for aircraft fuselage applications. *WIT Trans Built Environ* 2010; 113: 3–14.
- Bisagni C, Di Pietro G, Frascini L, et al. Progressive crushing of fiber-reinforced composite structural components of a formula one racing car. *Compos Struct* 2005; 68: 491–503.
- Hou T, Pearce G, Prusty B, et al. Pressurised composite tubes as variable load energy absorbers. *Compos Struct* 2015; 120: 346–357.
- Kim HC, Shin DK, Lee JJ, et al. Crashworthiness of aluminum/CFRP square hollow section beam under axial impact loading for crash box application. *Compos Struct* 2014; 112: 1–10.
- Zarei H and Kröger M. Crashworthiness optimization of empty and filled aluminum crash boxes. *Int J Crashworthiness* 2007; 12: 255–264.
- Zarei H, Kröger M and Albertsen H. An experimental and numerical crashworthiness investigation of thermoplastic composite crash boxes. *Compos Struct* 2008; 85: 245–257.
- Nampoothiri KM, Nair NR and John RP. An overview of the recent developments in polylactide (PLA) research. *Bioresour Technol* 2010; 101: 8493–8501.
- Thompson RC, Moore CJ, Vom Saal FS, et al. Plastics, the environment and human health: current consensus and future trends. *Phil Trans R Soc B* 2009; 364: 2153–2166.
- Rodríguez-Panes A, Claver J and Camacho A. The influence of manufacturing parameters on the mechanical behaviour of PLA and abs pieces manufactured by FDM: a comparative analysis. *Materials* 2018; 11: 1333.
- Fernandez-Vicente M, Calle W, Ferrandiz S, et al. Effect of infill parameters on tensile mechanical behavior in desktop 3D printing. *3D Printing Additive Manuf* 2016; 3: 183–192.
- Groenendyk M and Gallant R. 3D printing and scanning at the Dalhousie University Libraries: a pilot project. *Library Hi Tech* 2013; 31: 34–41.
- Rankouhi B, Javadpour S, Delfanian F, et al. Failure analysis and mechanical characterization of 3D printed ABS with respect to layer thickness and orientation. *J Fail Anal Prev* 2016; 16: 467–481.
- Vaezi M and Chua CK. Effects of layer thickness and binder saturation level parameters on 3D printing process. *Int J Adv Manuf Technol* 2011; 53: 275–284.
- Brady D. The crystallinity of poly (phenylene sulfide) and its effect on polymer properties. *J Appl Polym Sci* 1976; 20: 2541–2551.
- Zhu G, Sun G, Li G, et al. Modeling for CFRP structures subjected to quasi-static crushing. *Compos Struct* 2018; 184: 41–55.
- Chiu LN, Falzon BG, Ruan D, et al. Crush responses of composite cylinder under quasi-static and dynamic loading. *Compos Struct* 2015; 131: 90–98.
- Sanjay M, Arpitha G and Yogesha B. Study on mechanical properties of natural-glass fibre reinforced polymer hybrid composites: a review. *Mater Today* 2015; 2: 2959–2967.
- Andrews K, England G and Ghani E. Classification of the axial collapse of cylindrical tubes under quasi-static loading. *Int J Mech Sci* 1983; 25: 687–696.
- Guillow S, Lu G and Grzebieta R. Quasi-static axial compression of thin-walled circular aluminium tubes. *Int J Mech Sci* 2001; 43: 2103–2123.
- Greve L, Pickett A and Payen F. Experimental testing and phenomenological modelling of the fragmentation process of braided carbon/epoxy composite tubes under axial and oblique impact. *Compos Part B* 2008; 39: 1221–1232.
- Tarlochan F, Samer F, Hamouda AMS, et al. Design of thin wall structures for energy absorption applications: enhancement of crashworthiness due to axial and oblique impact forces. *Thin-Walled Structures* 2013; 71: 7–17.
- Kim HC, Shin DK and Lee JJ. Characteristics of aluminum/CFRP short square hollow section beam under transverse quasi-static loading. *Compos Part B* 2013; 51: 345–358.

30. Priem C, Othman R, Rozycki P, et al. Experimental investigation of the crash energy absorption of 2.5 D-braided thermoplastic composite tubes. *Compos Struct* 2014; 116: 814–826.
31. Kalhor R and Case SW. The effect of FRP thickness on energy absorption of metal-FRP square tubes subjected to axial compressive loading. *Compos Struct* 2015; 130: 44–50.
32. Sun G, Li S, Li G, et al. On crashing behaviors of aluminium/CFRP tubes subjected to axial and oblique loading: an experimental study. *Compos Part B* 2018; 145: 47–56.
33. Baroutaji A, Sajjia M and Olabi A-G. On the crashworthiness performance of thin-walled energy absorbers: recent advances and future developments. *Thin-Walled Struct* 2017; 118: 137–163.
34. Boria S, Scattina A and Belingardi G. Axial energy absorption of CFRP truncated cones. *Compos Struct* 2015; 130: 18–28.
35. Kim J-S, Yoon H-J and Shin K-B. A study on crushing behaviors of composite circular tubes with different reinforcing fibers. *Int J Impact Eng* 2011; 38: 198–207.
36. Grauers L, Olsson R and Gutkin R. Energy absorption and damage mechanisms in progressive crushing of corrugated NCF laminates: fractographic analysis. *Compos Struct* 2014; 110: 110–117.
37. Mamalis AG, Manolakos D, Ioannidis M, et al. Crashworthy characteristics of axially statically compressed thin-walled square CFRP composite tubes: experimental. *Compos Struct* 2004; 63: 347–360.
38. Jia X, Chen G, Yu Y, et al. Effect of geometric factor, winding angle and pre-crack angle on quasi-static crushing behavior of filament wound CFRP cylinder. *Compos Part B* 2013; 45: 1336–1343.
39. Sun G, Li S, Liu Q, et al. Experimental study on crashworthiness of empty/aluminum foam/honeycomb-filled CFRP tubes. *Compos Struct* 2016; 152: 969–993.
40. Sun G, Wang Z, Hong J, et al. Experimental investigation of the quasi-static axial crushing behavior of filament-wound CFRP and aluminum/CFRP hybrid tubes. *Compos Struct* 2018; 194: 208–225.
41. Babbage J and Mallick P. Static axial crush performance of unfilled and foam-filled aluminum-composite hybrid tubes. *Compos Struct* 2005; 70: 177–184.
42. Eyvazian A, Mozafari H and Hamouda AM. Experimental study of corrugated metal-composite tubes under axial loading. 2017.
43. Reuter C and Tröster T. Crashworthiness and numerical simulation of hybrid aluminium-CFRP tubes under axial impact. *Thin-Walled Struct* 2017; 117: 1–9.
44. Xu J, Ma Y, Zhang Q, et al. Crashworthiness of carbon fiber hybrid composite tubes molded by filament winding. *Compos Struct* 2016; 139: 130–140.
45. Karimi K, Tait MJ and El-Dakhkhni WW. Testing and modeling of a novel FRP-encased steel-concrete composite column. *Compos Struct* 2011; 93: 1463–1473.
46. Feng P, Cheng S, Bai Y, et al. Mechanical behavior of concrete-filled square steel tube with FRP-confined concrete core subjected to axial compression. *Compos Struct* 2015; 123: 312–324.
47. Fam A and Rizkalla SH. Behavior of axially loaded concrete-filled circular FRP tubes. *ACI Struct J* 2001; 98: 280–289.
48. Quanjin M, Rejab M and Sahat I. Design of portable 3-axis filament winding machine with inexpensive control system. *J Mech Eng Sci* 2018; 12: 3479–3493.
49. Guler MA, Cerit ME, Bayram B, et al. The effect of geometrical parameters on the energy absorption characteristics of thin-walled structures under axial impact loading. *Int J Crashworthiness* 2010; 15: 377–390.
50. Sun G, Xu F, Li G, et al. Crashing analysis and multi-objective optimization for thin-walled structures with functionally graded thickness. *Int J Impact Eng* 2014; 64: 62–74.
51. Rezvani MJ and Jahan A. Effect of initiator, design, and material on crashworthiness performance of thin-walled cylindrical tubes: a primary multi-criteria analysis in lightweight design. *Thin-Walled Struct* 2015; 96: 169–182.
52. Aziz AR. *The energy-absorbing characteristics of novel tube-reinforced sandwich structures*. PhD Dissertation, University of Liverpool, UK, 2015.